ANALYSIS OF HIGH-κ DIELECTRIC THIN FILMS WITH TIME-OF-FLIGHT MEDIUM ENERGY BACKSCATTERING

By

Robert D. Geil

Dissertation

Submitted to the Faculty of the

Graduate School of Vanderbilt University

in partial fulfillment of the requirements

for the degree of

DOCTOR OF PHILOSOPHY

in

Chemical Engineering

August, 2005

Nashville, Tennessee

Approved:

Professor Bridget R. Rogers

Professor Robert A. Weller

Professor Kenneth A. Debelak

Professor G. Kane Jennings

Professor Peter T. Cummings

To Mom and Dad, for providing so much love and support throughout my lengthy career as a student

ACKNOWLEDGEMENTS

This dissertation would not have been possible with out the guidance of my advisors, Bridget Rogers and Robert Weller. I am immensely grateful for the patience and confidence they displayed. Special thanks to Zhe Song, group member and CVD (and digital photography) expert. Thanks to: Walt Augustyniak, who taught me an invaluable amount in the accelerator laboratory; other group members along the way: Vivek Pawar, Nirav Vora, Mekha George, and Dan Crunkleton; Jessica Hilton for depositing samples for my depth resolution study. I would also like to acknowledge the National Science Foundation for funding that helped support this work.

TABLE OF CONTENTS

Page

DEDICATION ii

ACKNOWLEDGEMENTS iii

LIST OF TABLES vi

LIST OF FIGURES vii

LIST OF ABBREVIATIONS xi

Chapter

I. INTRODUCTION 1

Field-effect Transistors 2
Alternative High-κ Gate Dielectrics 4
High-κ/Si Interface 5
Fabrication of Thin Dielectric Films 5
Characterization Techniques 6
Research Summary 9

II. THIN FILM CHARACTERIZATION TECHNIQUES 11

Backscattering Spectrometry 12
Kinematic Factor 12
Scattering Cross Section 16
Stopping Power 18
Straggling 22
Channeling 24
Time-of-Flight Medium Energy Backscattering 24
Spectrometer Efficiency 28
Backscattering Data 29
Backscattering Spectrum Simulation 31
Alternative Detection Systems 33
Spectroscopic Ellipsometry 34
Transmission Electron Microscopy 35
Atomic Force Microscopy 36

III. CALIBRATION AND EVALUATION OF TOF-MEBS SYSTEM 38

Energy calibration 38
Thickness Calibration 45
Stoichiometry Calibration 48
Backscattering Statistics 51
Conclusions 57

IV. INTERFACIAL ANALYSIS USING TOF-MEBS 58

Experimental Details 60
Data Analysis 60
Results and Discussion 61
Conclusions 71

V. EFFECTS OF MULTIPLE SCATTERING AND SURFACE ROUGHNESS ON BACKSCATTERING SPECTRA 72

Multiple Scattering 73
Surface Roughness 75
Experimental Details 76
Results and Discussion 80
Conclusions 87

VI. EVALUATION OF ENERGY AND DEPTH RESOLUTION WITH TOF-MEBS 88

Calculating Depth Resolution 90
Optimizing Depth Resolution 93
Experimental Procedure 98
Results and Discussion 100
Conclusions 109

VII. CHARACTERIZATION OF ZrO_2 FILMS DEPOSITED BY MOCVD ON HYDROGEN TERMINATED Si AND NATIVE Si OXIDE SURFACES 110

Experimental Details 111
Results and Discussion 113
ZrO_2 and Interfacial Layer Composition 113
Thin Film Density 121
Conclusions 124

SUMMARY AND CONCLUSIONS 125

A. SIMULATING AND FITTING BACKSCATTERING SPECTRA 127

REFERENCES 136

LIST OF TABLES

Table Page

1. Comparison of theoretical and experimental peak edges for 270 keV He^+ scattering from O, Al, and Hf. 40

2. Thickness comparisons of ZrO_2 films and interfacial layer determined by TOF-MEBS and TEM.......... 49

LIST OF FIGURES

Figure Page

1. Basic MOSFET structure 2

2. Thickness values obtained by various analytical techniques. 7

3. Diagram of elastic collision 13

4. Kinematic factor *K* for He^+ ions backscattering from different masses 15

5. Kinematic factor *K* for He^+ ions backscattering from Al at different scattering angles 15

6. Stopping cross sections for He^+ ions Al, SiO_2, and ZrO_2 as a function of energy 20

7. Energy straggling of He^+ ions in 100Å of Al, Zr, and Au as a function of projectile energy 23

8. Simulated channeled and random spectrum of 270 keV He^+ incident on 25Å SiO_2/Si 25

9. Geometry and major components of the time-of-flight system. 27

10. Raw time-of-flight spectrum of 270 keV He^+ incident on SiO_2/Si 30

11. Energy spectrum of 270 keV He^+ incident on SiO_2/Si 32

12. TOF-MEBS backscattering spectra of $HfAl_xO_y$ on Si indicating a shift in peak locations over time 40

13. The corresponding energy width of some flight time interval, 500 ns for this figure, is much greater at shorter flight times. 42

14. TOF-MEBS for 270 keV He^+ incident on $HfAl_xO_y$/Si. 44

15. Comparison of SE and TOF-MEBS thicknesses from ZrO_2 samples 47

16. Comparison of SE and TOF-MEBS thicknesses from SiO_2 samples 49

17. Cross sectional TEM image of ZrO_2 (59.7 Å)/$ZrSi_xO_y$ (11.1 Å)/Si 50

18. Stoichiometric ratio versus SiO_2 film thickness 52

19. Percent uncertainty versus integrated charge for O and Zr signals in time-of-flight spectrum 54

20. Standard deviation of ZrO_2 and Zr-silicate layer thickness versus integrated charge 56

21. Standard deviation of Zr and O atomic percent versus integrated charge 56

22. Computer simulations comparing He^+ backscattering at 1.8 MeV and 270 keV 62

23. Backscattering spectrum and simulation for 270 keV He^+ ions incident on $C/SiO_x/Si(100)$ 64

24. Backscattering spectrum and simulation from aluminum oxide film on Si(100) 65

25. Backscattering spectrum and simulation for 270 keV He^+ incident on $ZrO_2/Si(100)$ 67

26. Background function and simulated Zr signal 70

27. Residual χ^2 distribution for simulated 270 keV He^+ ZrO_2/Si backscattering spectra with and without background modification 70

28. Target geometry for Monte Carlo simulations 78

29. Simulations of backscattering spectra for 270 keV He^+ on 330 Å Ta/Si using a multiple and a single scattering model (15° exit angle) 81

30. Simulations of backscattering spectra for 270 keV He^+ on 330 Å Ta/Si using a multiple and a single scattering model (75° exit angle) 81

31. Single scattering simulation fit to the multiple scattering simulation using a five layer model 83

32. Experimental time-of-flight medium energy backscattering spectrum and simulation of 270 keV He^+ incident on 50 Å ZrO_2/Si 83

33. Simulations of backscattering spectra for 270 keV He^+ on 50 Å ZrO_2/Si using a multiple and a single scattering model (75° exit angle) 85

34. Lower energy edge of Zr signal 85

35. Two-dimensional view of rough ZrO_2 target used for MC simulations. 86

36. Variation in the path length and scattering angle.. 92

37. Energy loss factor [S] for 60, 170, and 270 keV He^+ in Al over tilt angles 0 to 55° 94

38. Stopping of H^+, He^+, Li^+, C^+, and N^+ projectiles in Al as a function of energy....... 95

38. Energy loss factor [S] for He^+ in Al (scattered from Er) as a function of beam energy.. 96

39. Stopping of H^+, He^+, Li^+, C^+, and N^+ projectiles in Al as a function of energy....... 96

40. Experimental geometry for TOF-MEBS analysis.. 99

41. Zirconium signal in a ZrO_2/Si spectrum obtained with 220 keV He^+ 99

42. 270 keV He^+ backscattering spectrum of ErAs heteroepitaxial materials system.. 101

43. Measured TOF spectrometer energy resolution versus detected particle energy .. 101

44. Depth resolution at the surface of Al as a function of detected energy 103

45. Calculated energy spread as a function of target tilt.. 103

46. Energy spread and depth resolution as a function of target tilt for 270 keV He^+ in ZrO_2 105

47. Total measured energy spread and depth resolution as a function of target tilt 105

48. TOF-MEBS depth resolution versus beam energy 107

49. Calculated depth resolution versus beam energy.. 107

50. ZrO_2/Zr-silicate/Si thin film model for backscattering spectra simulations 112

51. TOF-MEBS He^+ backscattering spectra of 30 Å ZrO_2 deposited on H-Si at 350° C with best fits from simulations and the χ^2 distribution 114

52. TOF-MEBS He^+ backscattering spectra of 30 Å ZrO_2 deposited on N.O. at 350° C with best fits from simulations and the χ^2 distribution 116

53. Atomic % of oxygen in 30 and 60 Å ZrO_2 films deposited on H-Si and N.O. at three different temperatures 118

54. Atomic % of zirconium in interfacial region of 30 and 60 Å ZrO_2 films deposited on H-Si and N.O. at three different temperatures 118

55. TOF-MEBS He^+ backscattering spectrum and simulation of SiO_x on Si 120

56. Atomic % of oxygen in interfacial region of 30 and 60 Å ZrO_2 films deposited on H-Si and N.O. at three different temperatures 120

57. Density of 30 and 60 Å ZrO_2 films deposited on H-Si and N.O. at three different temperatures 122

58. Simulated spectrum for 270 keV ^4He on 50 Å ZrO_2/ 15 Å SiO_2/Si 129

59. Simulated backscattering spectrum with a channeled substrate 130

60. Experimental TOF-MEBS spectra for 270 keV He^+ on ZrO_2/Si 132

61. Selected region of experimental TOF-MEBS spectrum 133

62. Backscattering spectrum and best fit simulation of 270 keV He^+ on 55 Å $Zr_{1.02}O_2$/ 26 Å SiO_2/Si 134

63. Residual χ^2 distribution 135

LIST OF ABBREVIATIONS

ADC	Analog-to-Digital Converter
AES	Auger Electron Spectroscopy
AFM	Atomic Force Microscopy
ALD	Atomic Layer Deposition
ARXPS	Angle Resolved X-ray Photoelectron Spectroscopy
CMOS	Complementary Metal Oxide Semiconductor
CVD	Chemical Vapor Deposition
ERDA	Elastic Recoil Detection Analysis
ESA	Electrostatic Energy Analyzer
FET	Field Effect Transistor
FWHM	Full Width Half Max
GIXPS	Grazing Incidence X-ray Photoelectron Spectroscopy
GIXR	Grazing Incidence X-ray Reflectivity
H-Si	Hydrogen-Terminated Silicon
LJ	Lenz-Jensen
MC	Monte Carlo
MCA	Multichannel Analyzer
MCP	Microchannel Plate
MEIS	Medium Energy Ion Scattering
ML	Monolayer
MOCVD	Metal Organic Chemical Vapor Deposition

MOSFET	Metal Oxide Semiconductor Field Effect Transistor
N.O.	Native Silicon Oxide
NIST	National Institute of Standards and Technology
NRA	Nuclear Reaction Analysis
QTH	Quartz Tungsten Halogen
RBS	Rutherford Backscattering Spectroscopy
RMS	Root Mean Squared
SE	Spectroscopic Ellipsometry
SIMS	Secondary Ion Mass Spectroscopy
SSBD	Silicon Surface Barrier Detector
TAC	Time-to-Amplitude Converter
TEM	Transmission Electron Microscopy
TOF	Time-of-Flight
TOF-MEBS	Time-of-flight Medium Energy Backscattering
UHV	Ultra High Vacuum
XPS	X-ray Photoelectron Spectroscopy
XTEM	Cross-Sectional Transmission Electron Microscopy
ZTB	Zirconium t-Butoxide

CHAPTER I

INTRODUCTION

In 1965 Gordon Moore observed an exponential growth in the number of transistors per integrated circuit.[1] His observation became known as Moore's law, which states that the number of transistors on a chip is expected to double about every 2 years. At the time Moore made his observation, the number of transistors in an integrated circuit was about 400. The number today is an impressive 400 million. Billion transistor chips should be possible by the end of the decade. The trend of decreasing transistor size, driven by the desire for increased switching speeds and reduced power consumption, has required a continuous decrease in the physical dimensions of the various components of a transistor.[2] One physical parameter that is particularly important in this scaling process is the thickness of the SiO_2 gate dielectric. However, as the thickness of the gate dielectric decreases, high leakage current and reduced drive current become fundamental limitations to further scaling.[3] These limitations can be avoided by using a thicker dielectric film with a permittivity higher than that of SiO_2. It is this search for a material to replace SiO_2 as the gate dielectric that ultimately motivates this research. The center piece of this work is a unique characterization tool called time-of-flight medium energy backscattering (TOF-MEBS). This work focuses on the analytical capabilities of the TOF-MEBS system and its application to characterizing thin dielectric films and their interface with Si.

Field-effect Transistors

The explosion in microelectronic device performance is largely due to the miniaturization of the metal oxide semiconductor field effect transistor (MOSFET), the most common field-effect transistor (FET) in use today.[4] The major components of a MOSFET (Figure 1) are the source, drain, gate and gate dielectric, channel, and substrate. Figure 1 shows an n-channel MOSFET, which consists of n^+ source and drain regions in a uniformly doped p-type substrate. By applying a positive voltage to the gate, charge accumulates on both sides of the gate dielectric. If enough charge is accumulated, a conduction channel forms between the source and drain and current is enabled to flow between the two regions.

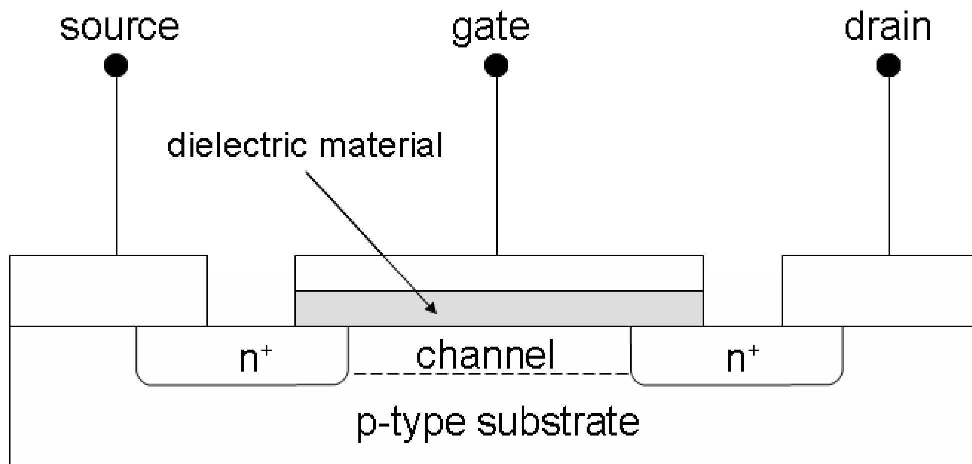

Figure 1. Basic MOSFET structure

The time required to form this conductive channel (switching speed) depends, in part, on the gate capacitance, where a higher capacitance offers improved performance. The capacitance, C, of a gate structure, which can be modeled as a parallel plate capacitor, is given by

$$C = \kappa\varepsilon_o A/t, \qquad \text{(I-1)}$$

where κ is the dielectric constant (also called relative permittivity), ε_o is the permittivity of free space, A is the capacitor area, and t is the dielectric film's thickness. The scaling of device feature size implies a reduction in the channel length. Shortening the channel length requires that the area of the gate dielectric also decreases, which results in a reduction in C. In order to maintain a desired capacitance for a decrease in gate area, the dielectric thickness must also decrease. However, below a certain thickness, high leakage current and reduced drive current become fundamental limitations to further scaling.[3] This problem can be avoided by using a thicker dielectric material with a permittivity (κ) higher than SiO_2.[2]

The gate dielectric is the region of the MOSFET that separates the metal gate from the semiconductor substrate. SiO_2 has been used widely as the insulating material for MOSFET structures for a number of reasons: it is amorphous, thermodynamically and electrically stable on Si, forms a high-quality interface with Si, and has a low defect charge density.[3] The continued use of SiO_2 as the gate oxide is due to the facts that it is the native oxide to Si, and that a considerable knowledge base has been acquired for the oxidation process.[5] However, as the thickness of a SiO_2 layer is decreased, a variety of

problems arise: reduced drive current, high leakage current, penetration of impurities from the gate into the gate dielectric, and reliability and lifetimes of the devices using these thin films.[2] Although transistors intended for high-performance microprocessor applications can sustain leakage current densities as high as 10 A/cm^2,[2] low-power applications require transistors with leakage currents as low as ~10^{-3} A/cm^2.[6] At a SiO_2 thickness of 1.5 nm, gate leakage is as high as, ~1 A/cm^2.[7]

Alternative High-κ Gate Dielectrics

Any materials system under consideration as an alternative gate dielectric must meet a set of criteria to perform successfully. Key guidelines for selecting an alternative gate dielectric have been outlined by Wilk, Wallace, and Anthony.[2] Guidelines that are most relevant to this study are: thermodynamic stability on Si, interface quality, and film morphology. Many dielectric materials have been investigated but very few appear promising with respect to all the guidelines listed above.

High-κ gate dielectric candidates that have received considerable attention include the group IIIB metal oxide Al_2O_3,[8-13] the group IVA metal oxides ZrO_2,[14-18] and HfO_2,[19-23] and the group VA oxide Ta_2O_5.[24-26] Also under consideration are binary alloys, such as $ZrAl_xO_y$,[27, 28] which attempt to combine the desirable qualities of the two metal oxides while eliminating the undesirable properties of each individual material. Metal silicates such as Zr and Hf-silicates are also promising materials because they exhibit high thermal stability in direct contact with Si.[29-31]

High-κ/Si Interface

The gate dielectric/Si interface is a dominant factor in determining the overall electrical properties of the gate structure and must maintain a high quality after complimentary metal oxide semiconductor (CMOS) processing conditions while in contact with Si.[2] Many of the high-κ materials under consideration are not thermodynamically stable in contact with Si and react to form an interfacial layer. Thermodynamic instability can be reduced by adding SiO_2 to metal oxides; although, the overall permittivity is lower than that of the pure metal oxide. Due to the high quality interface with Si, this SiO_2 layer will also help maintain high channel carrier mobility. However, such a low-κ layer would limit the highest possible capacitance achievable by the gate stack.[2]

Fabrication of Thin Dielectric Films

A variety of methods are available for fabricating high-κ dielectric films. These methods include filtered vacuum arc,[32] plasma sputtering,[27, 33] physical vapor deposition,[34] and atomic layer deposition (ALD).[10, 19, 35] One of the most widely studied fabrication methods and also most commonly used in industry is metal organic chemical vapor deposition (MOCVD), which derives its name from the use of metal-organic precursors. This method was used for depositing many of the films studied in this work. Variations of MOCVD include rapid thermal,[34, 36] low temperature,[37] low pressure,[38, 39] and atmospheric pressure.[40] Typical MOCVD experiments are performed with temperatures ranging from less than 250 ºC to greater than 550ºC. Reactor pressures range from atmospheric to less than 10^{-5} torr. Pressure, temperature, and carrier gas flow rate are deposition parameters that are important determinants of film properties. These

parameters can affect material properties such as stoichiometry, thickness, density, crystallinity, and morphology. The optimization of these process parameters to achieve quality film structures comprises much of the current alternative high-κ dielectric research.

Characterization Techniques

The demand for alternative gate dielectrics has also put pressure on the physical characterization techniques necessary to determine the structure and composition of a given film.[41] Characterization of dielectrics in CMOS devices with a thickness of only a few monolayers will require improved techniques for chemical and electrical analysis.[42]

Standard methods for determining composition and thickness encounter difficulties below about 10 nm. These difficulties are aptly illustrated by a study conducted by SEMATECH, an international consortium focused on semiconductor manufacturing technology. Six techniques were used to determine the thickness of silicon oxynitride samples circulated in a round-robin study The reported variation between the total measured thicknesses was on the order of 50%, as shown in Figure 2.[43]

Reasons noted for the spread in the results included the accuracy of the physical quantities used in the methods, the physical limitation in the accuracy of the method on such a small scale, diffusion in the layers, and incomplete understanding of the physical and chemical nature of the materials.[43] A specific limitation of x-ray photoelectron spectroscopy (XPS) is the required knowledge of photoemission cross-sections and photoelectron mean escape-depths. In order to determine film thickness with grazing incidence x-ray reflectivity (GIXR), film composition must be known. The interpretation

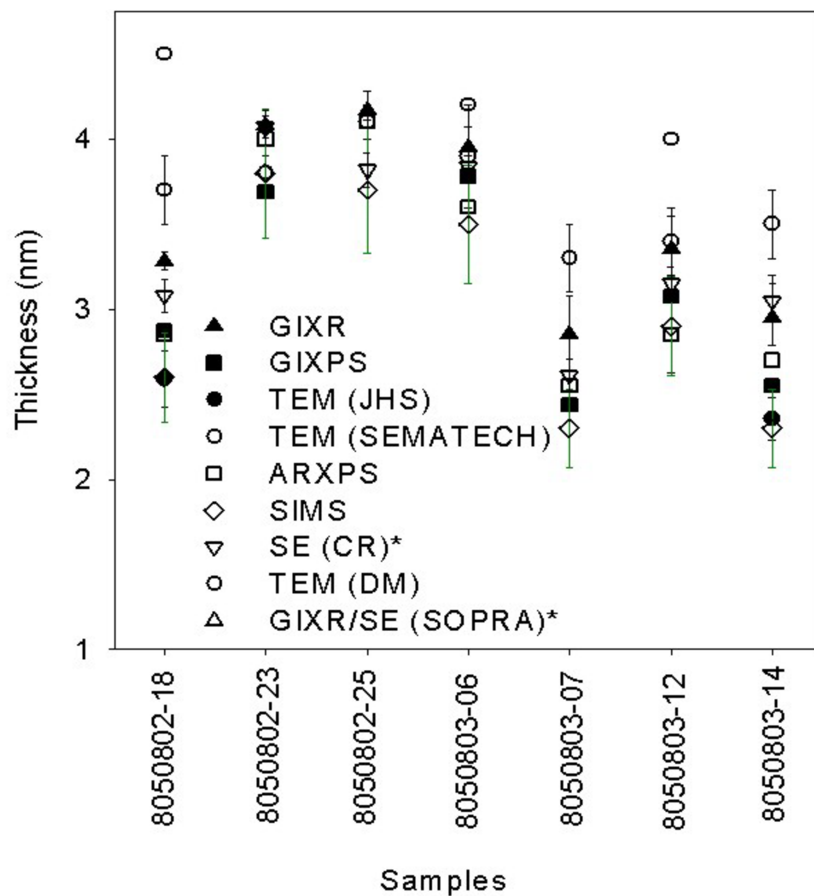

Figure 2. Thickness values obtained by various analytical techniques. GIXR: grazing incidence x-ray reflectivity; GIXPS: grazing incidence x-ray photoelectron spectroscopy; TEM: transmission electron spectroscopy; ARXPS: angle resolved XPS; SIMS: secondary ion mass spectroscopy; SE: spectroscopic ellipsoimetry.[43]

of spectroscopic ellipsometry (SE) data depends on the assumed thin film model and the optical constants. Although transmission electron microscopy (TEM) provides a visual image of film's thickness, this value is subject to the viewer's interpretation of the location of the film boundary. Secondary ion mass spectrometry (SIMS) measures depth by determining the time required to sputter through a layer. However, results are complicated by variations in the sputter rate and by ion beam mixing, which can lead to broadening of the interface.[44]

Although the study conducted by SEMATECH did not include any ion beam analysis (IBA) techniques, such as Rutherford backscattering spectrometry (RBS) and TOF-MEBS, these methods also have their limitations concerning materials analysis at nanometer scales. In order to obtain a physical thickness value, the mass density of the material must be assumed. The assumed density value can be a serious source of uncertainty, especially for thin film where materials properties can be different from bulk properties. An additional source of uncertainty is the amount of energy loss per distance traveled experienced by the probe ion, which is quantified by the stopping power. Stopping powers for compounds are typically unknown and must be approximated.

The search for alternative high-κ dielectric materials relies heavily on characterization techniques that provide electrical and materials properties of the high-κ materials. Dielectric films need to be characterized to determine if a certain material system satisfies the stringent set of guidelines set for alternative high-κ materials. Characterization results will also aid in understanding the deposition process of high-κ gate dielectrics. Such an understanding is important for achieving dielectric films with reproducible electrical and materials properties.[45]

Research Summary

As part of a larger effort to develop a materials system for the replacement of SiO_2 as a gate dielectric material, this work investigates the analytical capabilities of TOF-MEBS as a novel materials characterization tool. Prior to this work, the use of the TOF system for the study of thin dielectric films was limited; therefore, a large portion of this thesis is dedicated to the work performed to calibrate the TOF system and to better understand its analytical capabilities. The characterization ability of the TOF system at depths of a few nanometers is of particular interest because the importance of the physical and chemical nature of the interfacial region between the gate dielectric and underlying Si. Dielectric materials that were studied in this work include Al_2O_3, SiO_2, and ZrO_2. Since ZrO_2 is a promising candidate as a high-κ gate dielectric, this material was of particular interest. TOF-MEBS was used to characterize ZrO_2 films and their interface with different deposition surfaces.

Chapter II discusses in detail the physical concepts involved in backscattering analysis and touches on other characterization methods used in this study. Chapters III-VI address studies on the TOF-MEBS technique. Chapter III describes the calibration of the TOF system with respect to energy, thickness, and stoichiometry. This chapter also presents a study performed to evaluate the uncertainty and reproducibility involved in TOF-MEBS experiments. Chapter IV evaluates the use of the TOF-MEBS system for the study of the interfacial region between dielectric materials and Si. This chapter discusses the approach used throughout this work for analyzing TOF backscattering spectra and extracting information on the interfacial region. Two factors that significantly limit the depth resolving capabilities of backscattering experiments is multiple scattering and

surface roughness. A study performed to better understand how these factors can interfere with TOF-MEBS results is presented in Chapter V. An additional study that covers the various factors limiting depth resolution is presented in Chapter VI. This chapter discusses the experimental configuration for optimizing the depth resolution of the TOF system. Chapter VII is devoted to the application of the TOF system for studying the high-κ candidate material ZrO_2, which was deposited on two different deposition surfaces, hydrogen terminated Si and native Si oxide.

CHAPTER II

THIN FILM CHARACTERIZATION TECHNIQUES

The majority of the thin film characterization in this work was performed with Vanderbilt's TOF-MEBS system. Backscattering spectrometry is an analytical technique in which an energized beam of particles is directed at a material's surface. By measuring the energy and yield of backscattered particles, information can be obtained concerning atomic composition, elemental areal density, and impurity distribution. Conventional backscattering spectrometry, Rutherford backscattering spectrometry (RBS), uses ion energies in the MeV range and a solid state detector. TOF-MEBS is a medium energy version of RBS that detects backscattered particles with a time-of-flight spectrometer, which offers improved depth resolution and sensitivity. In practice, medium energy refers to ion energies in the range of a few tens to a few hundreds of kilo-electron-volts (keV). A physical meaning of medium energy is given later in this chapter in the section on scattering cross-sections.

Additional characterization tools used in this work include atomic force microscopy (AFM), spectroscopic ellipsometry (SE), and transmission electron microscopy (TEM). AFM was used to measure surface roughness. SE and TEM where used to obtain film thicknesses.

Backscattering Spectrometry

There are four main physical concepts that give backscattering spectrometry its characterization capabilities, which include: (1) elastic two-body collisions where energy is transferred from a projectile to a target nucleus; (2) the probability that such a two-body collision takes place; (3) energy loss a projectile experiences when traversing matter; and (4) statistical fluctuations in the energy of projectiles traversing matter.
These physical interactions lead to the concepts on the kinematic factor, scattering cross section, stopping power, and energy straggling, respectively, and are discussed in detail in the following sections.

Kinematic Factor

In backscattering analysis, the monoenergetic particles that comprise the incident beam collide with target atoms. A small fraction of these collisions cause the primary particle to backscatter into a detector which measures their energies. The energy of scattered particles depends on the mass, M_1, and initial energy, E_0, of the projectile, the mass of the target atom, M_2, and the geometry of the scattering event, as shown in Figure 3.

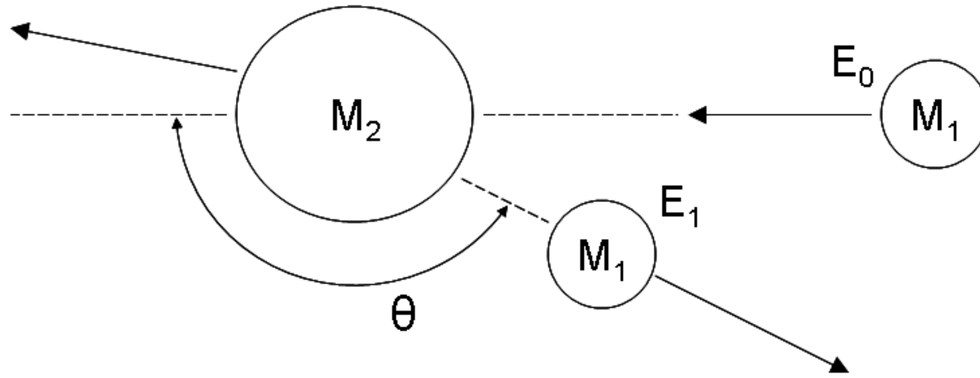

Figure 3. Diagram of elastic collision between a projectile of mass M_1, and initial energy E_0 and a stationary target mass of M_2.

After the collision, energy is transferred from M_1 to M_2 and the projectile scatters at an angle of θ with energy of E_1. For a perfectly elastic collision, the energy of the projectile after the collision is directly proportional to the projectile's initial energy (E_0). The ratio of the two energies is called the kinematic factor K,

$$K_i = E^i_1/E_0. \qquad \text{(II-1)}$$

The transfer of energy in an elastic collision between the two isolated particles can be determined by applying the principles of conservation of mass and momentum. Thus, the kinematic factor in terms of the projectile mass M_1, the target atom mass M_2, and the reaction angle θ, is given by the following equation:

$$K = \left[\frac{\left(M_2^2 - M_1^2 \sin^2\theta\right)^{1/2} + M_1 \cos\theta}{M_1 + M_2}\right]^2. \qquad \text{(II-2)}$$

Equation (II-2) indicates that K is larger for heavier targets and larger reaction angles. Figure 4 presents the kinematic factor as a function target mass for He^+ ions backscattering at 150°. Figure 5 plots the kinematic factor for He^+ ions backscattering off Al at various scattering angles. In order for backscattering to occur ($\theta > 90°$) the projectile mass must be greater than that of the target atom, $M_1<M_2$. Light projectiles such as H^+ and He^+ are typically used in backscattering experiments so that a wide range of target masses can be analyzed.

The ability of the backscattering system to distinguish between target atoms with a mass difference δM_2 is determined by the ability of the system to resolve energy differences, δE, of backscattered particles. The mass resolution of the system is given by

$$\delta M_2 = \frac{\delta E}{E_0\left(\frac{dK}{dM_2}\right)}. \tag{II-3}$$

Mass resolution can be improved by increasing the incident energy, E_0; using a larger projectile mass, M_1; using scattering angles close to 180°; or by improving the overall energy resolution, δE. Since the beam energy of the TOF-MEBS systems is limited to less than 300 keV and the scattering angle is fixed at 150°, mass resolution can be improved by using heavy ions or by increasing the overall energy resolution. The total energy resolution contains contributions from factors such as the detector resolution, energy straggling, and multiple scattering, which are sensitive projectile mass. These and other factors will be discussed in more detail in Chapters V and VI.

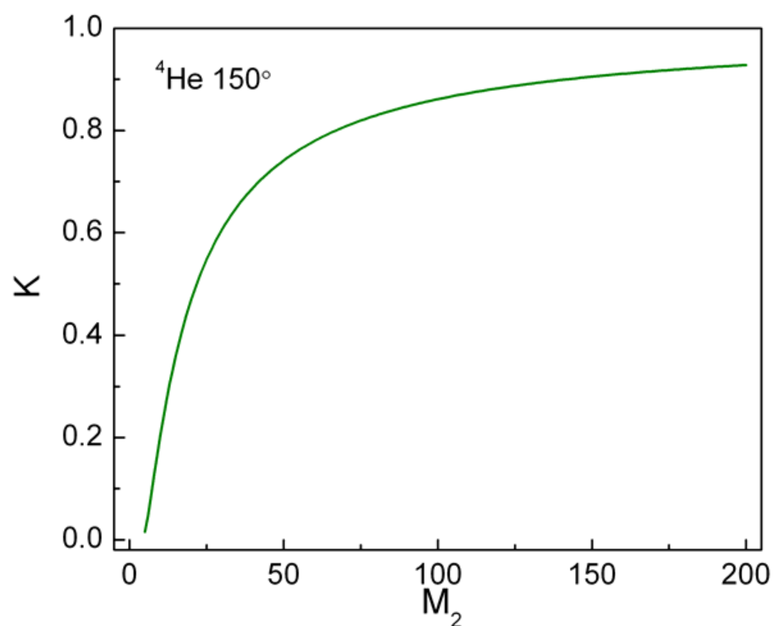

Figure 4. Kinematic factor *K* for He^{+} ions backscattering from different masses. The scattering angle is 150°., M_2, at a scattering angle of 150°.

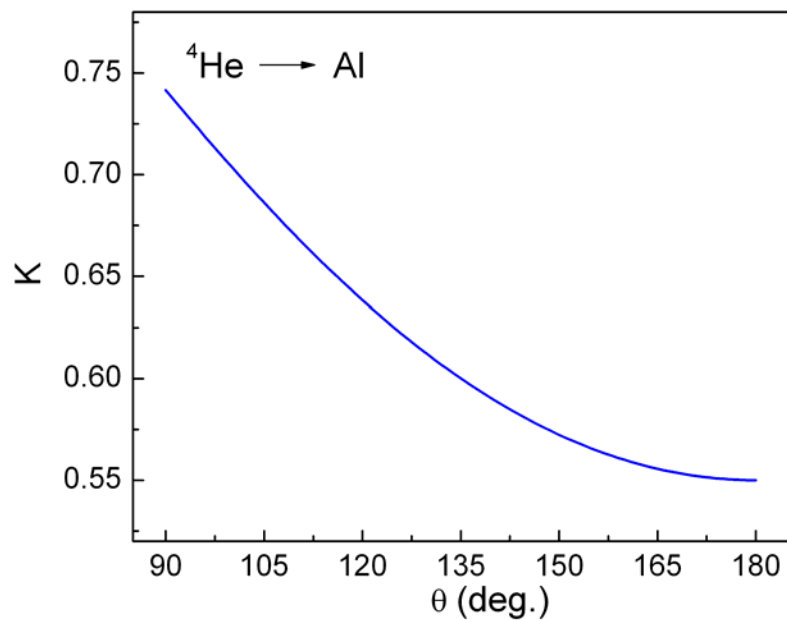

Figure 5. Kinematic factor *K* for He^{+} ions backscattering from Al at different scattering angles.

Scattering Cross Section

The probability, P, that a particle will be backscattered from a sample with areal density Nt into the detector solid angle Ω is given by the ratio of the number of detected particles, Y, to the number of incident particles, Q:

$$P = \frac{Y}{Q}. \qquad \text{(II-4)}$$

The yield of backscattered particles depends, in part, on the differential cross section, $d\sigma/d\Omega$, which simplifies to $\sigma(E, \theta)$ for small detector solid angles ($\Omega < \sim 10$ msr) and well defined scattering angles θ.[46] By assuming the Coulomb force between the incident and target nuclei, an unscreened Rutherford cross section may be calculated from the following:

$$\sigma(E,\theta) = \left(\frac{Z_1 Z_2 e^2}{4E}\right)^2 \frac{4}{\sin^4\theta} \frac{\left([1-((M_1/M_2)\sin\theta)^2]^{1/2} + \cos\theta\right)^2}{[1-((M_1/M_2)\sin\theta)^2]^{1/2}}, \qquad \text{(II-5)}$$

where Z_1, M_1 and Z_2, M_2 are the atomic number and mass of the incident ion and target atom, respectively, E is the energy of the ion immediately before scattering, e is the electronic charge, and θ is the scattering angle. Actual cross sections can deviate from the Rutherford description at both high and low energies for all projectile-target pairs. Ion beam techniques are termed *medium energy* if the beam energy is low enough that the cross sections deviate from unscreened Rutherford value by more than about a percent.[47]

These departures are caused by partial screening of the nuclear charges by the electron shells surrounding both nuclei. A general rule for the range of validity of the Rutherford cross section states that the cross section should be within 4% of the Rutherford cross section and that the lower energy limit of Equation (II-4) is $0.03Z_1Z_2^2$ keV.[47]

Due to the low beam energies used in this work, compared to the MeV energy used in RBS analysis, departures from the Rutherford value must be considered. Cross-sections at low energies are well described by the Lenz-Jensen (LJ) screened Coulomb potential.[47] In this work, LJ cross sections are calculated using an algorithm developed by Mendenhall and Weller.[48, 49] For a 270 keV He^+ projectile scattering from Si, cross sections deviate from the Rutherford value by less than a percent. For a heavier scattering target like, Zr, which has an atomic number of 40, the departure from the Rutherford value is about 5%.

The areal density, *Nt* (atoms/cm^2), of an element can be determined with knowledge of σ, Ω, the integrated peak count A_i, and the total charge collected Q, such that

$$(Nt)_i = \frac{A_i \cos\theta_1}{Q \cdot \sigma_i(E,\theta)\Omega}, \qquad \text{(II-6)}$$

where N is the atomic density of the *i*th element, t is the physical film thickness, and θ_1 is the angle between the incident beam and target normal. The average atomic ratio for a film containing the A_mB_n can be calculated by taking the ratio of atomic densities:

$$\frac{n}{m} = \frac{N_B}{N_A} = \frac{A_B}{A_A} \cdot \frac{\sigma_A(\theta,E)}{\sigma_B(\theta,E)}, \qquad \text{(II-7)}$$

where A_i is the same as in Equation (II-6). Equation (II-7) enables one to calculate stoichiometric ratios without knowledge of the quantities Q and Ω, which can be difficult to measure accurately.[50]

Areal density, $(Nt)_i$, can be converted to a physical film thickness, t, if the mass density, ρ_{AB} of the film is known:

$$t = \frac{(Nt)_A}{N_A^{AB}} = \frac{(Nt)_B}{N_B^{AB}}. \tag{II-8}$$

The atomic densities are defined as

$$N_A^{AB} = \frac{m\rho_{AB} N_0}{M_{AB}}; N_B^{AB} = \frac{n\rho_{AB} N_0}{M_{AB}}, \tag{II-9}$$

where N_0 is Avogadro's number and $M_{AB} = mM_A + nM_B$ is the molecular weight of compound A_mB_n.

Areal densities obtained from Equation (II-6) have an uncertainty of about ±3%. The uncertainty of average stoichiometric ratios determined by Equation (II-7) is a few tenths of 1%. Since film densities are usually unknown, the uncertainty in the physical film thickness is unknown.[50]

Stopping Power

The energy loss experienced by an ion traversing matter gives backscattering spectroscopy its depth profiling capability. The amount of energy the ion loses per

distance traveled in matter is given by the stopping power of the material, which depends on the masses of the ion and the material traversed and the energy of the ion. The energy loss process is due to many kinds of interactions between the projectile ion, target nuclei, and target electrons,[50] and can be viewed as an average over all possible energy dissipative processes activated by the projectile as it passes an atom.[51] A primary assumption that is made in theories quantifying the stopping of ions in matter is that these interactions are due only to electromagnetic forces and that any energy loss to nuclear reactions between the projectile and target nuclei can be ignored.[52]

Stopping powers are typically expressed in terms of the stopping cross section, ε, which is the energy loss per unit areal density. Typical units for ε are eV $cm^2/(10^{15}$ atoms) . The stopping cross section is related to the amount of energy loss per physical thickness traversed by

$$\varepsilon \equiv \frac{1}{N}\frac{dE}{dx}, \qquad \text{(II-10)}$$

where N is the atomic density in atoms (or molecules)/cm^3. Figure 6 shows stopping cross sections for He^+ ions in Al, SiO_2, and ZrO_2 as a function of energy. Stopping decreases at lower velocities (lower energy) because projectiles may capture electrons from the target and partially neutralize its nuclear charge. In the high energy regime, the stopping cross section decreases with increasing velocity because the projectile spends less time in the vicinity of the atom.[53]

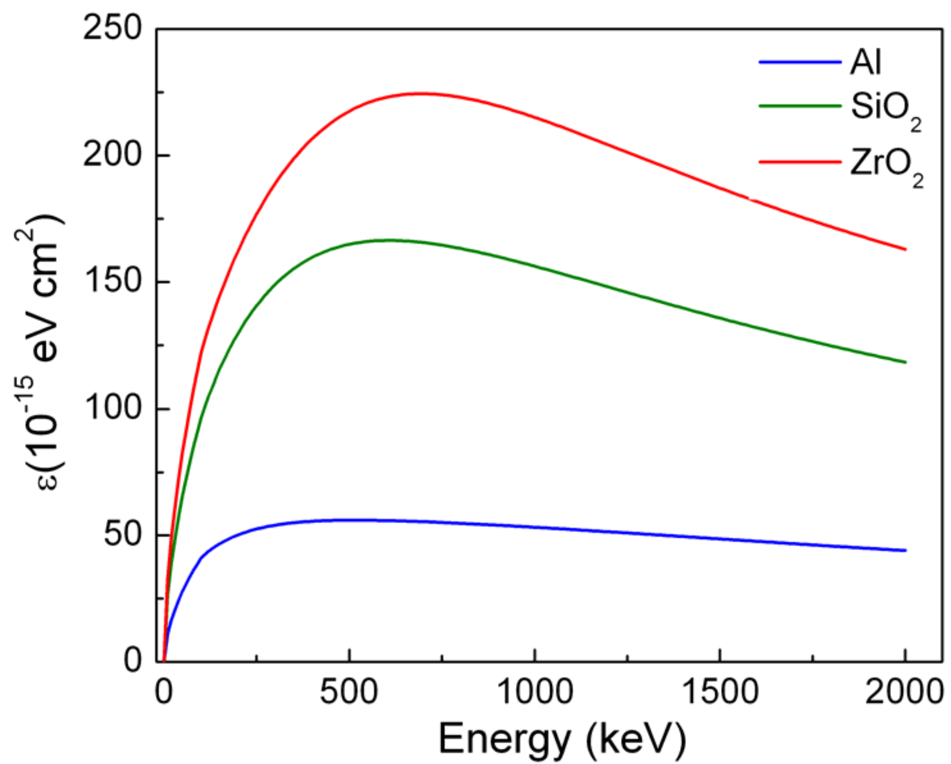

Figure 6. Stopping cross sections for He^+ ions in Al, SiO_2, and ZrO_2 as a function of energy. Stopping cross sections have a maximum between 0.5 and 1.0 MeV for He^+ in most materials.

The energy loss, ΔE, of ions traversing matter is energy dependent and can be calculated by integrating the stopping power, *dE/dx*:

$$\Delta E = \int \frac{dE}{dx} dx . \qquad \text{(II-11)}$$

For the case of thin targets, stopping power can usually be regarded as constant, and so energy loss can be approximated using the following:

$$\Delta E = Nx\varepsilon(E) , \qquad \text{(II-12)}$$

where E is taken as the initial beam energy, E_0 (surface energy approximation), or the mean energy of the analysis ion over pathlength x (mean energy approximation).

To determine the stopping of ions in compounds, an approximation called Bragg's rule is used. The compound stopping cross section in terms of energy loss/molecule/cm^2 traversed for a compound A_mB_n can be approximated by

$$\varepsilon^{A_mB_n} = m\varepsilon^{A} + n\varepsilon^{B} . \qquad \text{(II-13)}$$

This approximation assumes that each target atom independently contributes to the energy loss process and ignores the effects of chemical bonding in the compound.[51] Deviations from Bragg's rule are most pronounced around the stopping maximum for light organic gases and for solid compounds containing heavy constituents, such as oxides and nitrides.[54] A number of models have been developed to account for chemical

state effects.[55-57] Experimental measurements of the stopping of He^+ ions in dielectric materials such as SiO_2 [58, 59] have been performed, but none have been reported for the stopping of He^+ in other dielectric materials such as Al_2O_3 and ZrO_2.

Straggling

The energy loss by particles traversing matter is subject to statistical fluctuations. These fluctuations, called energy straggling, Ω_B, can significantly limit depth resolution. A straggling model derived by Bohr predicts that for a layer of thickness t, straggling has the variance

$$\Omega_B^2 = 4\pi (Z_1 e^2)^2 N Z_2 t \ . \tag{II-14}$$

This model assumes that an individual energy transfer takes place between a free stationary electron and a fully ionized projectile of charge $Z_1 e$, which is only fulfilled at high energies (~>0.5 MeV). More realistic straggling models can be obtained by considering the local electron density of the target or applying a more realistic model for the atomic electron density.[60] In this work energy straggling is calculated using the empirical formulae derived by Yang and coworkers.[60] Energy straggling increases with path length, and is greater for heavier projectiles and target atoms and larger areal densities. An additional factor that affects straggling is the energy of the projectile, which is not included in Bohr's model. Figure 7 shows energy straggling as a function of energy for ^4He ions in 100Å of Al, Zr, and Au. Straggling increases with energy up to 1-2 MeV, beyond which it is nearly constant.

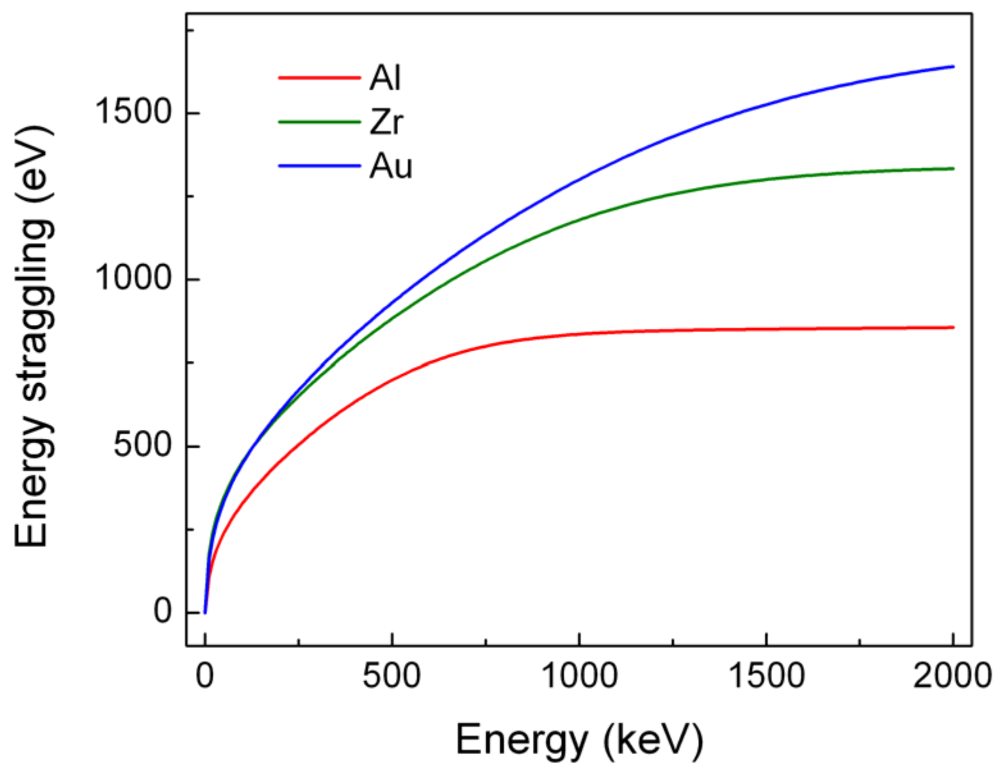

Figure 7. Energy straggling of He^+ ions in 100 Å of Al, Zr, and Au as a function of projectile energy. Straggling was calculated from Yang and coworkers empirical formulae.[60]

Channeling

The arrangement of atoms in single crystals determines the magnitude of incident ion-target interactions.[61] Channeling of energetic ions occurs when the beam is aligned with major planes of atoms in a single crystalline arrangement. The result is a reduction in backscattering yield from the material. Channeling analysis can be used to increase sensitivity to light elements by channeling the crystal substrate beneath an amorphous film. By reducing the substrate signal, the signal from light elements superimposed on the substrate signal is enhanced, and thus, sensitivity is improved. For the analysis of a Si(100) crystal substrate, axial channeling in the ⟨110⟩ direction can be achieved by tilting the normal of the substrate 45° relative to the beam. Figure 8 compares a random and a channeled backscattering spectrum obtained from 270 keV He^+ incident on native silicon oxide on Si(100). The Si peak in the channeled spectrum is due to contributions from the native oxide layer and from the first few monolayers of the Si substrate.

Time-of-Flight Medium Energy Backscattering

TOF-MEBS is a lower energy, high-resolution derivative of conventional RBS that uses a time-of-flight spectrometer for the detection of backscattered particles. The use of a time-of-flight spectrometer for medium energy ion scattering was first reported by Mendenhall and Weller.[62] Time-of-flight spectrometry functions by measuring the time it takes for the backscattered projectile particle to travel a fixed distance. Since the mass of the projectile and the length of the flight path are known, the kinetic energy of a backscattered particle can be obtained.

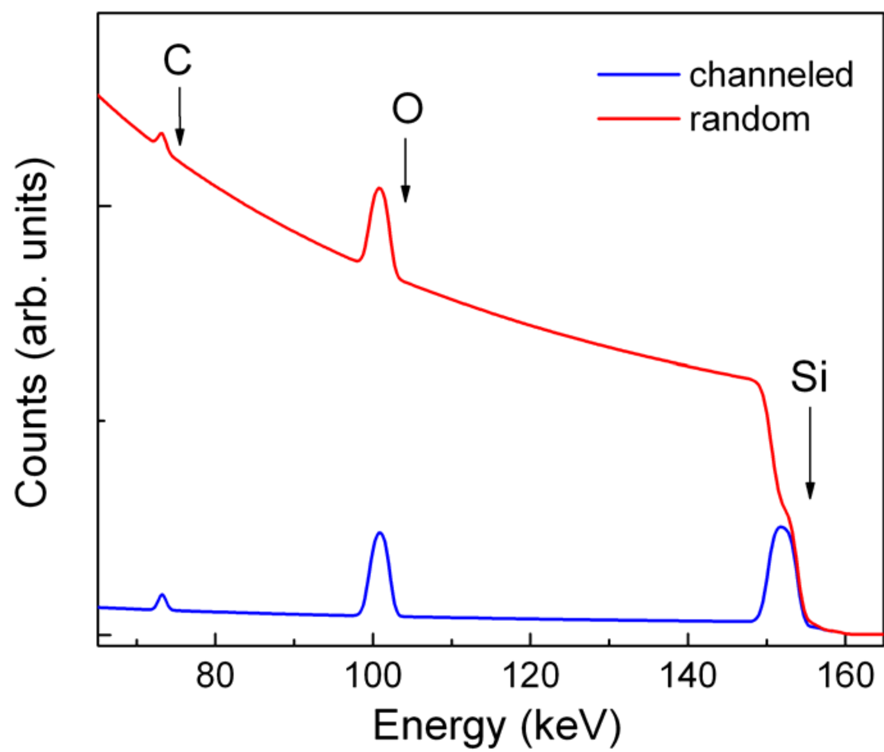

Figure 8. Simulated channeled and random spectrum of 270 keV He^{+} incident on 25Å SiO_2/Si. The beam was channeled in the ‹110› axial direction.

The beam line and the analysis chamber of the TOF-MEBS system are maintained at high vacuum where the pressure in on the order of 10^{-8} torr. Samples are manipulated in the analysis chamber with a 5-axis goniometer. By having multiple degrees of freedom for manipulating the sample, the sample can be easily oriented for channeling analysis.

The measurement of the flight time is represented by the time interval between a start of stop signal. The start signal is generated by detecting secondary electrons that are produced by ions passing through a thin carbon foil. The foil is sufficiently thin that an ion will pass though with minimal energy loss and change in trajectory.[47] A schematic of the TOF system is shown in Figure 9. The length of the flight path is 112 cm. The major components of the TOF-MEBS system are the start and stop detectors, timing discriminators, and time-to-amplitude converter (TAC). The particle detection systems are Galileo FTD-2003 microchannel plates (MCP), which generate start and stop pulses that are a fraction of a volt. The pulses are coupled with a timing discriminator (Phillips 6315) whose function is to produce uniform time markers that are insensitive to pulse amplitude. The TAC (Ortec 566) produces an output pulse whose height is proportional to the time difference between the start and stop signal. Signal processing is completed when the pulse from the TAC travels to a Canberra Series 40 multichannel analyzer (MCA). The main part of the MCA is the analog-to-digital converter (ADC). The ADC analyzes the maximum amplitude of each pulse and outputs a number (between 1 and 8191) that is proportional to the height of the input pulse. This number corresponds to a memory address, or channel, which is incremented by one each time one pulse of with a particular amplitude is accumulated.[63] The measured flight time is related to the channel

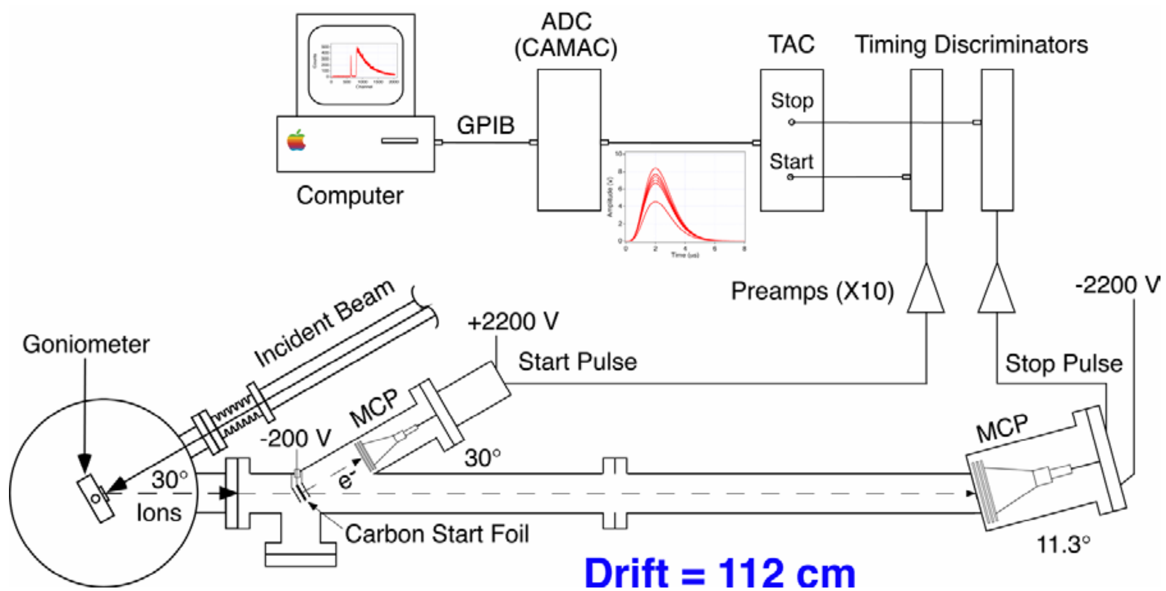

Figure 9. Geometry and major components of the time-of-flight system.[64] The drift length is 112 cm.

by a linear relationship, which is determined by calibrating the ADC. Chapter III addresses the ADC calibration.

Spectrometer Efficiency

The most common particle detector used for ion beam materials analysis with light MeV projectiles is the Si surface barrier detector.[63] However, at lower particle energies of tens to hundreds of keV, TOF detectors are better tools of choice, especially for heavy ions.[65] Unlike surface barrier detectors, which have near unit intrinsic efficiency, TOF spectrometers have an energy-dependent efficiency which can be considerably less than one.[65]

The intrinsic efficiency of the spectrometer is defined as the probability that a particle passing through the start foil will lead to the generation of a valid event. There are a number of factors that determine spectrometer efficiency, including secondary electron yield of the start foil, the probability that electrons reach the start detector, the start detector's efficiency for electrons, small angle multiple scattering in the start foil, the efficiency of the stop detector for ions.[65] Arps and Weller measured the efficiency of the TOF system using hydrogen, helium, and carbon ions in the energy range 50-275 keV.[66] Efficiency was found to increase with energy up to a few hundred keV, except for hydrogen, where efficiency reached a maximum around 100 keV. The study also showed that efficiency degrades for heavier projectile masses. An efficiency model capable of predicting the energy dependent performance of the TOF spectrometer was developed by Weller and coworkers.[65] The model includes the effects of secondary electron yield, multiple scattering in the foil, and the response of the MCP.

Backscattering Data

In TOF spectrometry, the flight time of the projectile is related to the primary energy of the projectiles, the masses of the target and projectile, and the length of the flight path. Lower flight times correspond to higher backscattered particle energies. A TOF spectrum of SiO_2 on Si is shown in Figure 10. The target was oriented 45º to a 270 keV He^+ beam. The axis labeled *Channel* refers to the channel number of the MCA. The width of each channel is the same and is around 122 ns.

A TOF spectrum can be converted to the energy domain using the kinetic energy equation,

$$E = \frac{1}{2} M_1 \left(\frac{d}{t} \right)^2 , \qquad \text{(II-15)}$$

where t is the flight time and d is the drift length of the spectrometer. However, this is not the preferred method.[47] Instead, the integral form of this equation is used:

$$\int_0^E P_E(E')dE' = \int_{t(E)}^{\infty} P_t(t')dt' , \qquad \text{(II-16)}$$

where $P_t(t')$ is the time domain spectrum and $P_E(E')$ is the equivalent energy domain spectrum. This conversion is preferred over simply using Equation (II-15) because it accurately preserves the total number of counts and computation takes just a few seconds.[47] Time-to-energy conversions are performed with *Mathematica* using the

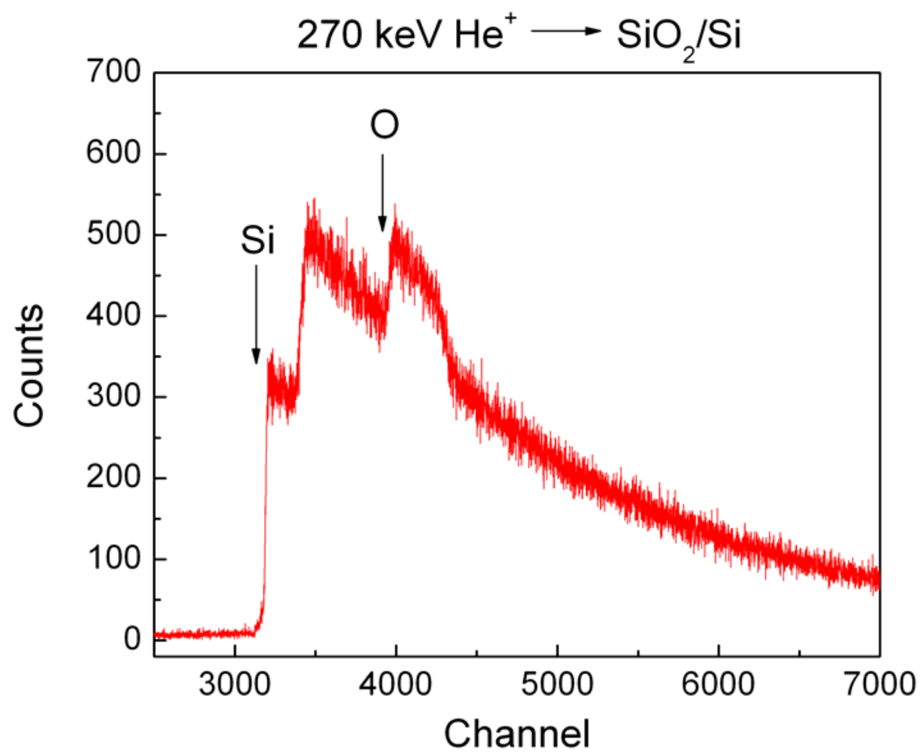

Figure 10. Raw time-of-flight spectrum of 270 keV He^+ incident on SiO_2/Si. Higher channel numbers correspond to lower backscattered energies.

package written by Weller called *Rebinning_ToF_Spectra*.[67] *Rebinning_ToF_Spectra* also performs a correction for spectrometer efficiency. TOF data converted to the energy domain and corrected for spectrometer efficiency are shown in Figure 11. The efficiency correction most strongly affects the lower energy portion of the energy spectrum because the spectrometer's efficiency decreases with particle energy. The resulting spectrum can be analyzed like a standard RBS spectrum from which elemental concentration and thickness can be extracted.

Backscattering Spectrum Simulation

A variety of computer programs are available for simulating backscattering spectra. Such programs include *RBSTools*,[67] *Data Furnace*,[68] *RUMP*,[69] *RBX*,[70] *SPACES*,[71] and SIMNRA.[72] SPACES and SIMNRA have the additional capability of being able to account for multiple scattering effects. However, simulations times are significantly longer. *RBSTools*, implemented in *Mathematica*, was developed by Weller and is currently used at Vanderbilt University for simulating high and medium energy backscattering spectra. The computation of a backscattering spectrum is handled in this package by the function *SimulateRBS* and requires as arguments a projectile, a target, beam energy in eV, and directions of the beam and the target outward normal specified as angles in degrees. A target is defined layer by layer with each having the elements chemical formula, molecular density, and thickness. The output of *SimulateRBS* is a function that gives the numerical value of the backscattering spectrum given a numerical value for energy. Straggling is also included in the output of *SimulateRBS*. Instrument

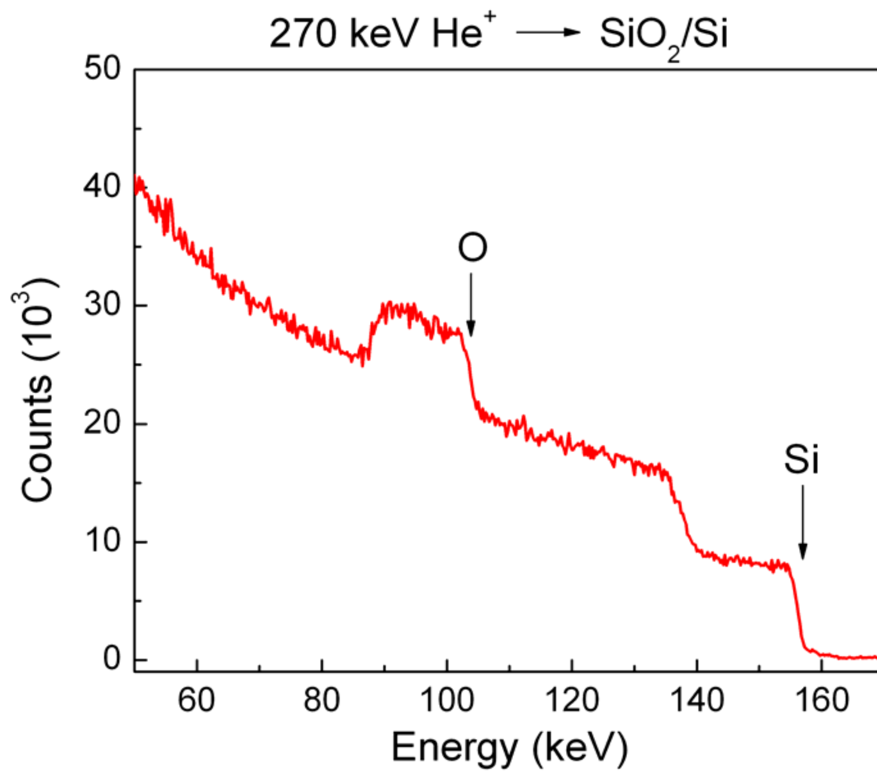

Figure 11. Energy spectrum of 270 keV He^+ incident on SiO_2/Si. Spectrum includes efficiency correction.

resolution is incorporated when the spectrum is evaluated. Simulations with *RBSTools* do not account for multiple scattering and surface roughness.

A simulated spectrum can be fit to an experimental spectrum with the function *SpectrumFit*. Any parameter that is used in the evaluation of a spectrum can be used in the fitting routine. Parameters that may be used in the fitting routine include layer thickness, density, composition, and detector resolution. The goodness of the fit is quantified by the overall χ^2, which is the sum of the square of the difference between the experimental data points and the corresponding simulated spectrum. A detailed description of simulating and fitting backscattering spectra with *RBSTools* is given in Appendix A.

Alternative Detection Systems

TOF-MEBS is just one a number of particle detection systems used for ion beam materials analysis. The most common particle detector used for this kind of work is the Si surface barrier detector (SSBD). When an energetic ion comes to rest in a semiconductor detector, it leaves in its wake a large number of electron-hole pairs. These are swept from the depletion region and appear as a pulse of current at the detector's terminal. The pulse is collected by a charge-sensitive preamplifier for further processing. The overall energy resolution of these systems is about 15-20 keV, which sets a lower limit of a few tens on nanometers on the depth resolution.[63]

In addition to time-of-flight spectrometers, electrostatic energy analyzers (ESA) have also been used in medium energy ion scattering (MEIS) work to achieve improved resolution (The acronym MEIS is typically used to describe medium energy ion

scattering work performed with an electrostatic energy analyzer). A typical electrostatic energy analyzer has an array of channel plates with a position-sensitive collector. The collector enables the determination of the angle at which the backscattered ions were detected. The detected ion energy is set by the analyzer field strength.[73] Using MEIS to analyze gate oxide films, Gustafsson and coworkers report that a depth resolution as high as 3 Å can be obtained at surface using protons with the energy at ~100 keV.[74] MEIS has been used to study dielectric films such as SiO_2,[75] Al_2O_3,[76] and ZrO_2.[77]

Although MEIS has been shown to have higher energy resolution, TOF spectrometry has been described as an attractive alternative to ESAs for several reasons. An electrostatic analyzer is sensitive to the charge state of the backscattered particle while a time-of-flight spectrometer can detect both ions and neutrals. This becomes an issue at lower beam energies because ions can capture electrons more easily to become neutrals. Also, ESAs can only examine a small range of energies at a time, while a TOF spectrometer can simultaneously measure all backscattering energies. An entire spectrum is measured by sweeping the energy over the region of interest. This makes this technique much less efficient than other detection systems.[78]

Spectroscopic Ellipsometry

Spectroscopic ellipsometry (SE) measures two quantities of polarized light, reflected from a surface, as a function of wavelength and angle of incidence. These two quantities are expressed by an amplitude component, Psi (ψ), and a phase component, Delta (Δ). Typical ellipsometers can measure ψ and Δ to better than 0.02° and 0.1° respectively, allowing resolution of thickness change down to the sub-Å scale. For thin

film analysis, SE is useful for determining thickness, surface and/or interfacial roughness, void fraction, and optical constants, such as index of refraction, extinction coefficient, and complex dielectric constant. SE is also sensitive to gradients in material properties versus film depth.[79]

In order to extract useful information from ellipsometric data, a model dependent analysis of ψ and Δ must be performed. After collecting data from the desired spectral range and angles of incidence, a model for the optical structure of the sample is constructed. The model and the Fresnel equations are then used to predict ψ and Δ, which are compared to the actual measured values. The model is fit to experimental data by iterating fit parameters such as thickness and optical constant. The difference between the experimental and predicted data is described by the (Root) Mean Squared Error (MSE), where a small value indicates a good fit.

Not all materials have intrinsic optical values; some materials' optical values depend on the process in which they were deposited. Also, the optical constant measured from a bulk specimen of material is likely to be different from a thin film of the same material.[79] Thickness measurements are also affected by overlayers or roughness on the material's surface, poor optical models, and errors in the angle of incidence.[80]

Transmission Electron Microscopy

Transmission electron microscopy (TEM) relies on the interaction between high energy electrons and the atoms in the solid. As electrons pass through a specimen, electrons are scattered by the electron cloud and nucleus of an atom. The nonuniform distribution of electrons that emerge from the sample contains structural and chemical

information about the sample.[81] Cross sectional TEM (XTEM) is used to provide a visual image of thin film's cross section with angstrom resolution. Contrast in the image shows layers of different materials and allows for visual inspection of layer thickness. The drawback to TEM analysis is that sample preparation is time consuming, making TEM analysis impractical for large numbers of samples. XTEM has been widely used to study thin dielectric films, especially for comparison to results obtained by SE, Auger electron spectroscopy (AES), and MEIS.

Atomic Force Microscopy

In atomic force microscopy (AFM), a form of scanning probe microscopy, a sharp probe is scanned across a surface while the interactions between the tip and the sample are monitored. There are three primary modes of AFM: contact mode, non-contact mode, and tapping mode. Tapping mode, which is the mode that was used for this work, operates by scanning a tip attached to the end of an oscillating cantilever across the sample surface. The tip lightly "taps" on the sample surface during scanning. The tapping mode offers high lateral resolution (1 to 5 nm) and minimizes damage done to the sample.[82]

AFM is useful for determining the roughness of surfaces. The root mean squared (RMS) roughness is the roughness value that is commonly reported for AFM measurements. The RMS roughness is the standard deviation of the height values (Z) within a given scan area:

$$RMS = \sqrt{\frac{\sum_{i=1}^{N}(Z_i - Z_{ave})^2}{N}}, \qquad \text{(II-17)}$$

where Z_{ave} is the average Z value with in the given area, Z_i is the current Z value, and N is the number of points within a given area.

CHAPTER III

CALIBRATION AND EVALUATION OF TOF-MEBS SYSTEM

All the major studies presented in this thesis were performed with Vanderbilt's time-of-flight medium energy backscattering system. This system was an appealing choice for thin film characterization because of its high resolution spectrometer and high sensitivity to light elements. However, the use of the system for thin film characterization was limited and its capabilities had not previously been fully explored. This chapter presents work performed to calibrate the system for energy, thickness, and stoichiometry measurements. Additionally, the uncertainty and reproducibility of backscattering results were evaluated.

Energy calibration

In order to obtain measurements of particle energies, the time-of-flight spectrum must be converted to the energy domain. This conversion depends on a number of parameters, which include foil thickness, particle path length, and two parameters that relate the channel n in the multichannel analyzer (MCA) to a flight time. It is assumed in TOF spectrometry that the flight time is related to a channel n by a linear relationship:

$$t = an + b \tag{III-1}$$

where *a* and *b* are constants. For routine ion beam analysis, the MCA can be assumed to be linear, such that Equation (III-1) holds.[63] The constant *a* is the conversion gain, which is the time interval of each channel. The constant *b* is the zero offset, which corresponds to the channel for a zero flight time. These parameters depend on the analysis electronics, in particularly, the analog-to-digital converter (ADC). These are adjustable parameters in the rebinning package used for converting a backscattering spectrum from the time to energy domain. An accurate conversion depends on whether or not these parameters have been properly calibrated.

The accuracy of the spectral features' energy values was determined by analyzing a thin film of $HfAl_xO_y$ on Si with 270 keV He^+. The range of atomic masses present in the film enabled a broad energy range of backscattering signals to be obtained. Backscattering spectra acquired in 2002 and again in 2004 are shown in Figure 12. The red spectrum, which was obtained in 2002, shows the O, Al, and Hf peak edges appearing at 105, 155, and 245 keV, respectively. The half max of each peak's high energy edge, which corresponds to scattering from the surface, was taken as the experimental peak location. Table 1 compares the experimental peak edge locations to their theoretical value. The energy location of the O, Al, and Hf peaks are all within 2% of their theoretical values, which suggests that the ADC was calibrated properly. Since the tops of the peaks are somewhat rounded, it is difficult to determine the true heights of the signals. Thus, the experimental peak edge locations are subject to some error, approximately ±1 keV.

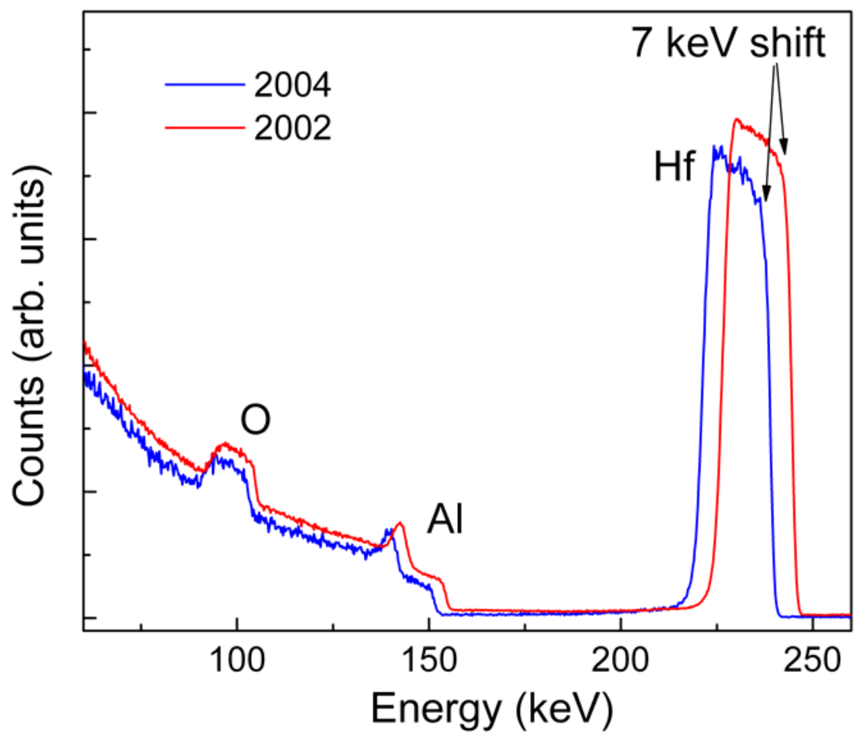

Figure 12. TOF-MEBS backscattering spectra of $HfAl_xO_y$ on Si indicating a shift in peak locations over time.

Table. 1. Comparison of theoretical and experimental peak edges for 270 keV He^+ scattering from O, Al, and Hf.

Element	Theoretical (keV)	Experimental (keV)
O	103.9	105±0.11
Al	154.5	155±0.15
Hf	248.3	245±0.25

Analysis of the peak locations was performed again in 2004 by analyzing the same thin film used in 2002 with 270 keV He^+. The spectrum is the blue spectrum shown in Figure 12. Inspection of this spectrum showed that the energy locations of the spectral features did not match those in the 2002 spectrum. The Hf signal shifted by about 7 keV, the Al signal shifted about 3 keV, and the O signal shifted by about 1 keV. Peaks at lower energies did not shift as much as the Hf peak because a change in backscattering energy is more sensitive to a shift flight time when the flight time is small. This is due to the $E \sim 1/t^2$ relationship between particle energies and flight times. This is illustrated graphically in Figure 13.

When spectral features have shifted, it is likely that the conversion gain and the zero offset have drifted. This drift could be due to aging of the electrical components in the ADC. The shift in energy scale was addressed by recalibrating the analysis electronics. The calibration was performed by calculating flight time and plotting them versus time channel. The flight time, t_f, of a particle traversing a length L in the time-of-flight spectrometer can be determined by:

$$t_f = \frac{L}{\sqrt{2(E_1 - \Delta E)/m_1}} - t_e \qquad \text{(III-2)}$$

where E_1 is the energy of a backscattered particle, ΔE is the energy the particle loses while passing through the carbon foil, m_1 is the mass of the particle, and t_e is the flight time of a secondary electron traveling from the carbon foil to the start detector. The flight length of the spectrometer, or drift length, is 112 cm. The energy loss in the carbon

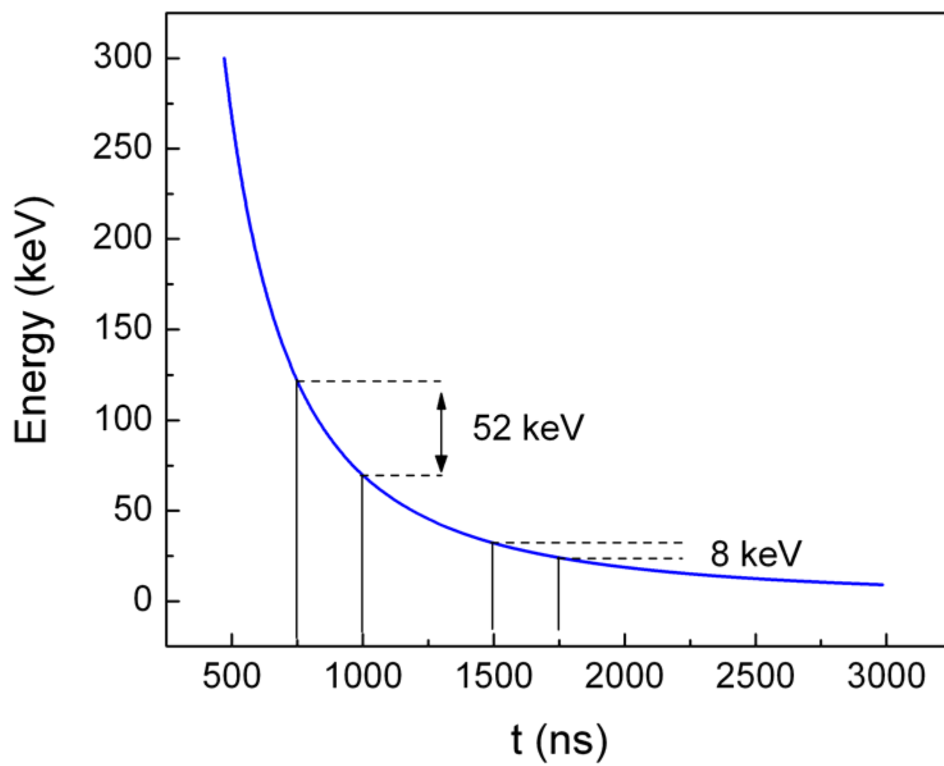

Figure 13. The corresponding energy width of some flight time interval, 500 ns for this figure, is much greater at shorter flight times.

foil is equal to the areal density of the foil, which was taken as 1.2 μg/cm^2,[83] multiplied by the stopping of helium in the foil. The stopping power of the foil was assumed to be that of pure carbon, although other contaminants such as hydrogen and oxygen are likely to be adsorbed on the carbon.[83] The flight time of secondary electrons was taken as 8.3 ns, which was determined by Mendenhall and Weller.[62]

The time channel corresponding to the flight time of a particle scattering from element *i* was taken as the low-time edge of signal *i* in the $HfAl_xO_y$ time spectrum (Figure 14). This part of the signal corresponds to scattering from the surface. The interpretation of edge location is subject to error and is a major source of uncertainty in the true values of the rebinning parameters. Additional sources of error are the uncertainty in the thickness of the carbon foil and stopping powers used for calculating energy loss through the foil. The stopping power of pure carbon was used in this calculation, but contaminants like hydrogen and oxygen are also present, although probably only a few atomic percent.[83] If the calibration is performed properly, one should not have to calibrate at every beam energy. However, it is possible to have less-than-optimal analyzer parameters and still get good results for a single beam energy.[84]

A linear least-square fit to a plot of flight time versus channel number yielded the time width of a channel and the zero offset. The zero offset is the channel that corresponds to the flight time of a particle with an infinite velocity. This analysis, in which 270 keV He ions were used, resulted in a time-channel width of 126.7 ns/channel and a zero-flight time of −56 ns. The time-channel width and zero offset channel before the recalibration were 122 ns/channel and -167 ns, respectively.

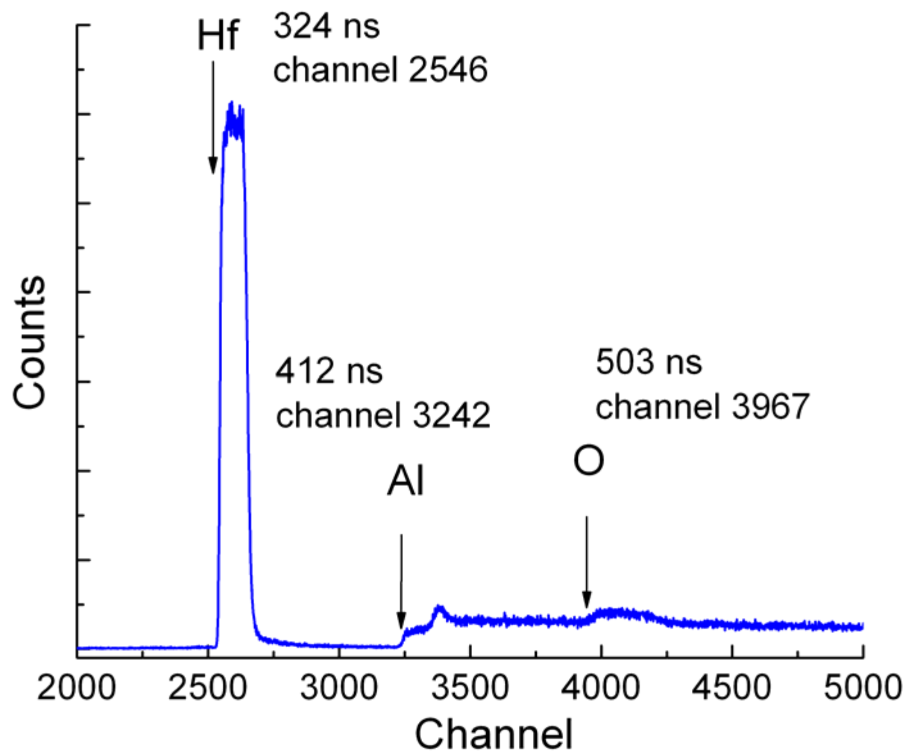

Figure 14. Time-of-flight spectrum for 270 keV He^+ incident on $HfAl_xO_y$/Si. The label of each signal indicates the flight time of a He^+ ion scattering from that element and the corresponding channel in the spectrum.

This evaluation was based on the assumption that the beam energy was known. The high-voltage power supply for the accelerator was carefully calibrated upon its commissioning. However, it is possible that the high-voltage resistors, which are responsible for generating a uniform and exact voltage, have aged with time. Suppose the beam energy did drift, what would be the error in backscattering results? For a 8 keV drift in beam energy from 270 to 262 keV (this would result in a 7 keV in a Hf signal for a 150° scattering angle), stopping powers of He^+ in ZrO_2 differ by about 1%, which corresponds to a thickness difference of about 1 Å. The stoichiometric ratio of two elements, say Zr and O, which is proportional to the ratio of the scattering cross section of the two elements (Equation II-7), differs by about a tenth of an atomic percent for the two energies. These differences are quite small, so even if the beam energy has drifted by a few keV, little difference will be seen in backscattering results.

Thickness Calibration

An initial evaluation of the TOF-MEBS system's capabilities with regard to film thickness determination was performed to establish a correspondence between thickness values obtained from TOF-MEBS and spectroscopic ellipsometry (SE). This was desirable because SE is used in our group extensively to study dielectric films both during and after deposition. Analysis with each technique was performed on SiO_2 and ZrO_2 films. Film thicknesses ranged from 35 to 300 Å.

TOF-MEBS thickness were obtained by fitting simulated spectra obtained with 270 keV He^+ with the sample normal tilted 45° relative to the beam. Ellipsometry thickness values were obtained *ex-situ* with a J.A. Woolam model M-2000D

spectroscopic ellipsometry. This device uses a QTH lamp and a D_2 lamp to generate a beam with a photon energy range of 1.2 – 6.5 eV. For SE measurements, film thicknesses were obtained by fitting a parametric model to experimental data using the software supplied with the SE system, WVASE 32. A simplified model consisting of ZrO_2 on Si was used for this study where the ZrO_2 layer was represented by the Cauchy dispersion model. The Cauchy model is typically used for dielectrics and semiconductors where the index of refraction and extinction coefficient are represented by a slowly varying function of wavelength.[130]

A set of ZrO_2/Si structures with ZrO_2 thicknesses ranging from 35 to 240 Å were analyzed with both TOF-MEBS and SE. A comparison of the thickness results is shown in Figure 15. The points in Figure 15 show TOF-MEBS thicknesses versus SE thicknesses. The solid red line in the figure shows a linear fit to the data, which has a slope of 1.02. The y-intercept of the line indicates that TOF-MEBS thickness results are about 34 Å lower than SE values. A slope of 1.0 and y-intercept of 0.0 would indicate a direct correspondence between the thickness values determined by the two techniques, as indicated by the blue line. One explanation for the difference between the two techniques is the bulk ZrO_2 density value (5.7 g/cm^3) used in TOF-MEBS spectra simulations. Bulk densities tend to be higher than thin films of the same material. Additional factors contributing to the offset are stopping values used in the simulations and the optical properties of ZrO_2 that were used for SE analysis, both of which are based on approximations. Due to the uncertainty in ZrO_2 film densities and optical properties, the correspondence between TOF-MEBS and SE thickness values was also determined using thermal SiO_2. More reliable thickness values can be obtained from thermal SiO_2 because

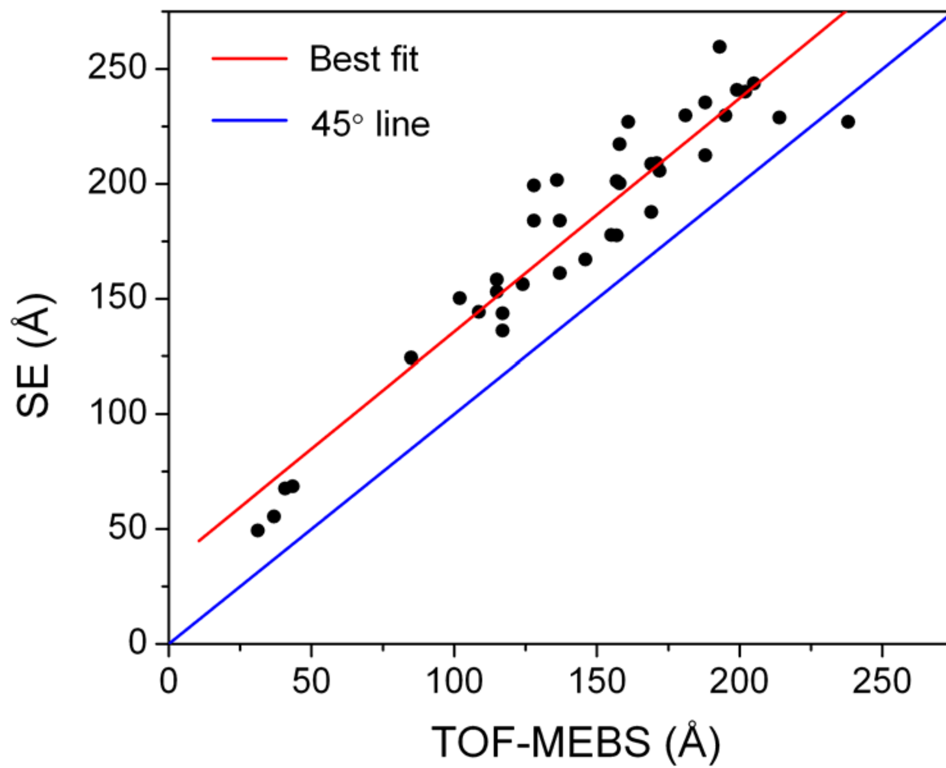

Figure 15. Comparison of SE and TOF-MEBS thicknesses from ZrO_2 samples. The red line shows the best fit with a slope of 1.09 and a y-intercept of 34.1.

the density of the material is well known and the optical properties have been experimentally determined. Figure 16 compares SiO_2 film thicknesses determined by the two techniques. The solid line shows that best linear fit to the data where the slope is 0.91 and y-intercept of 7.6. In addition to stopping power values, the reason for the slight difference between TOF-MEBS and SE thickness values for the thermal oxide samples could be the presence of an interfacial transition layer present between the SiO_2 and Si.[85] This layer is known to be a Si-suboxide and has slightly different stopping powers than SiO_2.

TOF-MEBS thickness results have also been compared to those obtained from TEM analysis. Table 2 compares thicknesses of thin ZrO_2 films deposited on Si. Figure 17 shows a TEM image of ZrO_2 (59.7 Å)/$ZrSi_xO_y$ (11.1 Å)/Si. TOF-MEBS thickness results for the same sample are ZrO_2 (51.5 Å)/$ZrSi_xO_y$ (17.7 Å). The density values used for obtaining thicknesses from TOF-MEBS results were $\rho_{ZrO2} = 5.7$ g/cm^3 and $\rho_{ZrSixOy} =$ 3.5 g/cm^3. Again, the difference in thickness results between the two techniques can be attributed to the assumed densities and the stopping powers of the materials. An additional explanation is the location of the interface between each layer, which is subject to interpretation for TEM analysis.

Stoichiometry Calibration

To test the accuracy of stoichiometry values determined by TOF-MEBS analysis, backscattering spectra were obtained from thermal SiO_2 samples. The choice of the samples was based on the idea that the bulk composition of thermally grown SiO_2 films is stoichiometric. However, for films on the order of a few monolayers the O:Si ratio

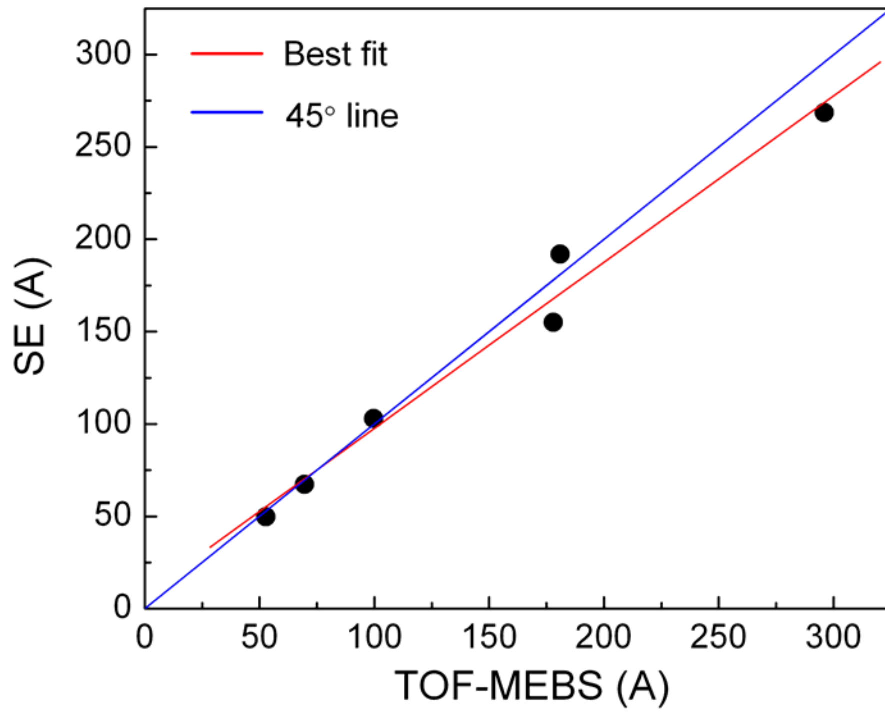

Figure 16. Comparison of SE and TOF-MEBS thicknesses from SiO_2 samples. The red line shows the best fit with a slope of 0.91 and a y-intercept of 7.6.

Table 2. Thickness comparisons of ZrO_2 films and interfacial layer determined by TOF-MEBS and TEM.

	ZrO_2		Interfacial layer	
	TOF-MEBS (Å)	TEM (Å)	TOF-MEBS (Å)	TEM (Å)
1	14.4	32.0	15.5	13.9
2	23.2	36.0	15.7	12.5
3	22.7	36.1	16.6	11.1
4	24.3	35.0	17.0	14.2
5	51.5	59.7	17.7	11.1

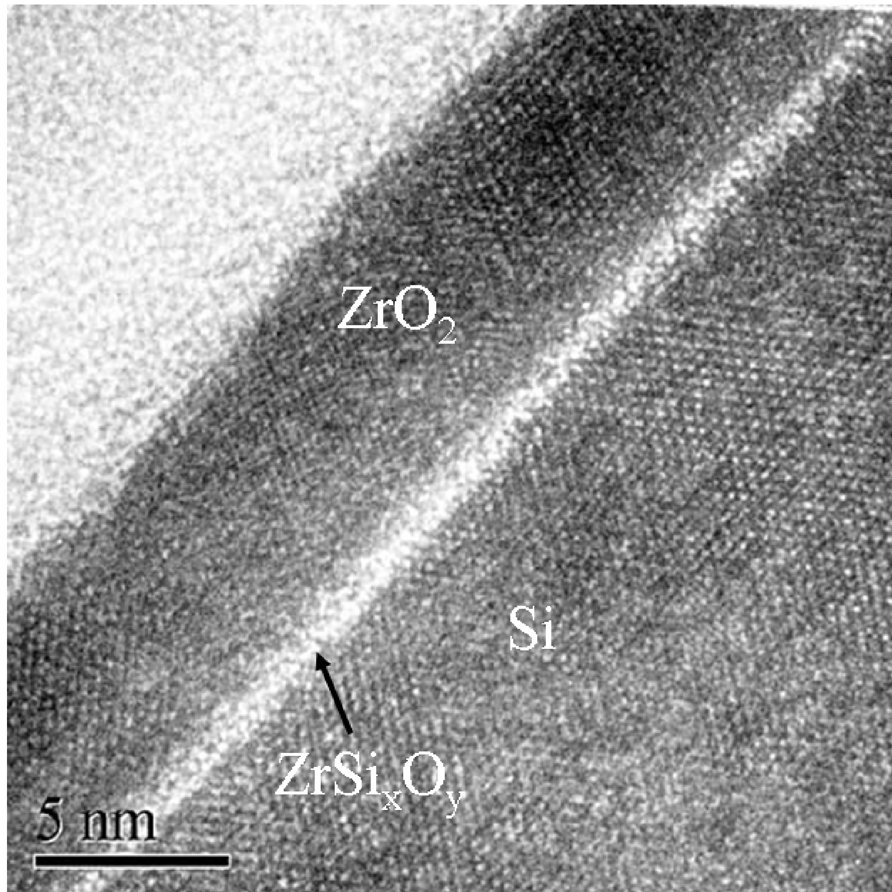

Figure 17. Cross sectional TEM image of ZrO_2 (59.7 Å)/$ZrSi_xO_y$ (11.1 Å)/Si .

departs from 2:1 due to the increasing contribution of the interfacial suboxide layer that forms between the oxide and the silicon substrate.[85] The SiO_2 films used for this study ranged in thickness from 50 to ~1000 Å. A bulk SiO_2 density of 2.22 g/cm^3 was used in data analyses. Backscattering spectra were simulated in *RBSTools* and best fits to experimental spectra obtained using atomic ratio as a fit parameter. Backscattering results gave O:Si ratios that were about 5% lower than the theoretical value of 2 (Figure 18). The 95% confidence levels shown by the error bars where obtained from the standard deviation calculated during spectrum simulation fits.

Backscattering Statistics

The data obtained during the course of ion beam analysis have intrinsic variability. This variability is reflected in the uncertainty in the final results of the analysis. In backscattering analysis, one source of uncertainty is the random error associated with counting backscattering events. These rare events occur with constant probability per unit time, and as a result, obey Poisson statistics. Accordingly, the probability $P(n)$ of observing exactly n events in a time interval is given by the Poission distribution:

$$P(n) = \frac{m^n e^{-m}}{n!}, \tag{III-3}$$

where m is the mean number of counts expected in the time interval. If m is large, then $P(n)$ assumes an approximate form such that the probability of obtaining exactly n counts is normally distributed with variance $\sigma^2 = m$. This result provides the rule for assigning

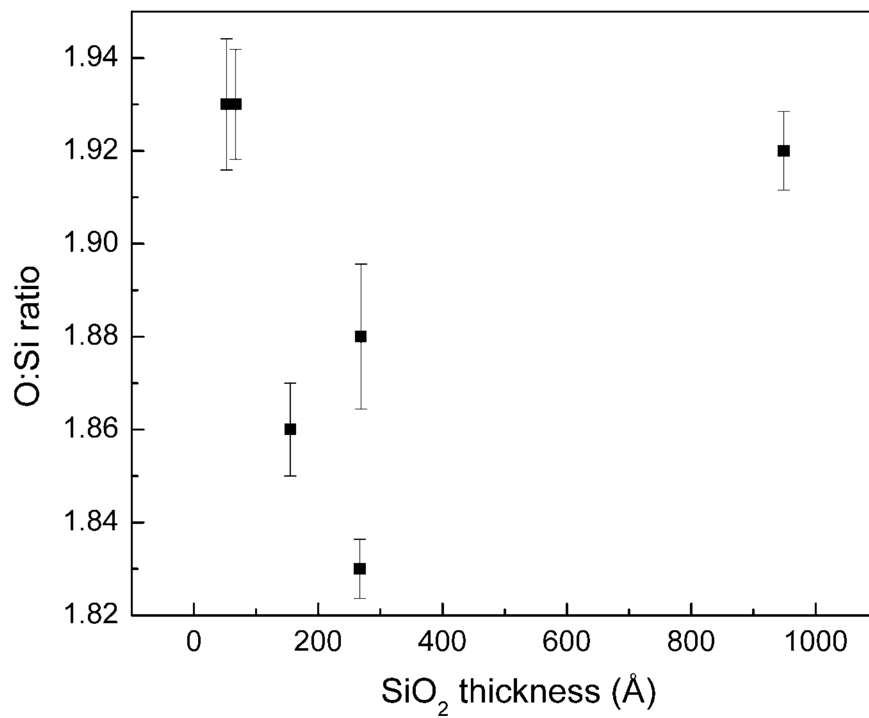

Figure 18. Stoichiometric ratio versus SiO_2 film thickness. Thicknesses are from TOF-MEBS results.

the statistical error to a measurement. Thus, for a large number of scattering events N, the standard deviation in the number of counts measured is $\sqrt{N}$ and the percent uncertainty is

$$\% \text{ uncertainty} = \sqrt{N} / N \times 100\% . \qquad \text{(III-3)}$$

It follows that for a two-fold improvement in statistics, four times as many counts must be collected.[63]

In ion beam analysis experiments such as TOF-MEBS, the total number of incident particles is measured by the total charge collected in coulombs (C). 1 μC of charge collected corresponds to 6.24×10^{23} incident particles. In this work, five TOF-MEBS spectra were collected from a 60 Å ZrO_2 sample for a total integrated charge of 20, 40, 80, and 160 μC. The same operating conditions were used for each run: 270 keV He^+, target tilt 0°, beam current ~50 nA. It was assumed that factors such as sputtering did not change the nature of the sample throughout the course of the experiment.

The statistics of TOF-MEBS spectrum were evaluated by determining the total number of counts in particular regions of interest. It is important that this evaluation is performed with a spectrum in the *time* domain because the conversion of spectra to the energy domain and the efficiency correction alter the counting statistics. The total number of counts contributing to the O and Zr signals were determined and the % uncertainty calculated by using Equation (III-3). Figure 19 shows the % uncertainty as a function of total collected charge for the O and Zr signals. A linear background subtraction was performed on the O signal to remove contributions from the Si substrate

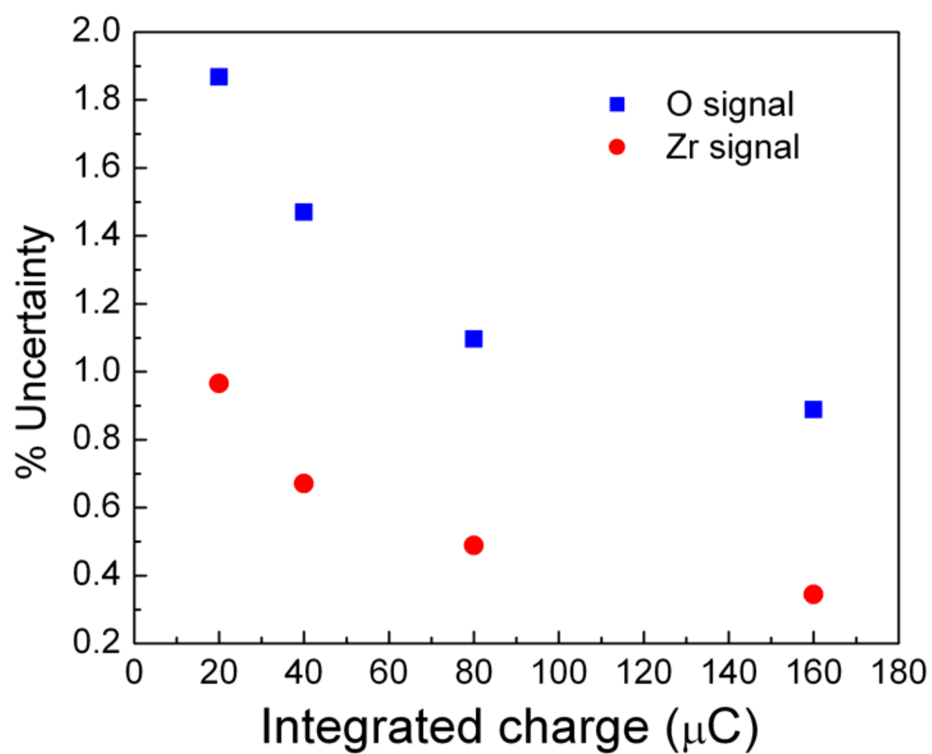

Figure 19. Percent uncertainty versus integrated charge for O and Zr signals in time-of-flight spectrum.

signal. The amount of charge collected for a typical TOF-MEBS experiment is around 80 μC. This corresponds to an uncertainty of 1.1% and 0.5% for the O and Zr signals, respectively. The uncertainty is higher for the O signal because fewer He^+ ions scatter from O due to its smaller scattering cross section. Nonetheless, this precision is as good as or better than most other sources of error in a typical ion beam experiment.[63]

The uncertainty in the number of counts in a backscattering spectrum is reflected in the reproducibility of backscattering results. The reproducibility of results obtained by fitting simulations to experimental spectra was determined by calculating the standard deviation of the best fit parameters. By performing separate backscattering experiments on the same sample, an estimation of the overall experimental error (random + systematic) can be obtained. The standard deviation for layer thicknesses (Figure 20) and film composition (Figure 21) versus integrated charge are plotted in the figures below. The fit results for the atomic % of Zr in the ZrO_2 layer was found to have a standard deviation of about 0.6 atomic % (80 and 160 μC). This corresponds to a relative error ($\sigma / \bar{x} \cdot 100\%$) of about 3 %. The standard deviation of the Zr atomic % in the silicate layer is about 0.5 atomic % for the three longer integrated charges. However, the average atomic % of Zr in this layer is only about 4.5 %, so the relative error is 11% (80 μC), which is not as good as the absolute error might suggest. The error in the atomic % of O in the silicate layer is relatively large because there are so few counts in the back edge of the O signal.

It takes about 60 min to collect an integrated charge of 80 μC (beam current ~ 50 nA), which is around the typical integrated charge of most backscattering spectra

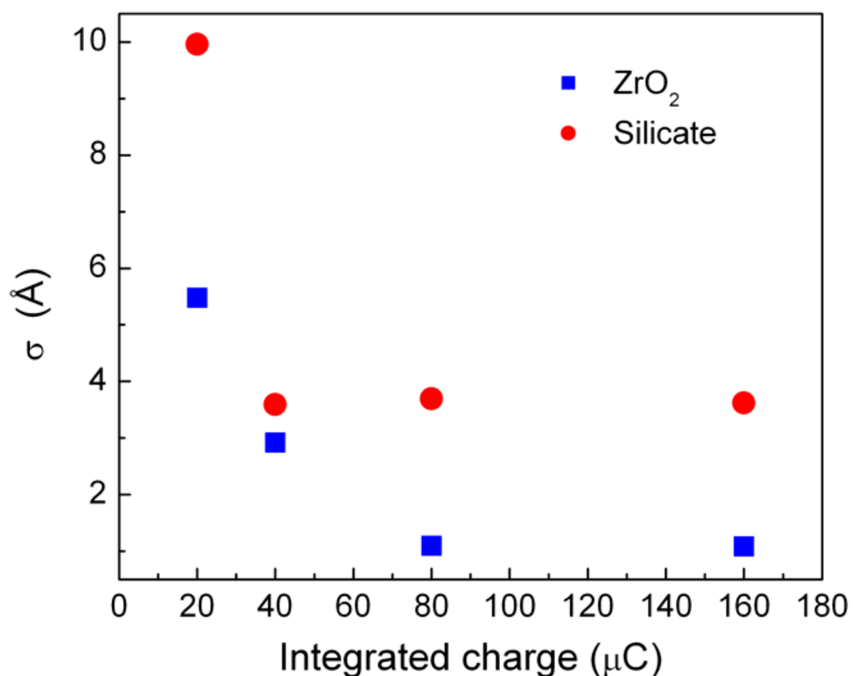

Figure 20. Standard deviation of ZrO_2 and Zr-silicate layer thickness versus integrated charge.

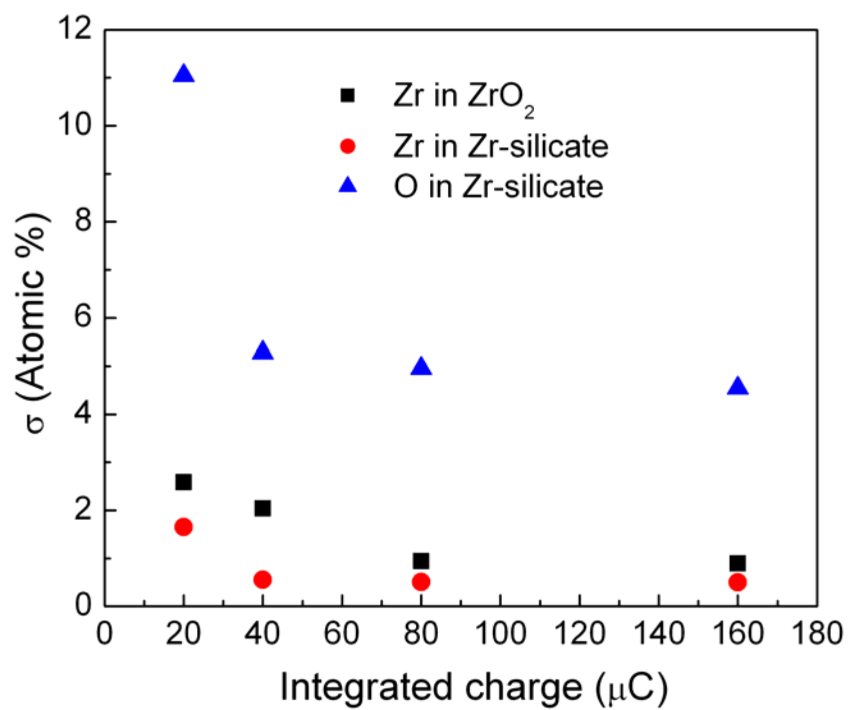

Figure 21. Standard deviation of Zr and O atomic percent versus integrated charge.

collected in this work. Since there is almost no difference between the standard deviations calculated for the integrated charges 80 and 160 μC, there is little incentive to spend an additional hour to accumulate more counts for improved statistics.

Conclusions

TOF-MEBS provides accurate thickness values with just a few percent of error when density and stopping power are well known and when the film composition is uniform. Film composition determined by simulating a TOF-MEBS spectrum is accurate within a few atomic %, but the uncertainty will be higher for thinner films because fewer backscattering counts define the layer. For TOF-MEBS analysis of 60 Å ZrO_2 on Si, the composition of the ZrO_2 layer has an uncertainty of about 3 %, while the relative error in the composition of the interfacial silicate layer is about 11%.

CHAPTER IV

INTERFACIAL ANALYSIS USING TOF-MEBS

As gate dielectric thicknesses in complementary metal oxide semiconductor devices (CMOS) are scaled to smaller dimensions, a fundamental understanding of the dielectric/Si interface becomes critical. Furthermore, when the dielectric thickness is on the order of 1 nm, material interfaces can dominate chemical and electrical properties of the gate stack. [42] CMOS scaling has also put pressure on the characterization techniques necessary to determine the physical and chemical properties of this interfacial region.[41] TOF-MEBS is presented in this work as a novel analytical technique for characterizing thin dielectric materials and their interfaces with Si. This chapter compares TOF-MEBS to conventional Rutherford backscattering spectrometry and discusses the efforts made to identify and optimize the amount of information that can be extracted from the TOF-MEBS spectra of ultra-thin dielectric films on silicon.

Rutherford backscattering spectrometry (RBS) has been used extensively for studying thin films. Conventional RBS uses light MeV ions and a Si surface barrier detector (SSBD). A SSBD has an energy resolution around 15 keV, which translates to a depth resolution on the order of a 100 Å. Although improved depth resolution in RBS can be obtained by using grazing incidence and exit angles,[86, 87] surface roughness becomes a problem by producing large variations in the cumulative energy loss of ions on different trajectories.[47] Due to poor depth resolution, RBS offers limited information for thickness scales less than a few hundred angstroms.

By combining time-of-flight spectrometry with medium energy ion scattering, Mendenhall and Weller were able to achieve increased depth resolution and improved surface sensitivity compared to conventional RBS.[62, 78, 88] Weller and coworkers optimized the TOF spectrometer design in which the contributions to measurement uncertainty from variation in path length and kinematic dispersion were reduced. They measured a depth resolution of about 2 nm. Due to larger cross sections at lower energies, TOF-MEBS is about 50 times more sensitive than conventional RBS with 2 MeV He^+. Although stopping powers are smaller at lower energies, the loss of intrinsic depth differentiation is more than made up by the gain in the spectrometer resolution of the time-of-flight detector.[47]

Prior to my work with the TOF-MEBS system, only a few studies had been performed with the system for thin film analysis. Weller and coworkers used the system to analyze a silicon-oxide, silicon-nitride multilayer target.[89] Although the study presented in this chapter concerns the analysis of dielectric materials, TOF-MEBS analysis can also be applied to softer materials like organic thin films. Arp and coworkers analyzed cadmium arachidate Langmuir-Blodgett thin films with the TOF-MEBS system.[90] By using 270 keV He^+, there were able to obtain thickness and stoichiometry values consistent with unmodified films. Another study of organic thin films using the TOF-MEBS system was performed by Huang and coworkers. They studied the suppression of aluminum penetration into 8-hydroxyquinoline aluminum organic thin films.[91]

Experimental Details

Dielectric materials systems studied in this work included Al_2O_3, SiO_2, and ZrO_2 on silicon. Film thicknesses ranged from approximately 10 to 200 Å. TOF-MEBS experiments were performed with 270 keV He^+ and a beam current of ~ 50 nA The total charge collected for each spectrum was 100 μC. Data analyses were performed by modeling the ion interactions with material structures and performing a non-linear least squares fit to the backscattering spectra. The beam spot size was about 18 mm^2. The effective solid angle for detection is 0.5 msr. The configuration of the time-of-flight spectrometer was previously shown in Figure 9.

Data Analysis

TOF-MEBS spectra were simulated with a suite of computational tools, *RBSTools*, implemented in *Mathematica* and developed by Weller for general-purpose ion-solid calculations.[67] These tools are suitable for both medium energy work and higher energies of conventional RBS. Stopping powers are identical to those tabulated by Rauhala.[92]

Since TOF-MEBS produces spectra of particle yield versus flight time, the data must be mathematically rebinned from the time domain to the energy domain and corrected for spectrometer efficiency. This procedure is also performed within a *Mathematica* program. A model of the intrinsic efficiency of the spectrometer was developed by Weller and coworkers and is included in the spectrum simulation calculations.[65] This model takes into account the effects of secondary electron emission,

multiple scattering in the start foil, and the energy dependent efficiency of the stop detector.

Model fits to experimental data were performed using Marquardt's method[93] with numerical differentiation to perform nonlinear, least-squares fits. The quality of the overall fit is given by χ^2. In order to identify regions of poor fit to experimental data, the distribution of residual χ^2 values was generated and examined.

Parameters used in the spectrum fitting routine include background, thickness (or film density), stoichiometry, and substrate channeling ratio. The substrate channeling ratio, channeling χ_{min}, is not related to the statistical value χ^2. Channeling χ_{min} is defined as the ratio of counts in the channeled spectrum to the number in the random spectrum at the same energy. Channeling χ_{min} values as low as 5% have been achieved.

Results and Discussion

The benefit of the improved resolution of the TOF-MEBS system compared to conventional RBS is illustrated in Figure 22. Figure 22(a) is a computer simulation of He^+ backscattering at 1.8 MeV using a surface barrier detector. The target is a 100 Å SiO_2 film on silicon oriented 45° to the beam. Backscattering analysis using 1.8 MeV He^+ ions and a surface barrier detector is typical for conventional RBS experiments. Figure 22(b) shows computer simulations of 270 keV He^+ backscattering from the same target using a surface barrier detector (—) and a time-of-flight spectrometer (—). Figure 22(b) shows that the combination of a high-resolution spectrometer and medium energy ions gives TOF-MEBS the ability to discern significantly more depth information from this sample than RBS. The TOF-MEBS spectrum (Figure 22(b), (—)) clearly shows the step on the

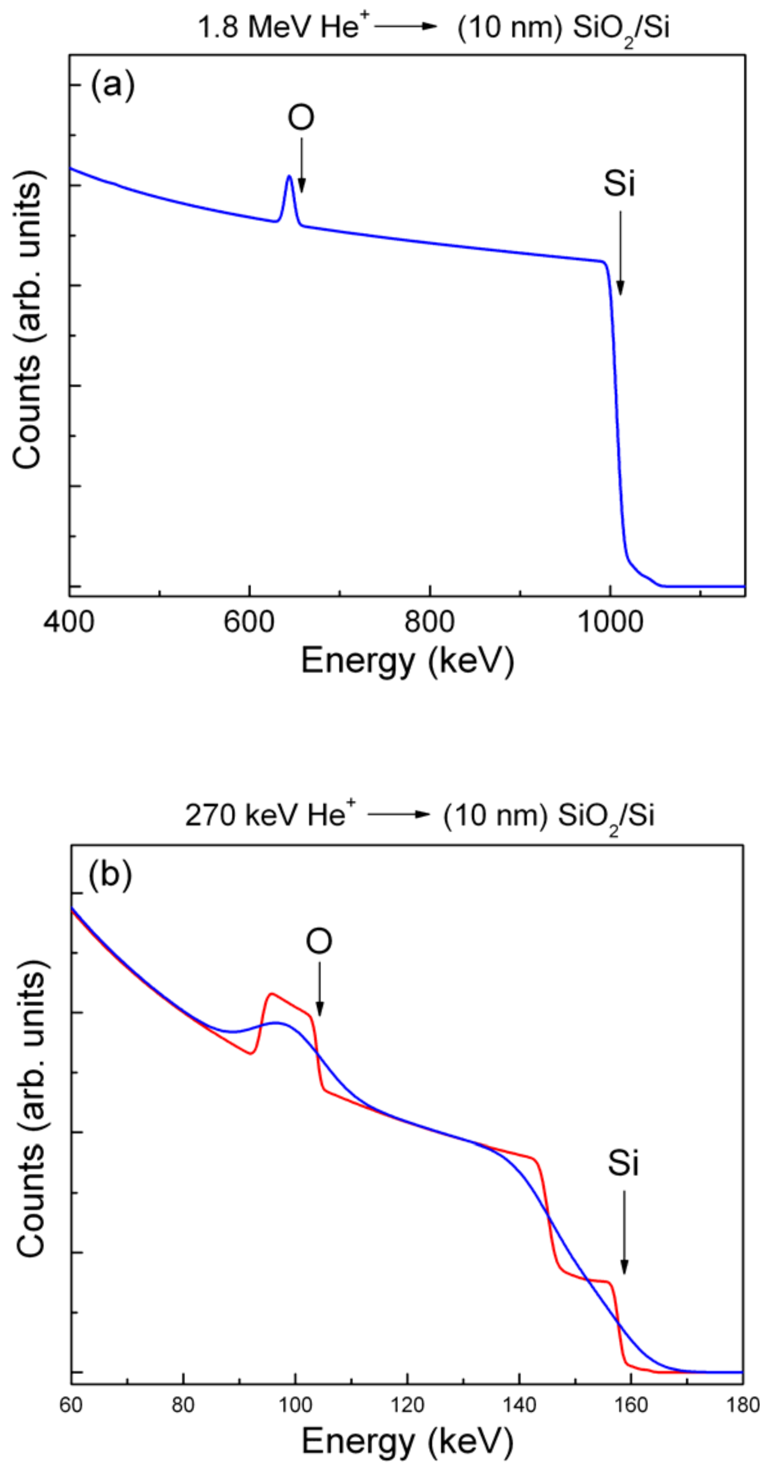

Figure 22. Computer simulations comparing He^+ backscattering at 1.8 MeV (a) and 270 keV (b) using a surface barrier detector (—) and a time-of-flight spectrometer (—). The target is a 100 Å SiO_2 film on silicon oriented 45° to the beam.

edge of the silicon due to the SiO_2 layer and a wide oxygen peak, whereas in the RBS spectrum the step on the silicon edge is not detected and the oxygen peak is little more than a delta function. A broad signal is desired over a sharp narrow one since the shape of a signal in a backscattering spectrum essentially provides a depth profile for the corresponding element. Although Figure 22 shows simulated spectra, the same improvement in depth information can be expected for actual backscattering experiments where the same analysis conditions are used.

TOF-MEBS also offers improved surface sensitivity over conventional RBS due to larger scattering cross-sections at lower energies. Figure 23 contains a backscattering spectrum acquired from a 18 Å native silicon oxide layer on Si(100) and its corresponding simulation. The composition of the native oxide layer is $SiO_{0.95}$ with about 2.2×10^{15} C atoms/cm^2 of contamination on the surface. The target was oriented 45° to the beam, and the detector was fixed at 150° to the beam. At 45° the beam channeled in the ❬110❭ direction and reduce backscattering contributions from the Si(100) substrate (χ_{min} = 8%). Conventional RBS analysis would be unable to detect this low-level of carbon contamination and ultra-thin SiO_x layer.

Figure 24 contains backscattering spectra of Al_2O_3 deposited on Si(100). Both carbon and silicon appear on the surface, probably due to hydrocarbon adsorption and porosity in the alumina film, respectively. The areal density of the carbon on this sample was determined to be 1.64×10^{14} atoms/cm^2. The average concentration of Si on the surface was determined to be 1.85×10^{13} atoms/cm^2. Figure 24(a) shows a best fit to the experimental data using a C/Al_2O_3/Si model. The residual χ^2 distribution shown at the bottom of the figure reveals that the region of poorest fit (high χ^2 values) is at the

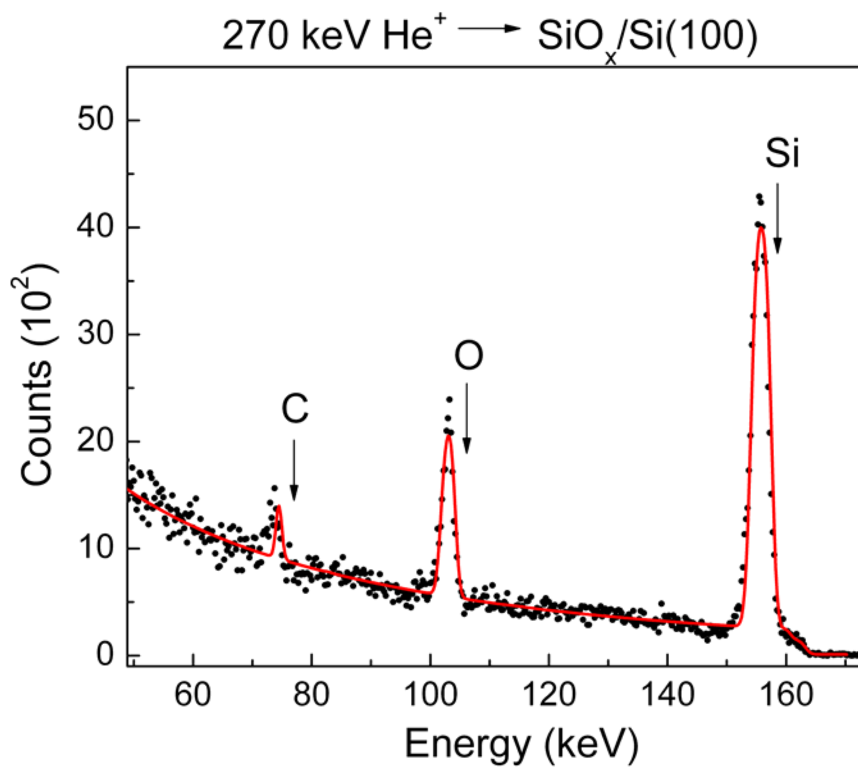

Figure 23. Backscattering spectrum (· · ·) and simulation (—) for 270 keV He^+ ions incident on 2.2×10^{15} C atoms/cm^2 on 18 Å SiO_x on Si(100). Sample was tilted 45° to the beam for channeling in the ‹110› direction. χ_{min} was 8%.

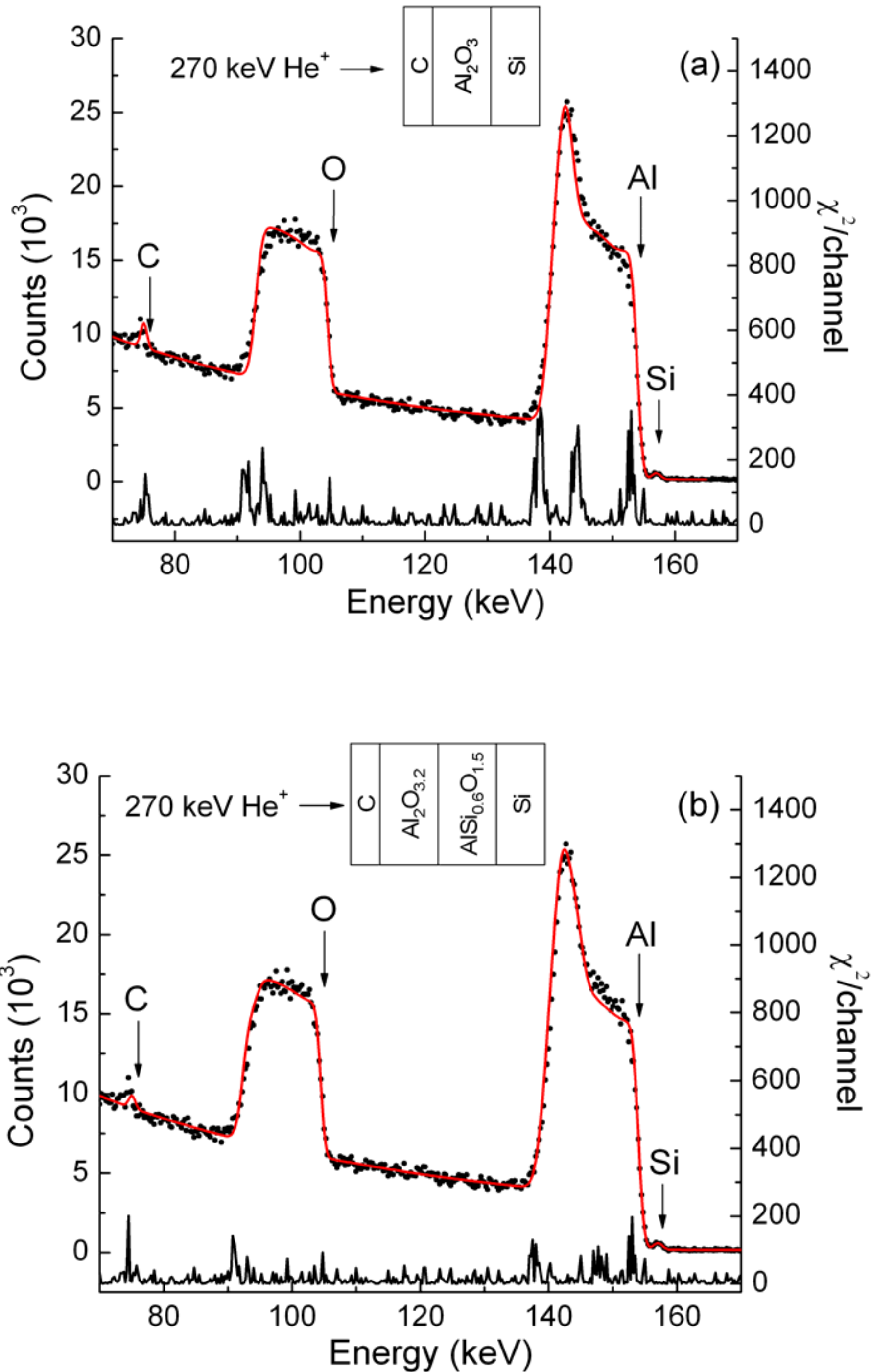

Figure 24. Backscattering spectrum (· · ·) and simulation (—) from aluminum oxide film on Si(100). Data were acquired using 270 keV He^+ ions with the sample tilted 45° to the beam for channeling in the ‹110› direction. χ_{min} was 15%. (a) Backscattering data and simulation using the $C/Al_2O_3/Si$ model. (b) Backscattering data and simulation using $C/Al_2O_x/AlSi_xO_z/Si$ model. The curve at the bottom of each figure shows the residual χ^2 distribution (—) for the respective simulation's fit.

alumina-silicon interface. It has been shown in literature that silicate and silicon dioxide layers can form at alumina-silicon interfaces.[11, 37, 94] Therefore, an interfacial layer was included in the material model and the simulation repeated. The overall χ^2 value was reduced by 43% by inserting an aluminum silicate layer at the alumina-silicon interface. The bottom curve of Figure 24(b) shows the residual χ^2 distribution after this interfacial layer in the model. The improved model reduced χ^2 values at the lower energy edges of the oxygen and aluminum signals and the front edge of the silicon signal. However, the fit in these regions is still relatively high compared to the rest of the χ^2 distribution. This could be due to layer roughness or interdiffusion between the respective layers.

Simulations determined the final structure to be $C/Al_{2.0}O_{3.2}$(72 Å)/$AlSi_{0.6}O_{1.5}$(40 Å)/Si with a total thickness of 112 Å. The thickness of the stack is based on an aluminum oxide bulk density[95] of 3.0 g/cm^3 and an aluminum silicate density of 2.6 g/cm^3. The silicate density of 2.6 g/cm^3 was chosen simply as a value between the density of pure SiO_2, 2.22 g/cm^3, and pure Al_2O_3, 3.0 g/cm^3. In all backscattering analyses, either a thickness or density value must be known *a priori* for an accurate determination of the other.

Figure 25 contains a backscattering spectrum and simulation of metal-organic chemical-vapor deposition (MOCVD) deposited zirconium oxide on Si(100). A simulation using a target model of ZrO_2 on Si yielded a poor fit. Regions of poorest fit, as shown by the residual χ^2distribution given in Figure 25(a), are the lower energy edges of the Zr and O signals and the leading edge of the Si signal. Fits to backscattering spectra were also poor at energies beyond the front edge of the Zr peak. This is due to the

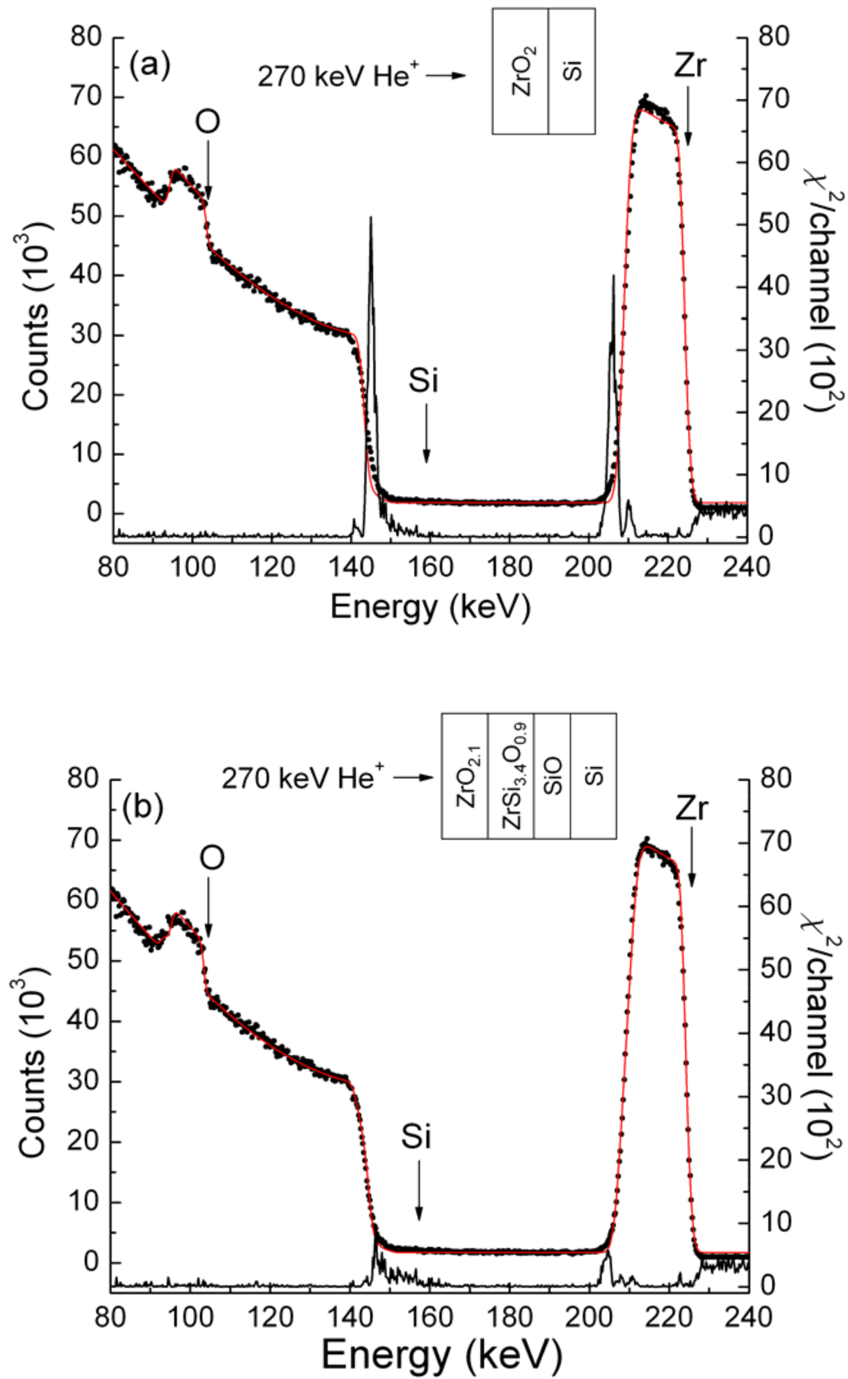

Figure 25. Backscattering spectrum (· · ·) and simulation (—) from zirconium oxide film on Si(100) Data were acquired using 270 keV He^+ ions with the sample tilted 45° to the beam. (a) Backscattering data and simulation using a ZrO_2/Si model. (b) Backscattering data and simulation using $ZrO_x/ZrSi_yO_z$/SiO/Si model. The curve at the bottom of each figure shows the residual χ^2 distribution (—) for the respective simulation's fit.

background model used in the simulation, which is a constant value for the entire spectrum

The residual χ^2distribution suggests that a material other than zirconium oxide is present at the interface. Both silicates and SiO_2 have been shown to form between as-deposited films of zirconium oxide and silicon,[14, 18, 96] which is discussed in detail in Chapter VII. Inserting a zirconium silicate and a suboxide layer at the interface of the zirconium oxide and the silicon substrate improved the overall χ^2 by 60%. The residual χ^2 distribution at the bottom of Figure 25(b) shows that the fit improved the most at the interfacial regions. Simulation determined the final composition to be $ZrO_{2.1}$(148 Å)/ $ZrSi_{3.4}O_{0.9}$(28 Å)/SiO(10 Å)/Si(100), with a total nominal thickness of 186 Å. The density value used for zirconium oxide was 5.7 g/cm^3, which has been previously reported.[94] A density value of 4.6 g/cm^3 was used for the zirconium silicate layer. This is the theoretical density value for $ZrSiO_4$. The total nominal thickness of the film determined by spectroscopic ellipsometry (SE) was 201 Å, 8% higher than the thickness determined by TOF-MEBS. This difference is likely due to the density values used in the simulation. Density values for ZrO_2 as low as 4.0 g/cm^3 have been reported in literature.[97] The difference between TOF-MEBS and SE thickness results could be reduced by using a lower ZrO_2 density value ($<$5.7 g/cm^3) in the simulations.

Possible explanations for the poor fit at the lower energy edge of the Zr signal are contributions from multiple scattering and surface roughness. These factors are addressed in Chapter V, in which both factors were found to be negligible for the analysis of 50 Å ZrO_2 on Si. However, the ZrO_2 film in this study is more than three times as thick. Since multiple scattering increases with path length, this effect might have

influenced the shape of the lower energy edge of the Zr signal in the ZrO_2/Si spectrum shown here.

In Figure 25(a) and (b), the regions beyond the front edge of the Zr signal indicate poor fit. The overall χ^2 of the ZrO_2/Si simulations can be improved further by adjusting the background model. The background used in the simulations shown above is simply a constant value. The background at energies above the Zr signal is not affected by multiple scattering and surface roughness and contains contributions due mainly to random coincidences. Random coincidences occur when stop and start signals are initiated by different particles.[78]

The discrepancy between the background above and below the Zr signal was addressed by superimposing the linear background with an error function:

$$background = H_1 - H_2 Erf\left(\frac{E - E_1}{\sqrt{2}\sigma}\right), \tag{IV-1}$$

where H_1 and H_2 are the background heights before and after the Zr signal, respectively; E_1 corresponds to the energy location of the error function and σ is the width of the function expressed as a standard deviation. H_1, H_2, E_1, and σ can be included as fit parameters in the fitting routine. By using an error function instead of a linear or step function, the change in background height is smooth. The background function and a simulated Zr signal are plotted in Figure 26. The overall χ^2 for the fit shown in Figure 25(b) is reduced from 48,000 to 20,000. Without a background adjustment, the high energy region of the spectrum can influence how well the simulation fits at other regions of the spectrum. Figure 27, which plots the residual χ^2 distribution before and after the

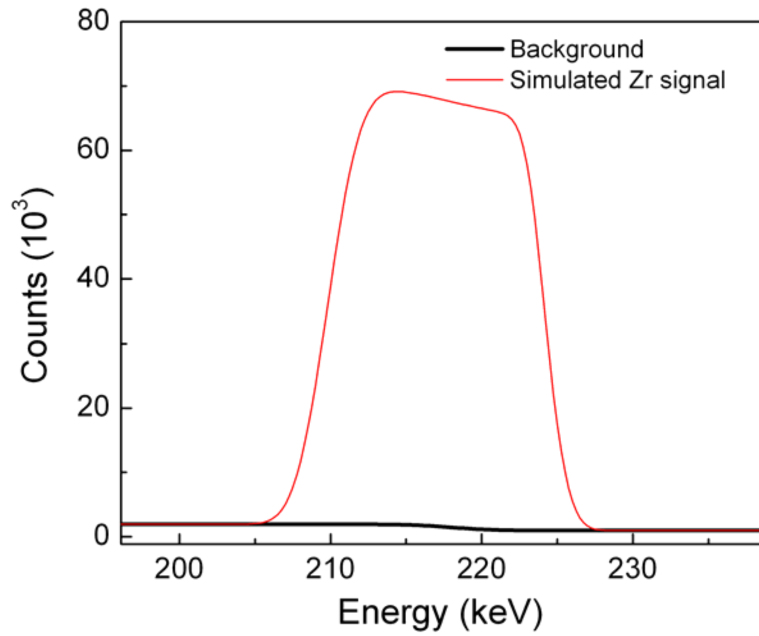

Figure 26. Background function and simulated Zr signal.

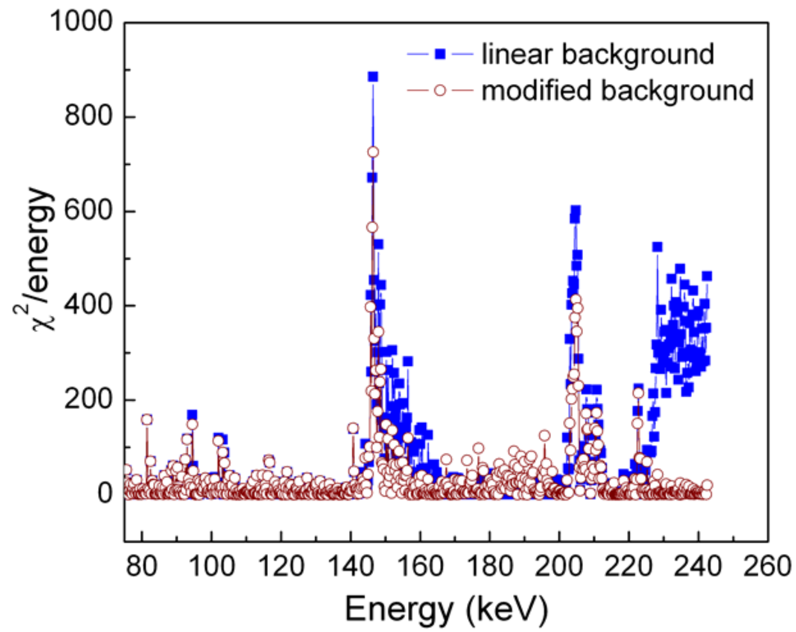

Figure 27. Residual χ^2 distribution for simulated 270 keV He^+ ZrO_2/Si backscattering spectra with and without background modification.

background modification, shows the modification also improves the fit near the front edge of the Si signal. The background modification changes best fit thickness results by less than 1%. However, the interfacial layers composition is altered to a larger degree, up to 10 %.

Conclusions

The materials properties of three different dielectric/Si materials systems were characterized with TOF-MEBS. As in all backscattering analyses, the thickness determined from the simulations depends of the materials density values used in the models. Simulation fit results were significantly improved by including thin interfacial layers between the dielectric films and silicon in the material structure models and by modifying the shape of the background. Although two interfacial layers were used in the thin film model for simulating ZrO_2/Si spectra, this model is not necessarily the most appropriate for all cases. For film structure having a very thin interfacial layer (~ 10 Å), a single interfacial layer might suffice, as in the case for the Al_2O_3/Si materials structures analyzed in this work.

CHAPTER V

EFFECTS OF MULTIPLE SCATTERING AND SURFACE ROUGHNESS ON BACKSCATTERING SPECTRA

In this work quantitative information is obtained from backscattering spectra with the package *RBSTools*,[67] in which simulated spectra are fit to experimental results. Backscattering spectra simulations in *RBSTools* are based on the assumptions that projectile trajectories experience single, large angle scattering (single scattering approximation) and that target surfaces are atomically smooth. However, in reality, projectiles undergo multiple small and large angle scattering events and surfaces contain topographical features. Both of these factors can significantly alter the shape of a backscattering spectrum and result in a misinterpretation of features present in the spectrum.

The purpose of this study is to evaluate the effects of multiple scattering and surface roughness on backscattering spectra obtained with the TOF-MEBS system. In this study Monte Carlo (MC) simulations were performed for two different targets (Ta/Si and ZrO_2/Si) at two different detector geometries. The Ta/Si target was chosen to illustrate an extreme case where multiple scattering has significantly affected the shape of the backscattering spectrum. The second target was modeled after that which we have analyzed in the lab with TOF-MEBS. Experimental TOF-MEBS spectra of this materials system indicate a slight tail at the low energy edge of the Zr signal. This tail has been interpreted as Zr in an interfacial silicate layer. However, it is unclear if multiple

scattering and surface roughness are responsible for this feature or if a silicate layer is in fact present.

Multiple Scattering

The single scattering model approximates ingoing and outgoing particle trajectories by straight lines and accounts for a single large angle scattering event. Actual particle trajectories are determined by a large number of collisions with target atoms, resulting in multiple small and large angle deflections.[98] Due to multiple kinematic energy losses and increased path lengths, multiple scattering may result in projectile energies that are much lower than expected for scattering at a some depth.[99]

In literature, the term plural scattering is used to refer to large angle scattering, while multiple scattering refers to small angle deflections. However, since a particle trajectory may experience both types of scattering, the distinction is artificial.[98] In this work multiple scattering will be used to refer to both types of scattering events.

An early treatment of the effects of multiple scattering on the shape of backscattering spectra was given by Weber and coworkers.[100] They collected backscattering spectra of a ~320 nm Au foil on Si using protons ranging in energy from 150-400 keV. This study proved that multiple scattering can contribute to the low energy background in their spectra. The study found that the background due to multiple scattering increases significantly with decreasing energy, increasing target thickness, and increasing atomic number of the target material.

Eckstein and Meyer calculated energy distributions of multiple scattering events using the simulation package SIMNRA.[72] They found that trajectories with more than

two scattering events with large deflection angles (>20°) are rare and can be neglected in cases where the incident and exit angles are close to the surface normal. Thus, for such geometries, a dual scattering model where only two scattering events take place can be used to approximate the effects of multiple scattering on backscattering spectra.

Accounting for multiple scattering effects in a backscattering spectrum is a difficult problem. A particle traversing matter undergoes a large number of interactions with the electrons and nuclei of the surrounding atoms and accounting for all of these interactions in a deterministic manner is regarded as impossible.[98, 101] Instead of treating multiple scattering in backscattering spectra analytically, another approach is to use a statistical method, such as MC simulations.

MC based simulation is a numerical approach to computing the characteristics of interatomic scattering that arises in backscattering analysis. Calculating the transport of ions through matter involves determining the scattering angle and the interatomic potential between the ion and target nucleus. The scattering of two atoms from each other can be described by the interatomic potential function,

$$V(r) = \frac{Z_1 Z_2 e^2}{r} \phi\left(\frac{r}{a}\right), \qquad \text{(V-1)}$$

where Z_1 and Z_2 are the charges of the incident and target atoms, r is the inter-nuclear separation, e^2 is the electronic charge, ϕ is the screening function, and a is the screening length. From this potential one can compute the classical scattering integral, which is discussed by Mendenhall and Weller.[48, 49] For a large number of interactions, computing the scattering integral is not a trivial task. MC integration is a numerical approach to

computing this scattering integral. For applications such as ion transport in matter, the physical process is simulated directly and there is no need for differential equations to describe the behavior of the system. The MC method proceeds by randomly sampling the probability density function, which describes probable interactions of the projectile.

The earliest report of MC simulations for calculating backscattering spectra is given by Steinbauer and coworkers.[101] They used MC simulations to calculate backscattering spectra for 100-200 keV protons incident on 1000Å Au films, determining the contributions of single, double, and multiple scattering to the total RBS spectrum. Bauer and coworkers extended this study by using protons and He^+ projectiles with energies ranging from 55 to 300 keV and Au target thicknesses ranging from 500 to 3000 Å.[102] These studies identified factors that influence multiple scattering events and showed how they can influence the shape of backscattering spectra. The main effect of multiple scattering on the shape of the Au signal was a tail at the lower energy edge and an increase in background at energies below the low energy edge. These effects were found to be most pronounced for low beam energies, and thick layers containing high-z elements, consistent with observations by Weber and coworkers.[100]

Surface Roughness

The roughness of both the substrate and the film under investigation can also influence that shape of a backscattering spectrum, especially the low energy edge of signals. The extent of roughness effects depends mainly on film thickness, experimental geometry, and the structure of the film and substrate. The effects of rough surfaces on backscattering spectra have been addressed by Edge and Bill,[103] Knudson et al.,[104]

Hobbs,[105] and Metzner et al.[106] The effects of surface roughness for thick targets were found to occur only for grazing geometries, where the angle between the incident or emerging ion and the sample surface is small. Grazing *emergence* geometries affect both the shape and height of backscattering signals while grazing *incidence* geometries mainly affect signal heights.[104] The effects of surface roughness were also found to be less significant for shallower scattering depths. More recently, MC computer simulations have been used to study surface roughness effects.[107-109] These results agree with earlier studies.

The influence of roughness effects on backscattering spectra was quantified by Mayer[110] using the computer simulation code SIMNRA. Simulations were performed for 2.0 MeV He^+ incident on 170 nm Au films having a range of root-mean-square (RMS) roughnesses. For films with an RMS roughness (σ) much smaller than the mean film thickness (d), $\sigma/d = 0.1$, only the low energy edge of the film is affected by roughness. The effect is a tail and a decrease in the yield near the low energy edge of the Au signal. This effect increases with σ/d. When σ/d is greater than about 0.6, the high energy edge of the signal begins to decrease. Even when the spectrum has been altered, the width of the signal is a good measure of the mean film thickness until the front edge is altered. A rough substrate also results in a low energy tail, which increases with roughness. As substrate roughness increases, peaks get broader and the tail extends to lower energies.[110]

Experimental Details

MC simulations of backscattering spectra were performed with GEANT4, a toolkit developed by the high-energy physics community for the simulation of the passage of

particles through matter.[111] GEANT4 takes a MC approach to produce a statistical distribution of particles as they pass through matter. Simulations were performed for two materials systems (330 Å Ta/Si and 50 Å ZrO_2/Si) and two different scattering geometries. 270 keV He ions were used for all the simulations. Particle transport calculations were performed for $5x10^8$ incident ions. Run times took about 12 hrs using an Apple G5® processor.

The scattering geometry defined for the MC simulations is illustrated in Figure 28. The target was tilted 45° relative to the beam and the scattering angle was 150 ± 0.025° for both geometries. Backscattering events were counted for a solid acceptance angle of $\pi/2 \pm \pi/4$ and $-\pi/2 \pm \pi/4$. This is larger than the acceptance angle of the actual TOF-MEBS system (~0.5 msr). An exaggerated acceptance angle reduces computation time by increasing the yield of backscattering events. Efficiency was improved further by using a method called importance biasing.[112] When a useful (large angle) scattering event occurs, additional statistically possible particle trajectories are considered. These particle trajectories are defined by cone that is divided into 32 segments. If a particle trajectory in one of the cone segments falls into the acceptance angle of the detector, 1/32 of a count is registered. This efficiency enhancement explains the non-integer number of counts in the simulated backscattering spectra.

Simulations were performed for two different exit angles, θ_2 = 15° and 75°, by positioning the detector 30° towards and away from the target normal. In this work a detector positioned towards the target normal is referred to as the negative direction and a detector positioned away from the target normal is called the positive direction. These two geometries result in significantly different outgoing ion path lengths.

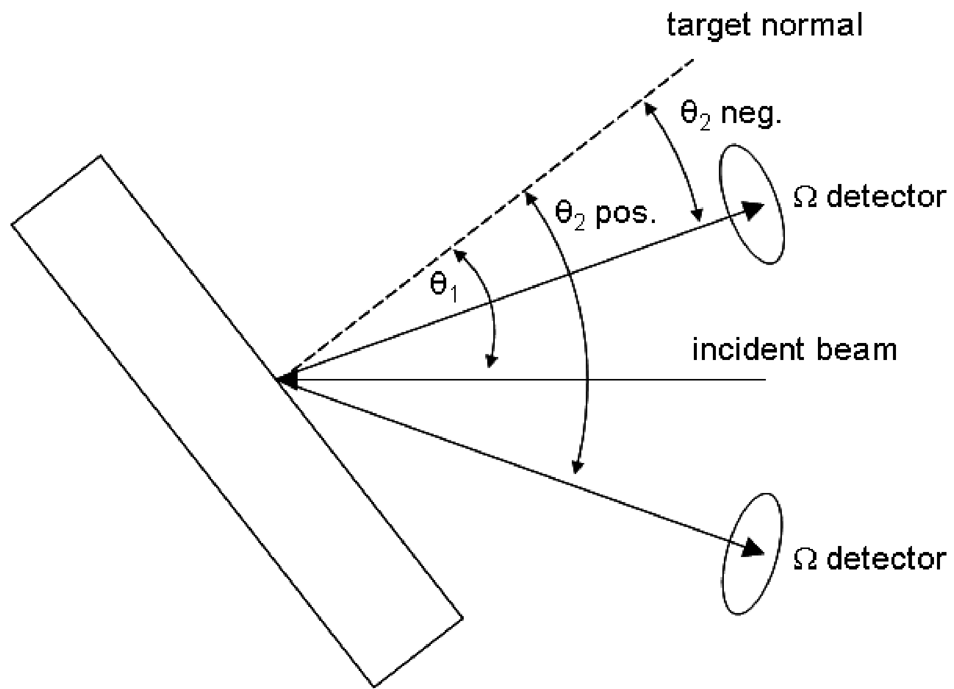

Figure 28. Target geometry for Monte Carlo simulations. θ_2 neg. is 15° and θ_2 pos. is 75°. The solid angle Ω is $\pi/2$.

The influence of surface roughness on the shape of backscattering spectra was also simulated with GEANT4. A simulation was performed for 270 keV He^+ incident on a ZrO_2/Si target with an RMS roughness of about 10 Å. The target was tilted 45° with the detector in the positive direction. Roughness was approximated by semi hemispherical structures with 20% of the layer mass in the rough layer and the remaining mass in the dense layer. The total ZrO_2 atoms/cm^2 is the same as that for a dense 50 Å film of the same material.

Backscattering spectra were also simulated with *RBSTools*. Experimental TOF-MEBS spectra were obtained from a nominally 50 Å thick ZrO_2 film deposited via MOCVD on Si and were simulated with *RBSTools* to determine thickness and composition. The experimental time-of-flight medium energy backscattering spectra shown in this work were collected using 270 keV He^+ with a target tilt of 45° and a detector positioned 30° relative to the beam in the positive direction.

The stopping powers used in the MC simulations were obtained from the Ziegler, Biersack, and Littmark (ZTB) semi-empirical formula.[113] Stopping powers used in *RBSTools* are identical to those tabulated by Rauhala.[92] *RBSTools* stopping powers are slightly higher than the ZTB values; therefore, simulations performed with *RBSTools* yield slightly lower thickness values for a given backscattering spectrum.

Backscattering spectra of a thick, high-z target (330 Å Ta/Si) were calculated with GEANT4 to illustrate an extreme case of multiple scattering, one where both the shape of the low energy edge of the high-z signal and the front edge of the underlying substrate signal are distorted. The MC simulated spectra were compared to a simulated spectrum

using the single scattering model to determine if multiple scattering events are contributing to the lower energy edge of the Zr signal in TOF-MEBS spectra.

Results and Discussion

Figures 29 and 30 show simulated spectra for 270 keV He^+ ions backscattered from 330 Å of Ta on Si for the negative and positive detector positions, respectively. The spectra shown in each figure were calculated using the single scattering model (—) and the multiple scattering model (•••). A comparison between the two simulated spectra in Figure 29 shows that there is a small amount of tailing at the low energy edge of the Ta signal, which is evidence of multiple scattering. Multiple scattering is also responsible for the increased background between the Ta and Si signal.

A comparison between the low energy edge of the Ta signal in the single and multiple scattering spectra shows that the effects of multiple scattering are not significant enough to alter the slope of the signal's back edge. However, when a more grazing exit angle is used, as in the positive detector position, the outgoing ion path length is increased and multiple scattering significantly distorts the shape of the entire backscattering spectrum (Figure 30). The slope of the low energy edge of the Ta signal from the multiple scattering spectrum is significantly lower than the slope from the single scattering spectrum and the background between the Ta and Si signal has increased so much that the Si signal is almost completely lost.

Without *a priori* information, the tail in the Ta signal could be interpreted as a gradient in the Ta concentration at the interface of the Ta layer and Si substrate. The single scattering spectrum can be fit to the multiple scattering spectrum by falsely

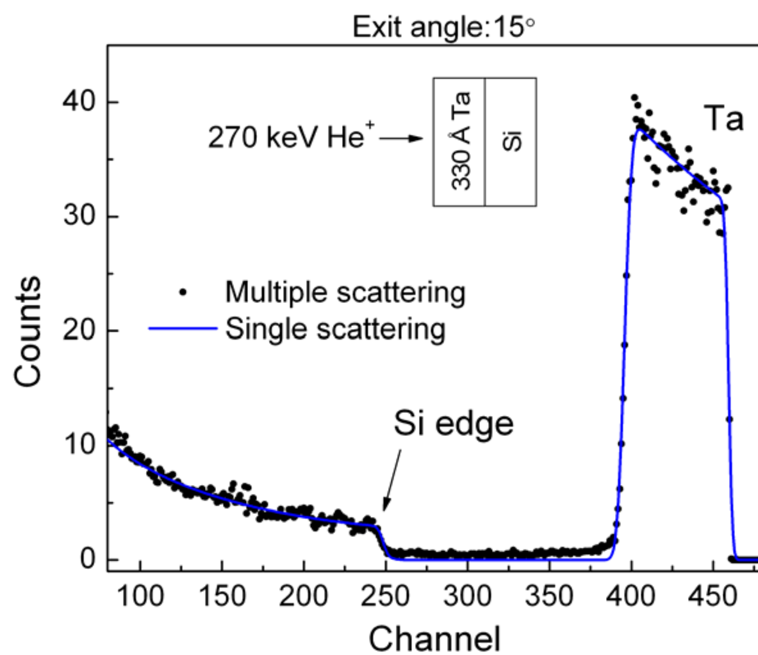

Figure 29. Simulations of backscattering spectra for 270 keV He^+ incident on 330 Å Ta/Si using a multiple and a single scattering model with the detector positioned in the negative direction (15° exit angle).

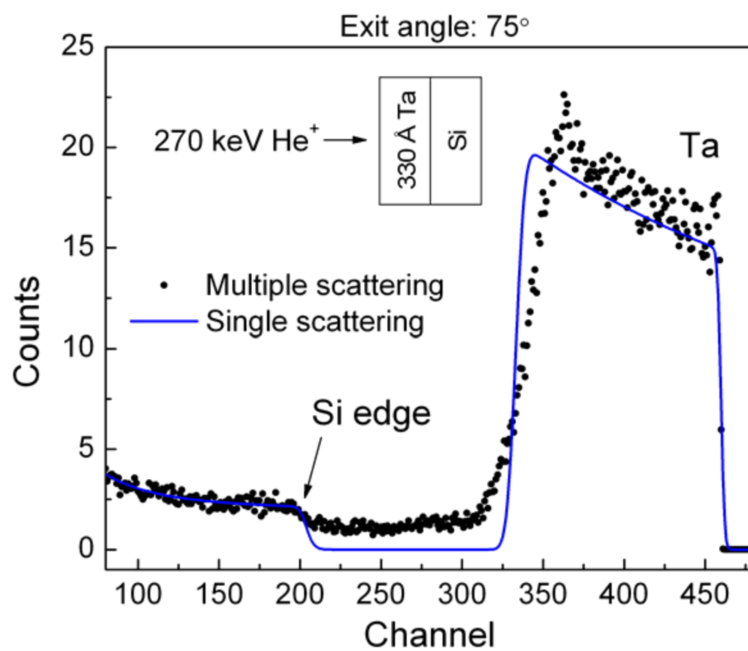

Figure 30. Simulations of backscattering spectra for 270 keV He^+ incident on 330 Å Ta/Si using a multiple and a single scattering model with the detector positioned in the positive direction (75° exit angle).

assuming that the shape of the spectrum at the low energy edge of the Ta signal and front edge of the Si signal indicates intermixing between the two elements (Figure 31). The single scattering simulation in Figure 31 was obtained with *RBSTools* using a multilayer model where the ratio of Ta to Si was varied from pure Ta to pure Si. By simulating the tail in the Ta signal with a series of layers the overall χ^2 was reduced from 389 to 52. In practice one is not likely to make this mistake when such a thick and heavy material is being analyzed with backscattering spectrometry. However, Figure 31 illustrates the point that it is possible to generate a backscattering simulation with a severely inaccurate film model and still obtain a good fit to experimental data.

Fig. 32 shows an actual time-of-flight medium energy backscattering spectrum and a *RBSTools* simulation of 270 keV He^+ on 50 Å ZrO_2/Si. The model used for the spectrum simulation consisted of a layer of ZrO_2 and a Zr-silicate layer on a Si substrate. The simulation fit at the lower energy edge of the Zr signal was improved by including an interfacial layer in the model.[114] However, it is not clear if the slight tail in the Zr signal is evidence of a silicate layer or the result of multiple scattering in the film. The inclusion of an interfacial silicate layer could be mimicking the effects of multiple scattering events that alter shape of the lower energy edge of the Zr signal. The influence of multiple scattering and surface roughness on the shape of the lower energy edge of the Zr signal was investigated by performing MC simulations of backscattering spectra obtained from this materials structure.

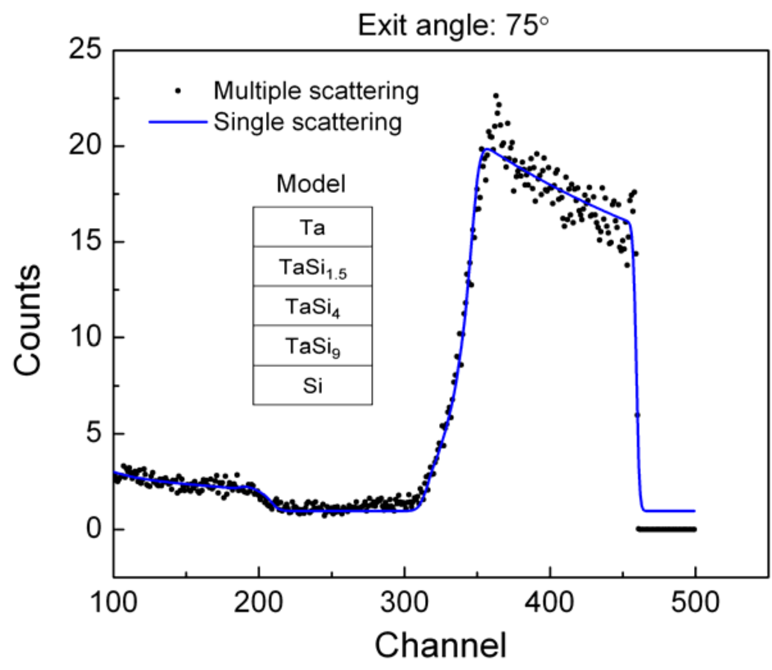

Figure 31. Simulated backscattering spectra for 270 keV He^+ incident on 330 Å Ta/Si with detector in positive position. The single scattering simulation was fit to the multiple scattering simulation using a five layer model.

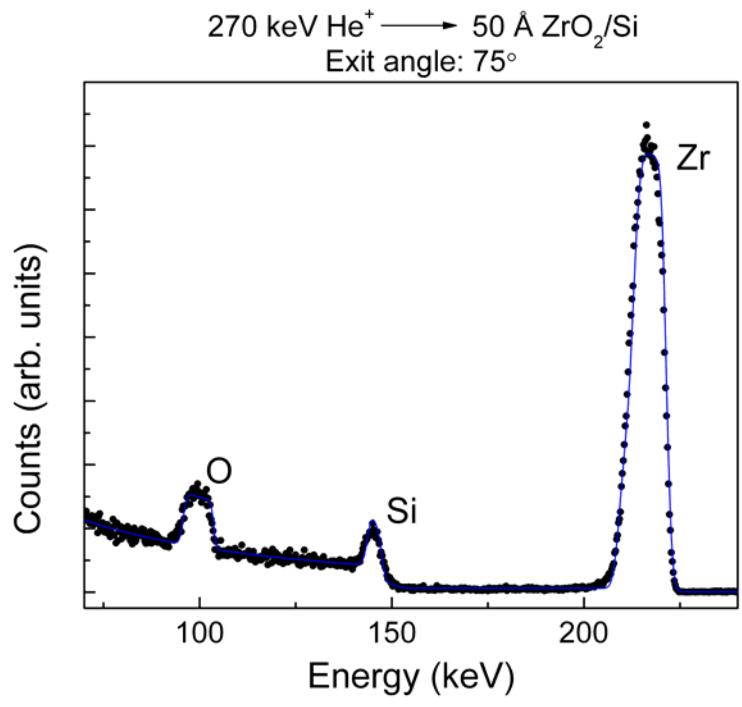

Figure 32. Experimental time-of-flight medium energy backscattering spectrum and simulation of 270 keV He^+ incident on 50 Å ZrO_2/Si

Figure 33 shows single and multiple scattering simulations of a backscattering spectrum for 270 keV He^+ incident on 50 Å ZrO_2/Si with the positive detector position. The shape of the lower energy edge of the Zr signal obtained from MC simulations does not appear to be altered by multiple scattering events. A magnified view of this region is shown in Figure 34. The error bars represent the height uncertainty. The thickness and atomic mass of the ZrO_2 layer is not large enough to result in a significant amount of multiple scattered ions. Multiple scattering events are insignificant in the ZrO_2 sample even when the exit angle for ions is 75°. However, since multiple scattering events become more significant as path length increases, they are likely to influence the shape of the Zr signal for a much thicker ZrO_2 layer or for higher target tilt angles

The surface roughness of the 50 Å ZrO_2/Si sample used in this study, measured with atomic force microscopy, is about 3.7 Å. This corresponds to an σ/d value of 0.074, which suggests that only the low energy edge of the Zr will be affected. The question of whether or not the tail seen in the experimental spectrum of the ZrO_2/Si sample can be attributed to surface roughness was addressed by performing MC simulations. A rough ZrO_2 target with a RMS roughness of about 10 Å was defined by two layers: a top rough layer that accounts for 20% of the total atoms/cm^2 of a 50 Å ZrO_2 layer, and a bottom dense layer that accounts for the remaining 80% of the total areal density. A rough morphology was approximated with semi-hemispheres, as shown in Figure 35. Semi-hemispheres, in addition to pyramids and inverted pyramids, have been used in other studies to approximate the affects of rough surfaces on backscattering spectra.[105, 106] MC simulated spectra of 50 Å ZrO_2/Si targets with and with out a topography where virtually indistinguishable for a target tilt of 45° and a positive detector position (near glancing

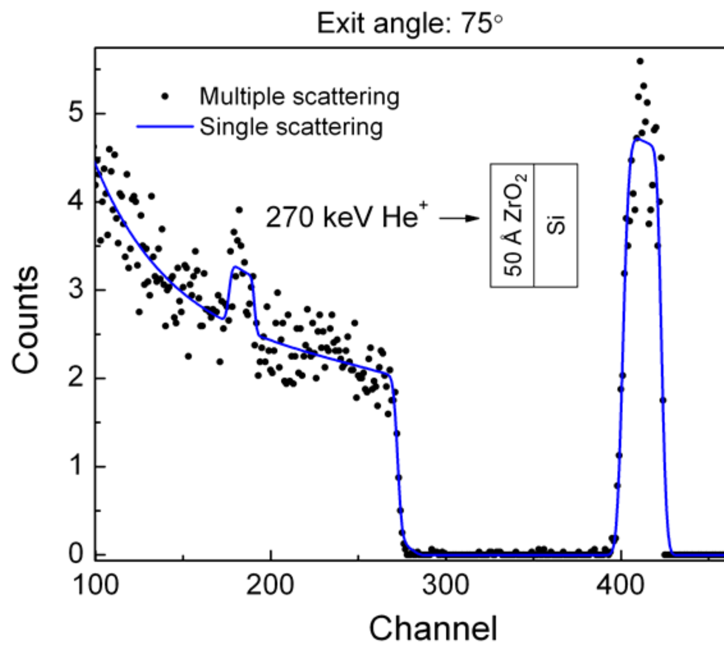

70

Figure 33. Simulations of backscattering spectra for 270 keV He^+ incident on 50 Å ZrO_2/Si using a multiple and a single scattering model with the detector positioned in the negative direction (75° exit angle).

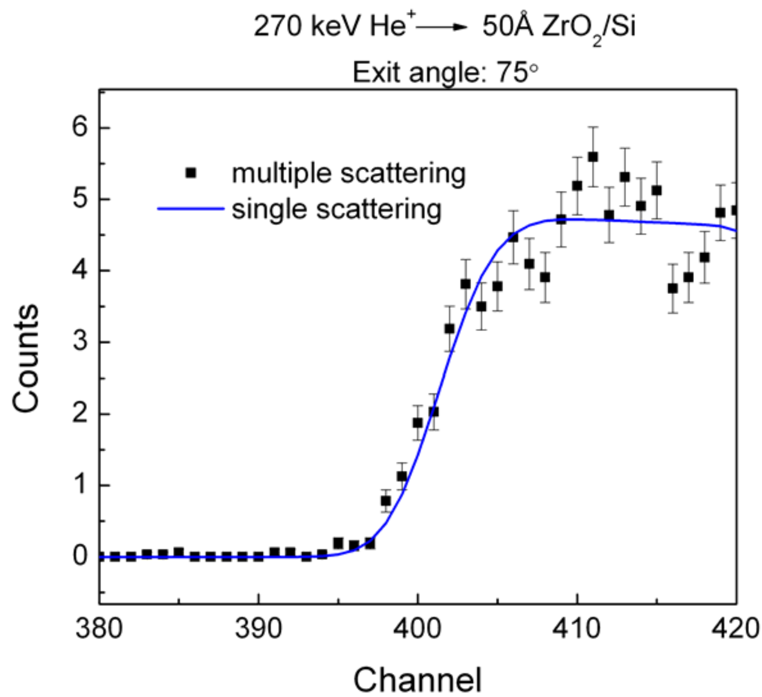

Figure 34. Lower energy edge of Zr signal. Multiple scattering has negligible influence on shape of Zr signal's low energy edge.

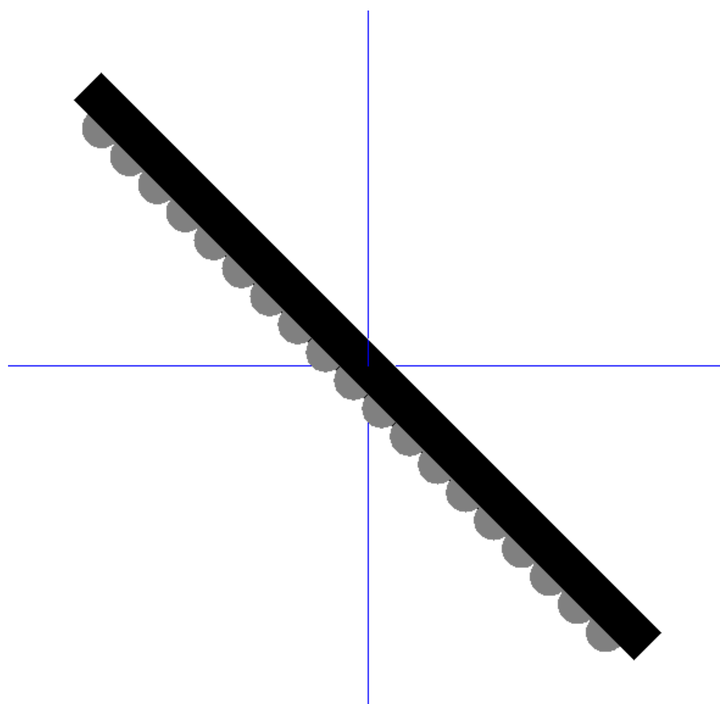

Figure 35. Two-dimensional view of rough ZrO_2 target used for MC simulations. The size of the semi-hemispheres in this figure was exaggerated to help visualization.

geometry). This suggests that surface roughness has a negligible influence on the low energy tail of the Zr signal. The tail seen in the ZrO_2/Si experimental backscattering spectrum indicates a transition region where film composition changes from ZrO_2 to a Zr silicate, and the tail is not due to multiple scattering or surface roughness effects.

Conclusions

The influence of multiple scattering and surface roughness on the shape of backscattering spectra was studied by simulating backscattering spectra using MC calculations. For thick high-z layer multiple scattering affects not only the low energy edge of the high-z signal, but can also distort the front edge of the underlying substrate signal. For the analysis of thin ZrO_2 films on Si with a target tilt of 45° and an exit angle of 75°, multiple scattering and roughness does not affect the shape of the spectrum, including the low energy edge of the Zr signal. However, for thicker ZrO_2 films and higher tilt angles, one may not be able to neglect the effects of multiple scattering. Surface roughness effects may also significantly affect the shape of a spectrum at higher tilt angles.

CHAPTER VI

EVALUATION OF ENERGY AND DEPTH RESOLUTION WITH TOF-MEBS

The interface between high-k material and the underlying substrate plays a significant role in determining the overall electrical properties of high-κ gate structure. Undesirable interfacial layers are prone to form at the high-κ/Si interface. These layers have a lower permittivity than the high-κ material, compromising the equivalent oxide thickness achievable with the material. Time-of-flight medium energy backscattering (TOF-MEBS) has been used to characterize the material properties of this interfacial region.[114]

To extract as much information from this region as possible, it is necessary to optimize the depth resolution of the TOF-MEBS system. The depth resolution of the TOF-MEBS system is influenced by various experimental conditions such as beam energy, target tilt angle, and probe depth. Past analyses of these high-κ structures, were performed with 270 keV He^+ and a tilt angle of 45°. The TOF-MEBS system is operated at its maximum beam energy of 270 keV because the stopping power of He^+ in most materials is near 500 keV, thereby maximizing the total energy loss of the incident ions.[115] Tilting the sample normal 45° relative to the beam enables channeling down the <110> axis, which enhances the signal from any element overlapping the substrate signal. However, until this study, it has not been determined whether or not these are the optimal experimental conditions for enhanced depth resolution. This study investigates the energy spread and depth resolution of the TOF-MEBS system as a function of beam

energy and tilt angle and determines the experimental configuration that optimizes depth resolution.

The optimization of backscattering systems for improving depth resolution has been the subject of a number of studies.[86, 87, 116-118] One factor that significantly limits depth resolution is the ion detection system, typically a silicon surface barrier detector (SSBD) for Rutherford backscattering spectrometry (RBS) analysis. Other detection systems that have been used to improve energy resolution, thereby improving depth resolution, include magnetic spectrometers,[86, 87] electrostatic energy analyzers,[74, 75, 77] and time-of-flight spectrometers.[62,78,88] Unlike the other particle detection systems mentioned, the resolution of the time-of-flight system strongly depends on particle energy.[83]

A number of factors contribute to the resolution of the TOF spectrometer used in this work and were previously evaluated by McDonald and coworkers.[83] The primary factors were shown to be the uncertainty of ion path length, kinematic dispersion from the finite detector solid angle, straggling in the carbon start foil, and variability of the start foil thickness. Variability in the start foil was identified as the most significant factor. They improved the resolution of the spectrometer significantly by using a diamond-like carbon start foil, which is smoother and thinner than conventional arc-deposited carbon foils.

Weller and coworkers optimized the resolution of the TOF-MEBS system through a redesign of the TOF spectrometer.[89] They tilted the angle of the carbon start foil and the stop detector with respect to the spectrometer axis by 30° and 15°, respectively. These adjustments reduced the timing uncertainty attributable to path length differences

and reduced the kinematic dispersion. A depth resolution of ~2 nm was measured after altering the geometry of the spectrometer.

Calculating Depth Resolution

The depth resolution δx of an energy loss experiment such TOF-MEBS at some depth x is defined as the depth interval that corresponds to the total detected ion energy spread, δE:

$$\delta x = \frac{\delta E}{[S]} \qquad \text{(VI-1)}$$

where δE is also referred to as the total system energy resolution, and [S] is the stopping factor. The stopping factor [S] is given by

$$[S] = \frac{K^2}{\cos\theta_1} S_1 + \frac{1}{\cos\theta_2} S_2 , \qquad \text{(VI-2)}$$

where K is the Rutherford kinematic factor, S_1 and S_2 are the mean stopping powers for the incident and exit beam, respectively; θ_1 and θ_2 are the angles between the sample normal and the direction of the incident beam and of the scattered ions, respectively. The stopping factor is easily calculated from stopping tables[119] and knowledge of the experimental geometry.

The total energy resolution of the system includes contributions from a number of energy spread factors: energy resolution of the detection system, straggling, geometrical

spread, multiple scattering, surface roughness, isotopic effect, energy spread of incident ion beam, and angular spread of incident ion beam.

Geometrical spread is due to a finite beam spot size and detector acceptance angle (Figure 36). The factors geometrical spread, multiple scattering, surface roughness, and angular spread of the incident beam all result in a range of scattering angles and projectile path lengths, although by different mechanisms. The effects of multiple scattering and surface roughness were discussed in detail in the previous chapter. The different mass of each isotope results in a range of backscattered particle energies, and therefore, peak locations. The backscattering spectrum from a sample that contains several isotopes is the summation of the individual peaks generated by each isotope, which increases the width of the backscattering signal from the element. Angular spread of the incident ion beam can result if there are fluctuations in the current of the analyzing magnet or in the electric and magnetic fields of the lenses used for steering and collimating the beam. This factor and geometric spread can be reduced by using smaller aperture sizes.

Assuming that the distribution of each energy spread contribution is near Gaussian in shape and each factor uncorrelated,[117] the total energy spread is determined by adding each component in quadrature:

$$\delta E^2 = \sum \delta E_i{}^2 \qquad \text{(VI-3)}$$

For a layer that is infinitesimally thin, the full-width half-max (FWHM) of the signal from that layer corresponds to the total system energy resolution, δE, which is the lowest

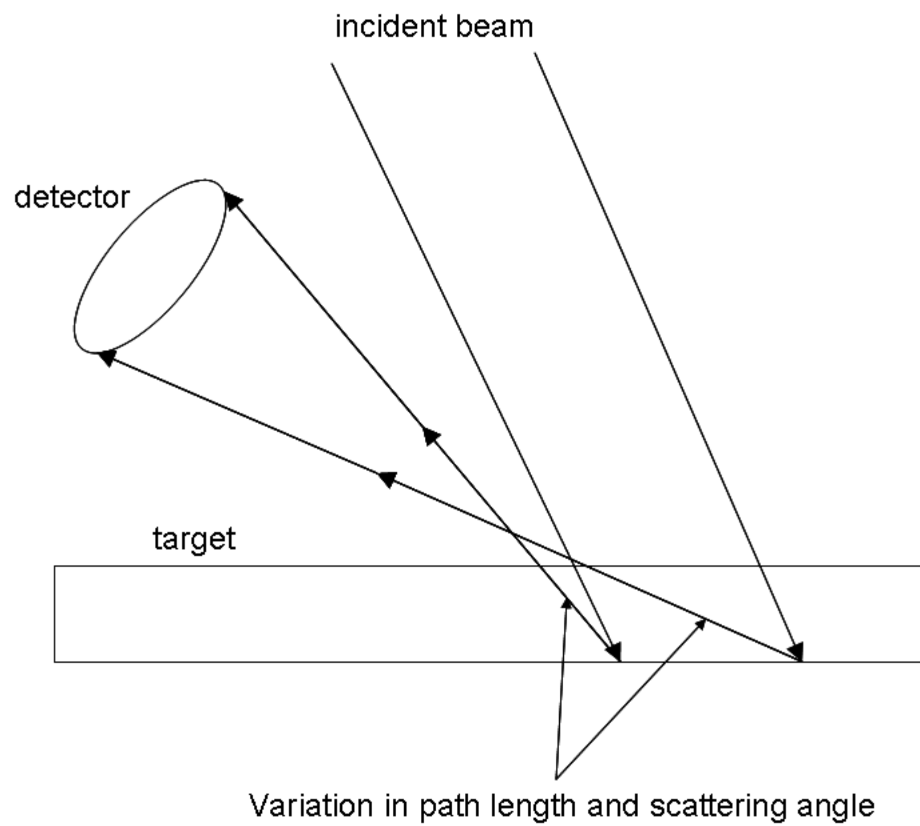

Figure 36. There is variation in the path length and scattering angle due to the finite size of the incident beam and detector acceptance angle.

resolvable energy width.[51] This value is equivalent to the width of the edge of an error function from 12% to 88% of the edge height.[120]

Theoretical values for energy spread and depth resolution were determined using Szilagyi's DEPTH package.[118, 121] DEPTH is available for downloading from Szilagyi's *IBIS Document Library*.[122] A user's manual is available with the download. DEPTH was designed to determine optimum depth resolution in ion beam analysis, particularly RBS, elastic recoil detection analysis (ERDA), and nuclear reaction analysis (NRA). Calculations were performed for He^+ ions traversing Al and scattering from Er-167. DEPTH was used to determine energy straggling, geometrical spread, and multiple scattering. DEPTH does not have the ability to account for surface roughness, although it can be a significant factor at high tilt angles. Since the stability of the accelerating voltage for the TOF-MEBS system is less than 10 V of ripple at full power, the energy spread of the beam was assumed to be negligible. The angular spread of the incident beam was also considered negligible in this study. If energy and angular spread of the beam are present, their effects would be manifested in the TOF spectrometer resolution measurements made as part of this study.

Optimizing Depth Resolution

Depth resolution can be optimized by minimizing the various energy spread factors contributing to δE, and by maximizing the stopping factor [S]. [S] is maximized by increasing the stopping power or by increasing the target tilt, thereby increasing the pathlength of ions in the target. Figure 37 shows the tilt angle (theta) dependence of [S] for three different beam energies. [S] increases asymptotically with theta to 60°, the

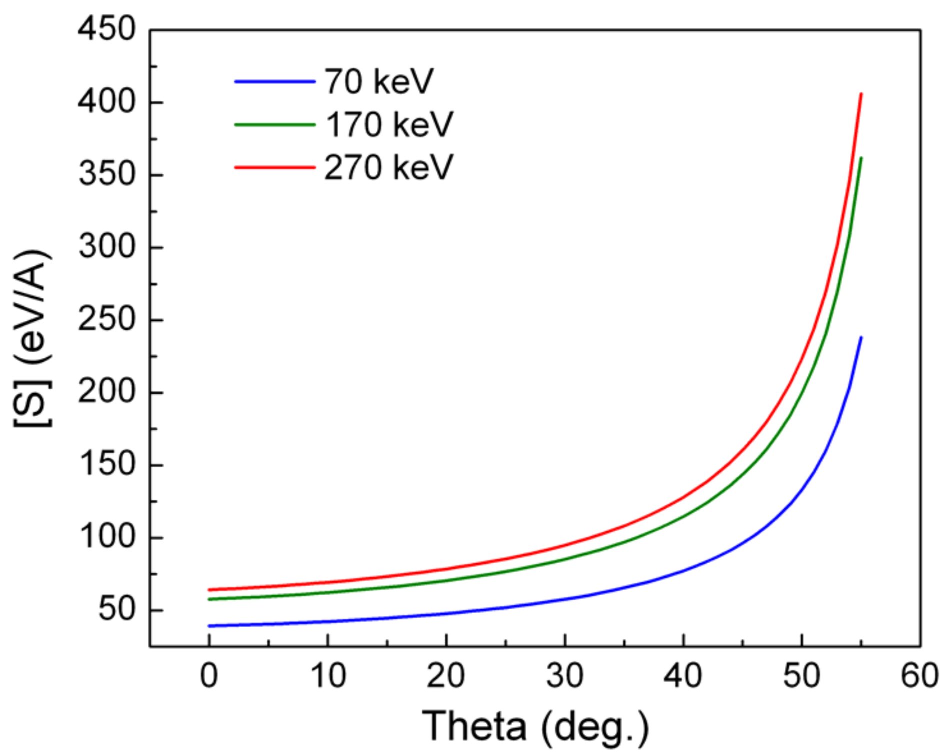

Figure 37. Energy loss factor [S] for 60, 170, and 270 keV He^{+} in Al over tilt angles 0 to 55°.

angle at which the sample surface is parallel to the spectrometer and no backscattered particles are detected. Figure 38 plots [S] for He^+ in Al as a function of beam energy for target tilts of 0, 30, and 45°. As in most materials, [S] of Al reaches its maximum around 500 keV for He^+.[110]

The analysis depth significantly affects depth resolution.[115] For backscattering analysis at the near surface region, the detector resolution has been shown to dominate depth resolution. As the depth of analysis increases, energy straggling and multiple scattering begin to dominate depth resolution.

By employing low-angle scattering arrangements with a high energy-resolution detection system the depth resolution can be significantly improved. Glancing incident geometry increases the path length that the probe beam must traverse, thereby increasing the total energy lost by the ion. As a result, the energy difference between ions scattered from the front and back of a film is much larger than the energy resolution of the system, and backscattering profile of the layer is better resolved.[86]

Equation (VI-2) suggests that depth resolution can be improved without bound by continuing to increase the target tilt angle. However, this also increases the ion path lengths during incident and exit paths, resulting in increased energy spread from surface roughness, energy straggling, multiple scattering.[117] Thus, for large tilt angles the increase in [S] may be outweighed by these factors.

Using heavier projectiles can also improve depth resolution because stopping power increases with projectile mass. Figure 39 shows stopping power in ZrO_2 as a function of projectile energy for the projectile H^+, He^+, Li^+, C^+, and N^+. O'Connor and Chunyu showed that for 2 MeV ions and depths less than 10 nm, heavy projectiles (C^+,

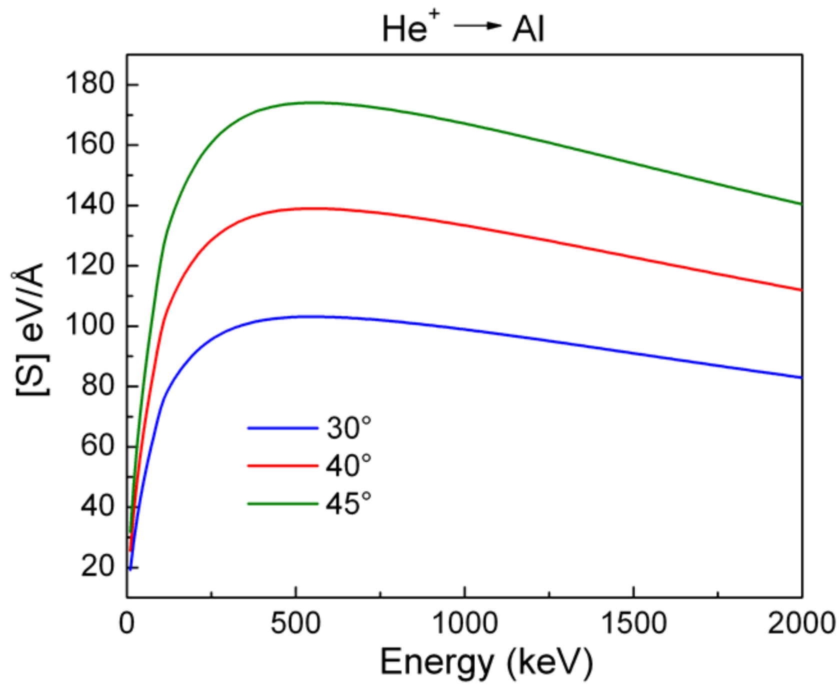

Figure 38. Energy loss factor [S] for He^{+} in Al (scattered from Er) as a function of beam energy for target tilts of 0, 30, and 45°. [S] reaches a maximum around 500 keV for He^{+} in most materials.

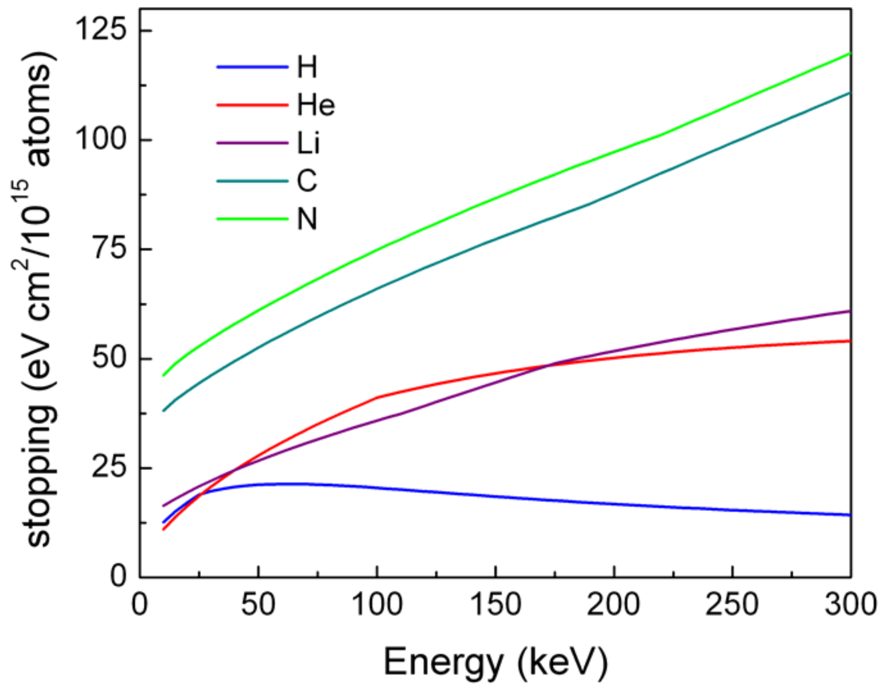

Figure 39. Stopping of H^{+}, He^{+}, Li^{+}, C^{+}, and N^{+} projectiles in Al as a function of energy.

N^+) improved the depth resolution by a factor of up to six, when compared to light projectiles (He^+, Li^+). Such an improvement is not seen at greater depths because multiple scattering and straggling dominate, both of which increase with projectile mass.[117] Although heavier projectiles may improve depth resolution in the near surface region, for TOF spectrometers the increase in projectile mass reduces the spectrometer's intrinsic efficiency, the probability that a counting event will be registered.[65, 66] This is mainly due to an increase in multiple scattering in the carbon start foil, which can alter projectile trajectories enough that they miss the stop detector.

Figure 39 also shows that the stopping maximum of hydrogen in Al occurs with in the operation range of the TOF-MEBS system, around 64 keV. The stopping of He^+ in Al at 270 keV is about two times greater than the stopping of H^+ in Al at 64 keV. The corresponding depth resolution for scattering near the surface with a tilt angle 45° is 11 Å for He^+ and 26 Å for H^+. Thus, switching the TOF-MEBS system to a lighter projectile in order to operate at a lower beam energy that is near the stopping maximum does not result in an improvement in depth resolution.

With stopping factor [S] reaching a maximum around 500 keV for He^+ in most elements, it follows that depth resolution can be improved by operating in this region. However, this may not be the case for detection systems where the energy resolution degrades with increasing energy. If the detector resolution has a strong dependence on energy, the depth resolution may be optimized at energies lower than where the stopping power is maximized.

Experimental Procedure

All experiments were performed using He^+ ions and a beam current of ~ 40 nA. The experimental geometry for TOF-MEBS experiments is illustrated in Figure 40. Due to the position of the spectrometer, the maximum usable tilt angle is less than 60°.

The resolution of the spectrometer was determined for backscattered energies ranging from ~50 to 230 keV. The resolution of the spectrometer was assumed to be equal to the front edge width, as defined by the energy difference between the 12% and 88% height of the Zr peak in a spectrum obtained from a ZrO_2/Si sample (Figure 41).

The sample was oriented normal to the beam to reduce spread that may arise from surface roughness. The function describing the linear fit to the plot of detector resolution versus detected energy was used to determine spectrometer resolution at a particular energy. The overall energy spread of the system was determined for tilt angles ranging from 5 to 55° and beam energies ranging from 60 to 270 keV.

In this study the overall energy spread was obtained from backscattering spectra of a heteroepitaxial materials system deposited by Professor Palmstrom's group at the University of Minnesota. This system consisted of 5 monoloayers (lattice constant a_0 = 5.76 Å) of ErAs deposited by molecular beam epitaxy on a GaAs (100) substrate. The ErAs layer was capped with 55 Å of Al. This system was chosen because the interface with the substrate is abrupt and the surface is smooth. AFM analysis of the system with the Al cap indicated an RMS roughness of about 1 nm. Our group has used TOF-MEBS to study the interfacial region between ~60Å ZrO_2 films and Si, so the depth resolution of the TOF-MEBS system at this depth (corresponding to the Al/ErAs interface) is of particular interest to us.

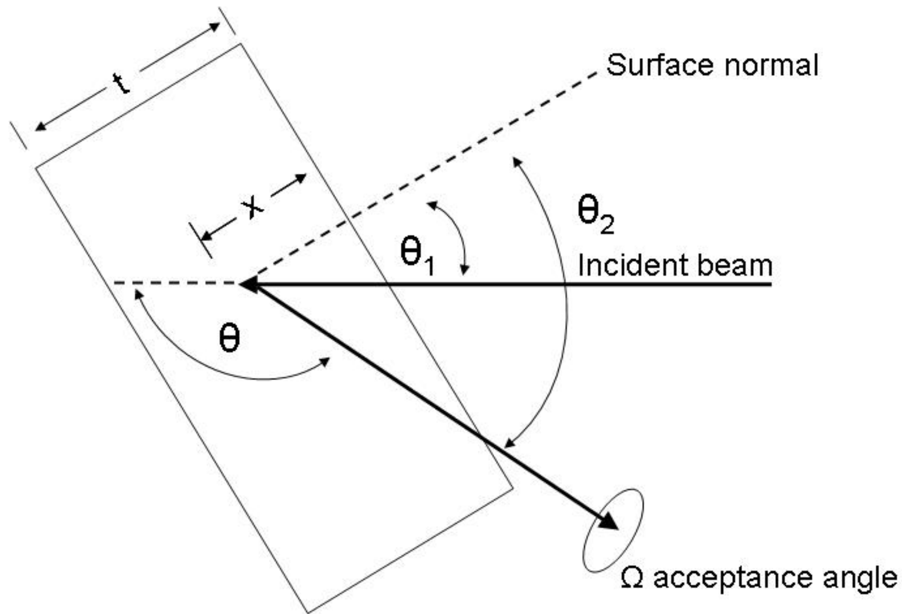

Figure 40. Experimental geometry for TOF-MEBS analysis.

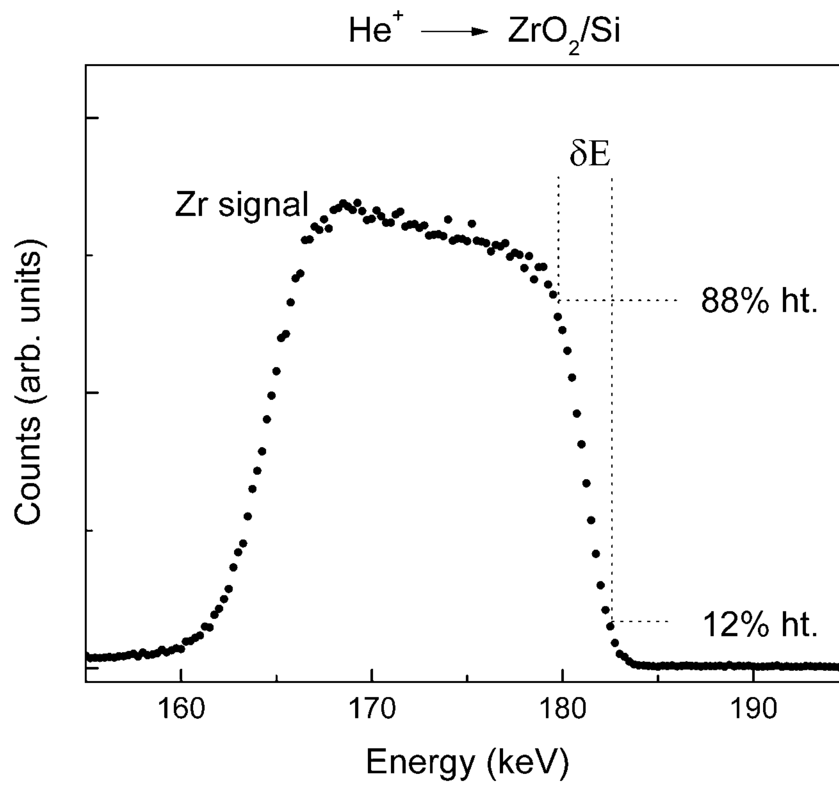

Figure 41. Zirconium signal in a ZrO_2/Si spectrum obtained with 220 keV He^+.

The system's energy resolution for scattering at a depth of 55 Å was assumed to be equal to the front edge width (12-88% peak height) of the isolated Er peak in a spectrum obtained from heteroepitaxial sample. A backscattering spectrum of this materials system is shown in Figure 42. The lower limit for depth resolution was determined by using the detector resolution as the only factor contributing to energy spread. This corresponds to scattering from the surface.

For DEPTH calculations, the beam spot shape and size can be defined. By irradiating a piece of thermal paper with the ion beam, the beam spot was found to be roughly rectangular with a height of 6 mm and a width of 3 mm. The distance of the detector from the target was taken as 250 mm and the diameter of the circular detector aperture was set to 12.5 mm. Since beam energy spread and angular spread of the beam were assumed negligible, these parameters were set to 0.

Results and Discussion

The TOF-MEBS system uses a spectrometer that offers improved sensitivity and depth resolution compared to conventional Rutherford backscattering systems. However, the system is limited to medium energy ions (< 300 keV) because the spectrometer resolution degrades with beam energy, as shown in Figure 43. The system resolution is defined in this work as the width of the leading edge of the Zr signal in ZrO_2/Si backscattering spectra. The energy dependence of the spectrometer was characterized using He^+ at energies ranging from 60 to 270 keV. A linear fit of the data resulted in the

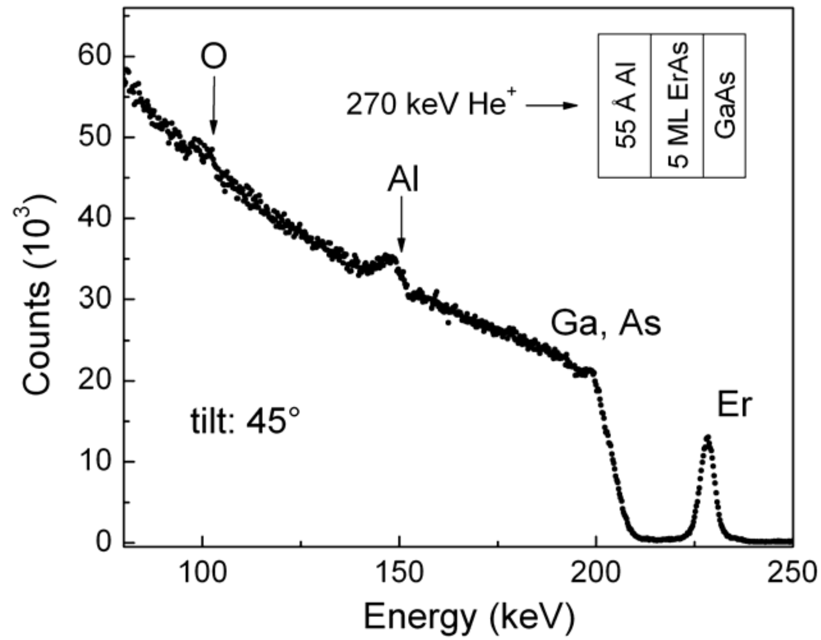

Figure 42. 270 keV He^+ backscattering spectrum of ErAs heteroepitaxial materials system. The front edge width of the Er signal was taken as the total energy spread of the time-of-flight system.

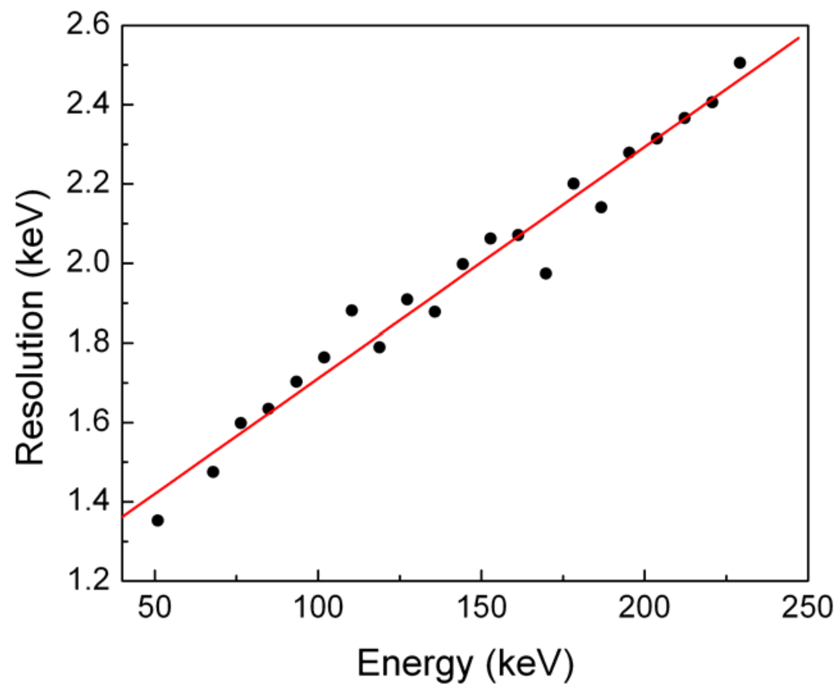

Figure 43. Measured TOF spectrometer energy resolution versus detected particle energy for He^+ backscattered from ZrO_2 at beam energies from 60 to 270 keV.

resolution function 1129 eV + 0.0058 *E*, where E is the energy of the He^+ particle entering the spectrometer in eV.

McDonald and co-workers also determined the energy dependence of Vanderbilt's time-of-flight spectrometer resolution.[83] Backscattering spectra were acquired from a set of SiO_2/Si samples at beam energies from 150 to 270 keV. By measuring the front edge width of the oxygen signal, they determined at resolution function of 728 eV + 0.006 *E*. For the study presented in this chapter, the energy resolution function was acquired from a Zr signal, which contains much better statistics (less uncertainty) than an oxygen signal for the same integrated charge. The better statistics is due to the relatively greater number of counts obtained from the Zr signal compared to the O signal, which is the result of larger scattering cross sections.

Because of the energy dependence of the TOF spectrometer, the increased stopping power and reduced energy resolution that are associated with higher beam energies must be balanced. Fig. 44 plots calculated depth resolution at the surface as a function of beam energy for two different detectors: one having constant 2 keV energy resolution and the other having the same energy resolution function determined for the spectrometer at Vanderbilt. With a constant energy resolution a backscattering system achieves an optimum depth resolution at a much higher energy, around 1000 keV.

Energy spread and depth resolution were both calculated and measured as a function of tilt angle for 270 keV He^+ in Al. Figure 45 shows the calculated results where the energy spread factors include spectrometer resolution, energy straggling, geometrical spread, and multiple scattering in and out. The resolution of the time-of-flight spectrometer is the most significant factor at shallow tilt angles where the total ion

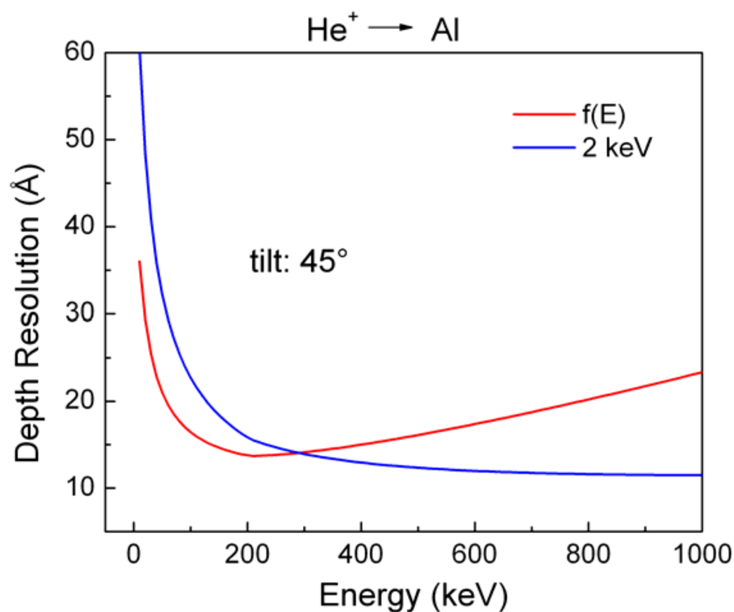

Figure 44. Depth resolution at the surface of Al as a function of detected energy calculated for a detector with constant energy resolution of 2 keV and a detector having the energy dependence of the time-of-flight spectrometer: 1129 eV + 0.0058 *E*, where *E* is the detected particle energy.

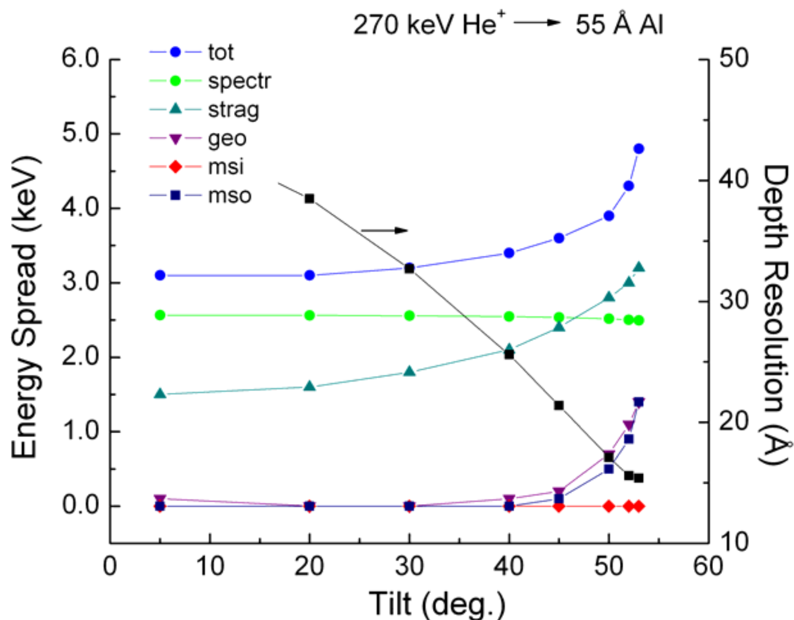

Figure 45. Calculated energy spread and depth resolution as a function of target tilt for 270 keV He^+ in 55 Å Al. Energy spread factors include spectrometer resolution (spectr), straggling (strag), geometrical (geo), and multiple scattering in (msi) and out (mso). The total energy spread (tot) is equal to the factors summed in quadrature.

path length is relatively short. However, as the target is tilted and path lengths increase, straggling, geometrical spread, and multiple scattering out become more significant. Energy straggling is the most significant factor at the broadest tilt angles, although contributions from geometric spread and multiple scattering have also increased dramatically. Multiple scattering *out* is much more significant than multiple scattering *in* because the path length of ions exiting the target is much longer than those entering the target. Depth resolution improves with increasing tilt angle, but appears to be approaching a minimum at the most extreme tilt angle.

DEPTH calculations were also performed for 270 keV He^+ in ZrO_2. Figure 46 shows both depth resolution and the various energy spread factors as a function of target tilt. The calculations were performed for He^+ scattering from Zr atoms. The trends shown in this figure are similar to those discussed for He in Al. For He in ZrO_2, depth resolution reaches a minimum (14 Å at 50°) in the range of target tilts used in the calculations. Multiple scattering of He ions is significant in ZrO_2 than it is in Al. Multiple scattering out and energy straggling are the dominant factors contributing to depth resolution at the most extreme tilt angle. Many of the TOF-MEBS experiments in this work were performed using 270 keV He^+ with the target tilted 45°. The calculated depth resolution of the system at these conditions for scattering from Zr at a depth of 50 Å is about 16 Å.

Measured energy spread and depth resolution results for He^+ in Al are plotted in Figure 47. As expected, the energy spread of the system increases as tilt angle approaches the cut-off angle. Depth resolution improves with increasing target tilt from 5° to 54° where it reaches a minimum of ~12 Å. A minimum was not observed for

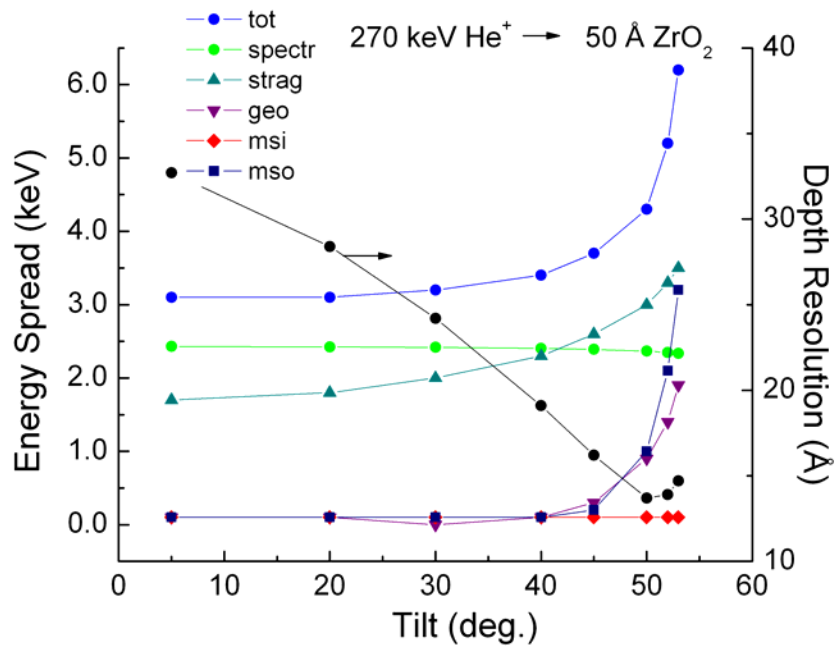

Figure 46. Energy spread and depth resolution as a function of target tilt for 270 keV He^+ in ZrO_2. Energy spread factors include spectrometer resolution (spectr), straggling (strag), geometrical (geo), and multiple scattering in (msi) and out (mso). The total energy spread (tot) is equal to the factors summed in quadrature.

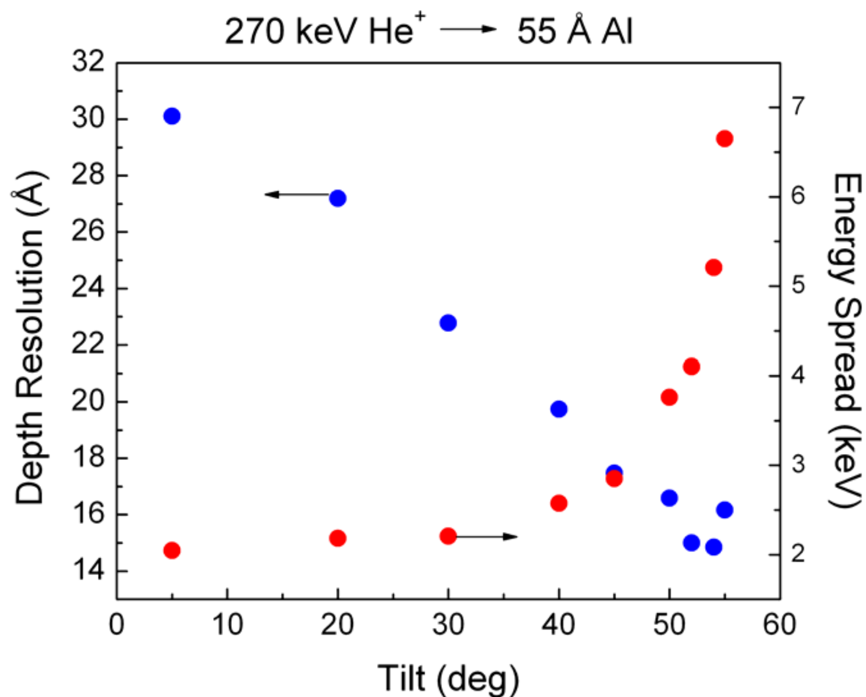

Figure 47. Total measured energy spread and depth resolution as a function of target tilt (θ_1) for 270 keV He^+ in 55 Å Al

calculated depth resolution as target tilt increased. However, calculations at tilt angles higher than 53° were not possible because DEPTH indicated that calculates contained significant error. At broad tilt angles surface roughness can be a significant limitation to depth resolution.[109] Therefore, surface roughness effects, which were not included in the calculations, are likely to have contributed to the degradation of measured depth resolution results.

The depth resolution of the TOF-MEBS system was measured for beam energies ranging from 60 to 270 keV. Figure 48 shows depth resolution over this energy range for target tilts of 30, 40, and 45°. The optimum depth resolution at a tilt of 45° is of particular interest because axial channeling is possible for analysis of thin films on (100) crystalline substrates. Channeling is desirable because it reduces the backscattering signal from the underlying crystalline substrate, thereby enhancing any overlapping signals. For all three tilt angles the best depth resolution is obtained for a beam energy of 170 keV. Interpolating between the 120 and 170 keV gives an optimum depth resolution around 150 keV. Depth resolution is best at the largest tilt angle of 45°. The best measured depth resolution value is shown to be ~16 Å. This value is only about 12% greater than the lower limit calculated with spectrometer resolution as the only energy spread factor contributing to depth resolution. DEPTH calculations also indicated that a theoretical minimum for depth resolution occurred for a beam energy around 150 keV (Figure 49). Calculated depth resolution values are higher than measured values for the target tilt angles and beam energies used in this experiment, which is probably due to the Al layer thickness value obtained by fitting the Al signal with a simulated spectrum. The Al cap was assumed to be pure Al, but it is likely that the Al underwent partial

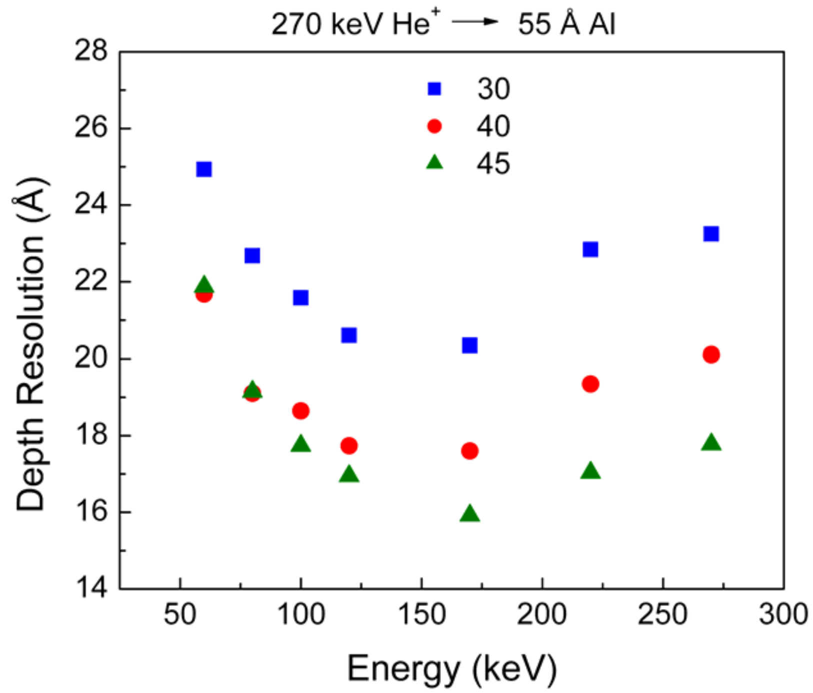

Figure 48. TOF-MEBS depth resolution versus beam energy for tilt angles (θ_1) at 30, 40, and 45°. Depth resolution reaches a minimum around 170 keV for all three tilt angles shown.

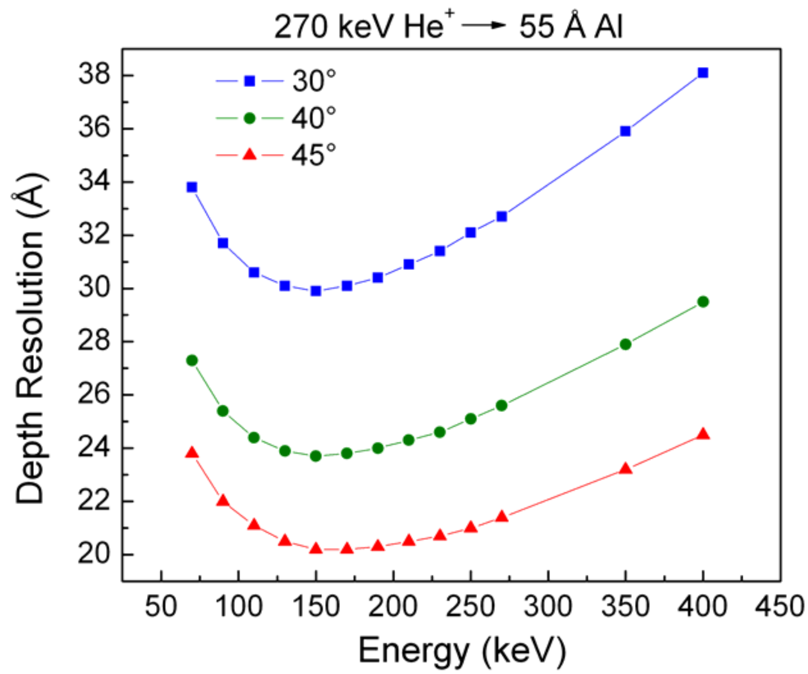

Figure 49. Calculated depth resolution versus beam energy for tilt angles (θ_1) at 30, 40, and 45°. Depth resolution reaches a minimum around 150 keV for all three tilt angles shown.

oxidation. Oxidized Al has a higher stopping power than pure Al. With a higher stopping power for the same peak width, a smaller thickness value will be obtained from a best fit simulation.

Experimental and calculated depth resolution values might also differ because of the way in which energy spread was determined. For such a thin layer of ErAs, the front edge width of the Er signal might not be an accurate measure of the overall energy spread. The FWHM of the Er signal would provide a measure of the overall system energy spread. However, measuring energy spread in such a manner would over-estimate energy spread due to the finite thickness of the layer where energy loss, straggling, multiple scattering, and isotopic spread would contribute to the width of the Er signal.

Although depth resolution achieves its optimum value for beam energies around 150 keV, the difference between depth resolution at this beam energy and the maximum operating energy of 270 keV is less than 2 Å. A comparison between Al stopping power values at 270 and 500 keV shows that the difference is small, ~5%. The difference in stopping powers for a dielectric material like ZrO_2 is about 20%. Thus, despite that fact that the TOF-MEBS system cannot be operated at beam energies near stopping maximum, little in terms of depth resolution is lost by operating at lower energies. Of course, the amount of resolution lost will depend on the material under investigation.

An additional factor that should be considered when operating at lower beam energies is mass resolution. If elements of similar mass are present in the sample, it would be more desirable to operate the TOF-MEBS system at 270 keV, as opposed to 170 keV, and sacrifice the additional improvement in depth resolution associated with lower beam energies. Mass resolution, which is proportional to energy resolution and

inversely proportional to beam energy, is about 25% better at 270 keV compared to mass resolution at 170 keV.

Conclusions

The energy and depth resolution of the TOF-MEBS system has been evaluated at a range of beam energies and target tilt angles. The spectrometer resolution was shown to increase linearly with detected particle energy. Due to the energy dependence of the TOF spectrometer, optimum depth resolution is achieved at beam energies of ~150 keV, significantly lower than the stopping power maximum near 500 keV. The total energy spread increases asymptotically for increasing tilt angles, which results in a degradation in depth resolution at tilt angles greater than 54°. The depth resolution at this tilt angle is a few angstroms better than the optimum depth resolution achieved at 150 keV and 45° tilt. However, for the analysis of films on (100) crystalline substrates operating at 45° may be more desirable so that axial channeling can be achieved.

CHAPTER VII

CHARACTERIZATION OF ZrO_2 FILMS DEPOSITED BY MOCVD ON HYDROGEN TERMINATED Si AND NATIVE Si OXIDE SURFACES

Scaling of metal-oxide-semiconductor field effect transistors (MOSFET) is required to further increase the performance and functionality of microelectronics devices. This scaling process has created the need for new materials that can replace SiO_2 as the gate dielectric material.

Unlike SiO_2, which can be thermally grown on Si, high-κ films must be deposited. The deposition process and the nature of the predeposition surface can strongly affect the properties of the high-k material and the interface with Si. It is highly desirable that the new high-κ dielectric material be thermodynamically stable on Si and have a high quality interface with Si. Many of the materials under investigation have an unstable interface with Si, which results in the formation of an interfacial oxide layer that compromises the overall capacitance of the gate stack. In order to integrate high-κ materials into CMOS technology, a complete understanding of this interfacial region is critical.[2]

In this study, ZrO_2 films were deposited on hydrogen terminated Si and native Si oxide surfaces. The nature of these surfaces can significantly affect the composition and density of the films deposited on them. The deposition of ZrO_2 on H-terminated Si has been shown to result in the formation of an interfacial layer for a number of deposition methods, including MOCVD,[14, 18, 96] ALCVD,[17, 73, 94] physical vapor deposition,[34] and sputtering[77]. However, the results of independent studies concerning the chemical nature of the interfacial layer in as-deposited ZrO_2 films on Si are not consistent. Some studies

suggest that the interface is a Zr-silicate[14, 18, 34, 96] with an average Zr concentration ranging from 3 at % to about 6 at%. Other studies report a SiO_x layer.[94, 123] A gradient in Zr concentration in the interfacial layer has also been reported.[17, 124] In contrast to ZrO_2 films deposited on H-Si surfaces, those deposited on oxide surfaces have been shown to form abrupt interfaces and to be stable against silicate formation.[73, 125] However, a silicate has been observed at the interface between ZrO_2 films and native oxide surfaces.[35]

Experimental Details

ZrO_2 films were deposited by MOCVD in a single wafer UHV compatible CVD system.[126] Depositions were performed at temperatures of 350, 400, and 450°C on two different substrates: hydrogen terminated silicon (H-Si) and Si native oxide (N.O.). Films were grown to thicknesses of 30 and 60 Å. Film growth was monitored with an *in-situ* J.A. Woolam model M-2000D spectroscopic ellipsometer. This device uses a QTH lamp and a D_2 lamp to generate a beam with a photon energy range of 1.2 – 6.5 eV. Additional details of these depositions and in-situ spectroscopic ellipsometry (SE) analyses have been documented by Song and Rogers.[126] TOF-MEBS analyses were performed on twelve samples with 270 keV He^+. Channeling was achieved by tilting the target normal 45° relative to the beam. A total charge of 100 μC was collected for each experiment using a beam current of 50 nA.

Raw TOF-MEBS data were converted from the time domain to the more familiar energy domain. Simulations of energy domain backscattering spectra and fits to experimental data were performed with *RBSTools*[67] using a variety of thin-films models. Parameters used in the model included film thickness, stoichiometry, and degree of

channeling. When backscattering peaks are separated, stoichiometric ratios may be determined to within a few tenths of a percent; however, overlapping peaks create uncertainty in peak count ratios during deconvolution. Non-uniform compositions also limit the accuracy of stoichiometric ratios.[115] Each layer in the thin film model is assumed to have a constant composition. A composition gradient can be approximated by using a series of separate layers, each with a slightly different composition. Although backscattering analysis provides accurate information concerning the total amount of atoms/cm^2, the accuracy of the concentration profile indicated in a backscattering spectrum is limited by the technique's depth resolution. Instead of an abrupt interface between ZrO_2 and the interfacial layer, the composition of the deposited films is assumed to be graded and is better approximated by a series of layers with slightly different compositions. Although additional layers in the model might improve the overall fit, the reliability of the fit results begins to decline. In this work a single layer is used to represent the interfacial region between the ZrO_2 layer and Si substrate; therefore the interfacial layer only provides the *average* composition in that region. A schematic of the thin film model used in this study is shown if Figure 50.

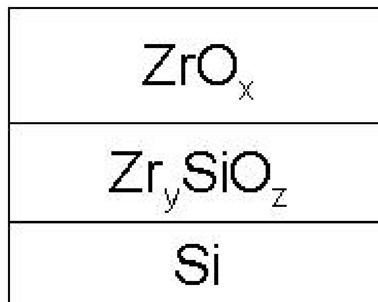

Figure 50. ZrO_2/Zr-silicate/Si thin film model for backscattering spectra simulations.

Results and Discussion

Twelve deposited samples were analyzed with TOF-MEBS and the resulting spectra were simulated with *RBSTools* using the thin film model described in the previous section. Best fits of the simulations to the experimental spectra yielded thickness and stoichiometry values. Densities of 5.7 and 3.5 g/cm^3 were assumed for the ZrO_x and Zr_ySiO_z layers, respectively.

ZrO_2 and Interfacial Layer Composition

Figure 51 shows a TOF-MEBS He^+ backscattering spectrum and simulation of 30 Å of ZrO_2 deposited on H-Si at 350° C. Also shown is the residual χ^2 distribution, in which regions of poor fit are indicated by spikes in the distribution. As a comparison, the backscattering spectrum was simulated using a model with an interfacial layer of SiO_x instead of a Zr-silicate. Figure 51b shows the residual χ^2 distribution when the interfacial layer used in the simulation model is SiO_x instead of a Zr silicate. The best fit to experimental spectrum resulted in overall χ^2 value that was about twice as high as the model with a Zr silicate. The region of poorest fit is the lower energy edge of the Zr signal. This suggests that Zr is in fact present in the interfacial layer of these materials systems.

Inspection of the residual χ^2 distribution in Figure 51a shows that the lower energy edge of the Zr signal still has some degree of misfit with a Zr silicate interfacial layer. The relatively poor fit in this region could be the result of multiple scattering and surface roughness. Multiple scattering causes excessive energy loss due to an increased path length of the analysis ions and, therefore, contributes to the lower-energy region of

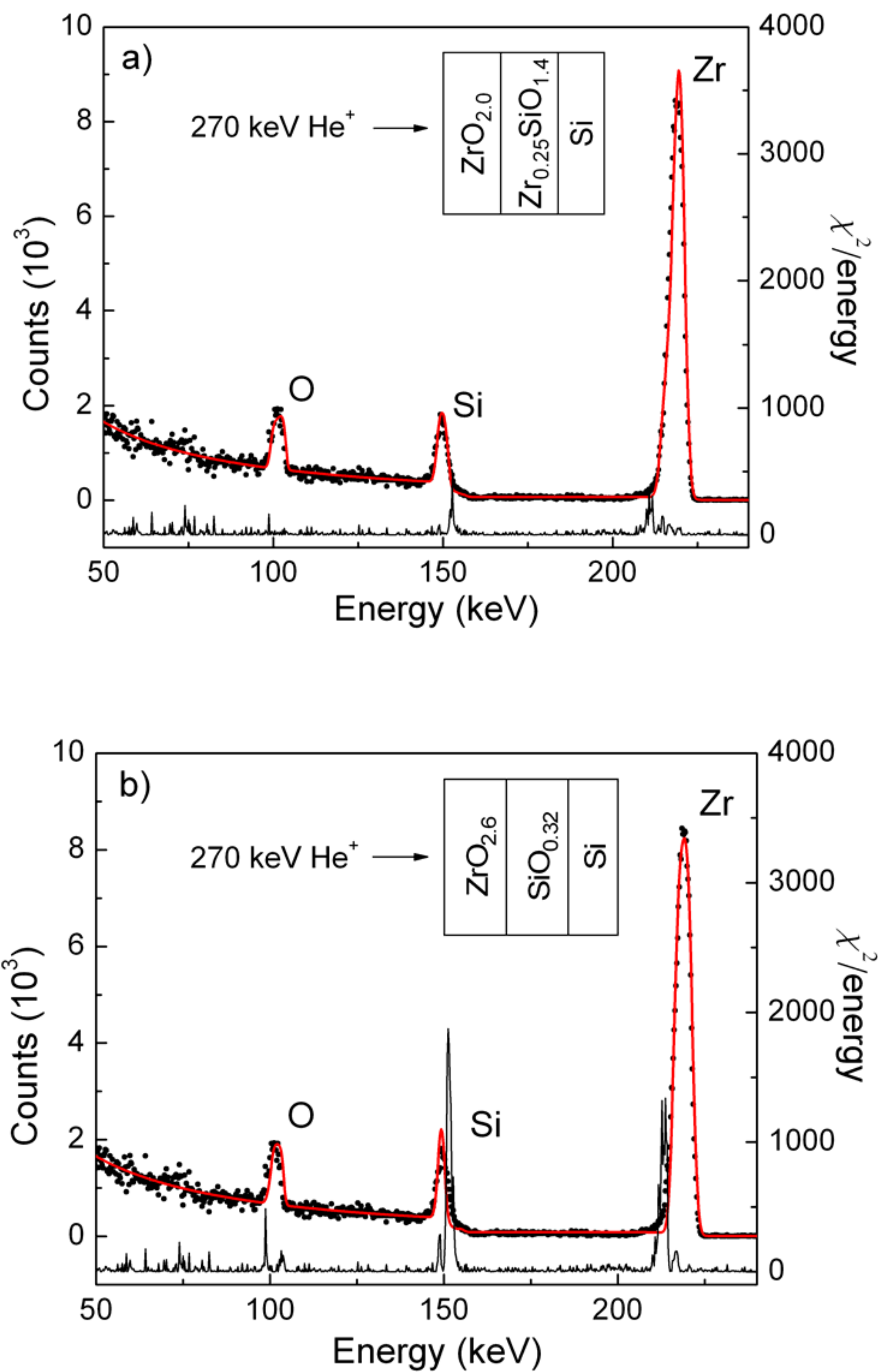

Figure 51. Both figures show the same TOF-MEBS He^+ backscattering spectra (····) of 30 Å ZrO_2 deposited on H-Si at 350° C with best fits from simulations (—) and the residual χ^2 distribution (—) . The thin film model used in a) was $ZrO_x/Zr_ySiO_z/Si$ while the model used in b) had SiO_x as the interfacial layer.

backscattering signals.[101] These contributions are most pronounced for low projectile energies,[100] and high z layers[101]. The relatively high atomic number of Zr might explain why among the regions of poorest fit, the lower energy edge of the Zr signal is the worst.

Surface roughness has a similar effect on backscattering spectra. For films with an RMS roughness (σ) much smaller than the mean film thickness ($\sigma/\underline{d} < 0.1$), only the low energy edge of the film is affected by roughness. When $\sigma/\underline{d}$ is greater than about 0.6, the high energy edge of the signal begins to decrease.[110] AFM analysis of our ZrO_2 films yielded roughness values RMS values of 3 - 7 Å. These roughness values yield a $\sigma/\underline{d}$ value $\geq$ 0.1, which suggests that surface roughness could effect the shape of the backscattering spectra. The broadening in the lower energy edge of the Zr signal that is interpreted as a silicate layer could be exaggerated by the two above mentioned factors. This could lead to an overestimation of the Zr content in the interfacial layer. Thus, the Zr atomic % reported in this paper is an upper estimate. However, because the analysis depths are so small and RMS surface roughness is less than 1 nm in magnitude for all the films analyzed, multiple scattering and roughness effects are considered to have a negligible influence on the shape of the Zr signal's lower energy edge.

Figure 52 shows a TOF-MEBS He^+ backscattering spectrum and simulation of 30 Å of ZrO_2 deposited on native Si oxide (N.O.) surfaces at 350° C. This figure compares spectra simulations with and without a Zr-silicate interfacial layer. The simulation model containing a silicate layer (Figure 52a) resulted in lower residual χ^2 values in the interfacial regions of the spectrum. This is evidence that the native Si oxide layer is reacting to form a Zr-silicate.

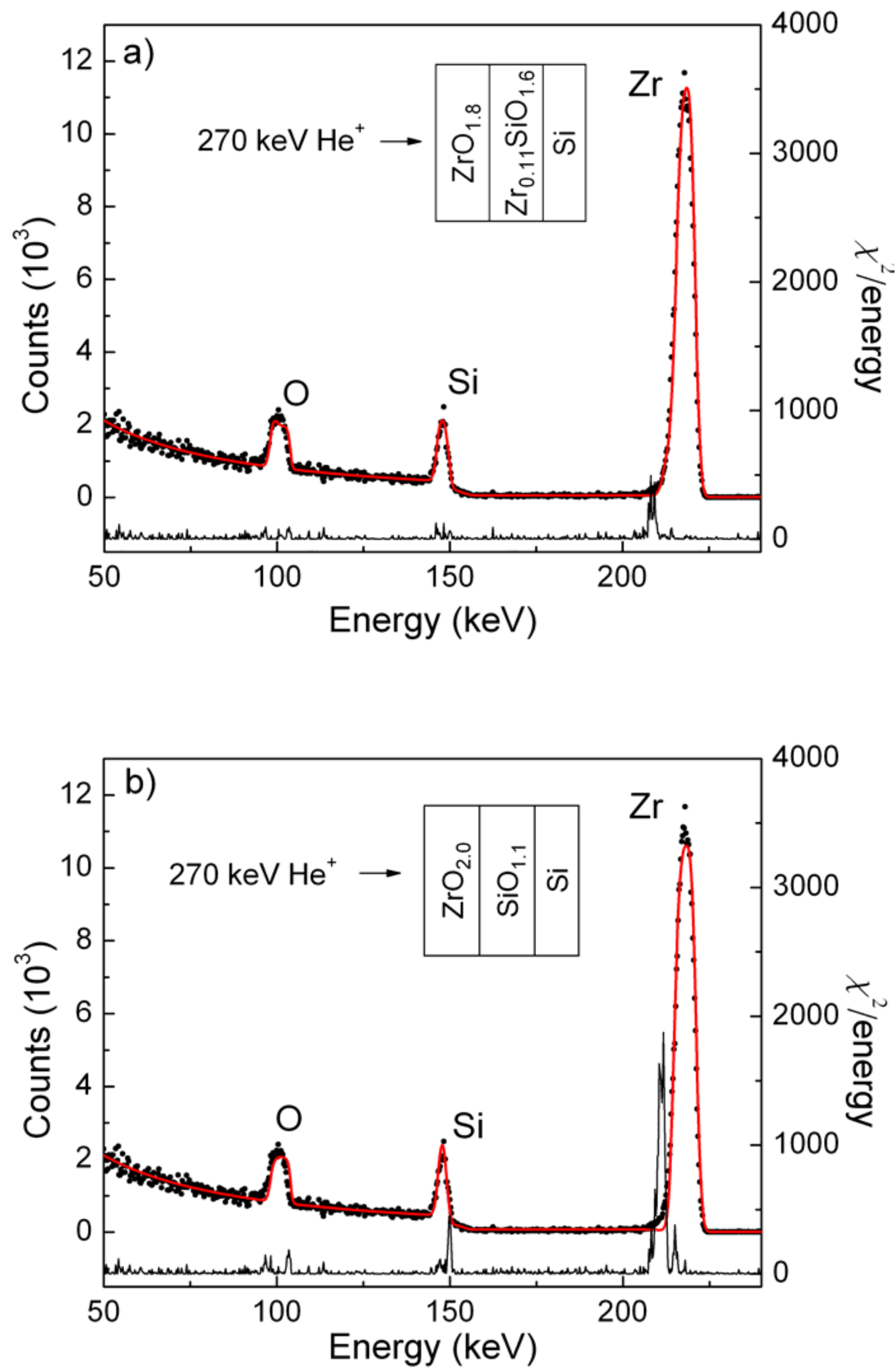

Figure 52. Both figures show the same TOF-MEBS He^+ backscattering spectra (····) of 30 Å ZrO_2 deposited on N.O. at 350° C with best fits from simulations (—) and the residual χ^2 distribution (—) . The thin film model used in a) was $ZrO_x/Zr_ySiO_z/Si$ while the model used in b) had SiO_x as the interfacial layer.

According to TOF-MEBS results, many of the films were found to be slightly oxygen deficient, but all were found to be with in a few atomic percent of the ideal 2:1 O/Zr ratio. Figure 53 shows the atomic % of O in all the ZrO_2 films deposited. An O atomic % of 66.6% corresponds to stoichiometric ZrO_2. Figure 53 does not indicate that the composition of the ZrO_2 layer has a significant dependence on deposition temperature or deposition surface.

The presence of an interfacial silicate is indicated in the backscattering spectra by a slight tail at the lower energy edge of the oxygen and zirconium signals and a broadened silicon signal. The atomic % of Zr in the interfacial region of the deposited films is shown in Figure 54. The average atomic % of Zr in the interfacial layer for the 30 Å films deposited on H-Si was about 7 %, while the corresponding N.O. films had a slightly lower Zr content of 4 %. Similar results were found for the 60 Å set where the interfacial Zr at.% was found to be 6.3% for films deposited on H-Si surfaces compared to 4.4 at.% for N.O. surfaces. The Zr content in the 30 Å films deposited H-Si was found to decrease significantly by about 7 at. % from 350 to 450 °C. However, none of the other sample sets showed such a trend with regard to deposition temperature.

Although thermodynamic calculations suggest that ZrO_2 is stable in direct contact with Si [125], the formation of an interfacial silicate layer in our H-Si films has been observed. The Zr-silicate interfacial layer could be formed by the reaction between ZrO_2 and Si,[124] SiO_2,[14, 18] or SiO_x. [127] In order for the reaction between SiO_2 and ZrO_2 to occur, the initial formation of SiO_2 by the reaction of Si with oxygen is necessary.[18] Although the H-Si substrates used in our experiments were transported to the reactor in

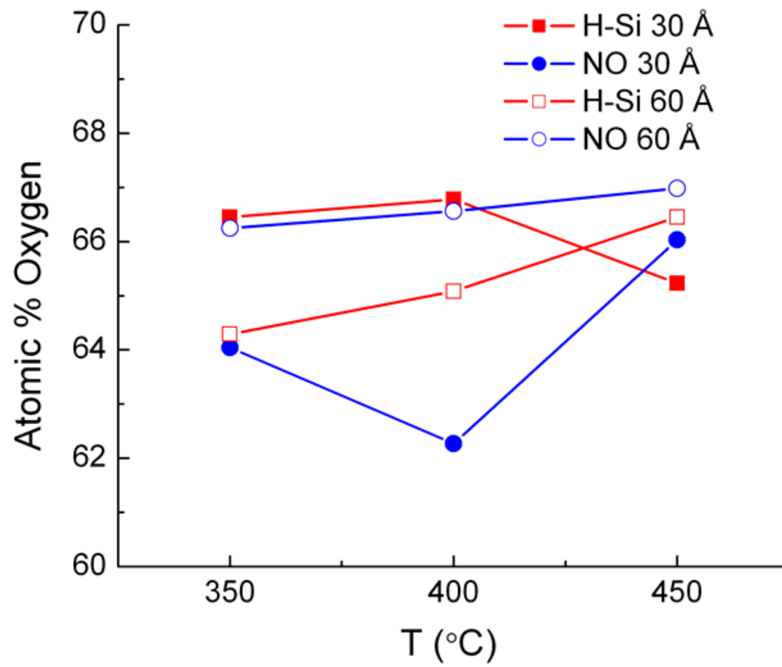

Figure 53. Atomic % of oxygen in 30 and 60 Å ZrO_2 films deposited on H-Si and N.O. at three different temperatures.

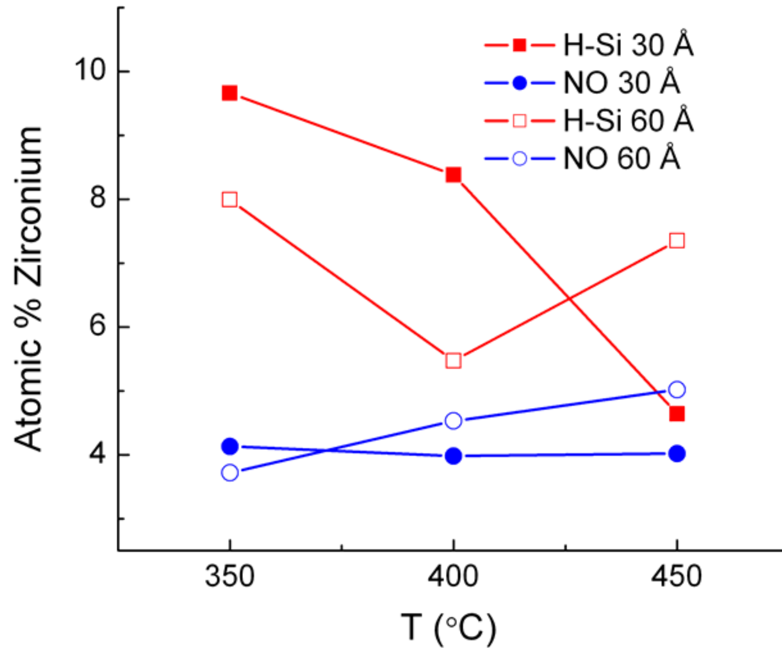

Figure 54. Atomic % of zirconium in interfacial region of 30 and 60 Å ZrO_2 films deposited on H-Si and N.O. at three different temperatures.

air, H-Si surfaces have been shown to be stable in air for at least 1 hr.[94] Additionally, molecular oxygen is never introduced into the reactor during depositions. However, oxygen is present in the precursor and H_2O is a by-product of the reaction of precursor with the deposition surface, which could provide a pathway for the formation of SiO_2. Although interfacial SiO_x has been shown to form during deposition,[14, 123] such a SiO_x layer may have formed after the deposition when the samples were exposed to air when transferring the samples from the deposition system to the TOF-MEBS system.

Studies of the growth of ZrO_2 on thermal SiO_2 surfaces show abrupt interfaces and high thermal stability.[73] However, backscattering spectra from the as-deposited ZrO_2 films on N.O. indicate silicate formation. The reaction of the ZrO_2 layer with the N.O. layer may be due the nature of native silicon oxides. Oxide layers that form on silicon are composed of SiO and SiO_x, but not SiO_2.[128] Thus, the silicate that forms between the ZrO_2 and native oxide layer is most likely due to the reaction between ZrO_2 and sub-silicon oxides. However, a silicate could also form from the reaction between the precursor and silicon oxides. TOF-MEBS analyses confirmed that the native oxide layer is silicon sub-oxide. Analysis of an untreated Si wafer indicates that oxygen and silicon are present on the surface in a 1:1 ratio (Figure 55).

After ZrO_2 deposition, the amount of oxygen in the N.O. layer was found to increase from 50 to around 60 atomic % (Figure 56). The atomic % of oxygen in the interfacial layer that formed between ZrO_2 and H-Si surfaces ranges between about 53 and 63%. For a fully formed silicate ($ZrSiO_4$), the oxygen atomic % is 67.

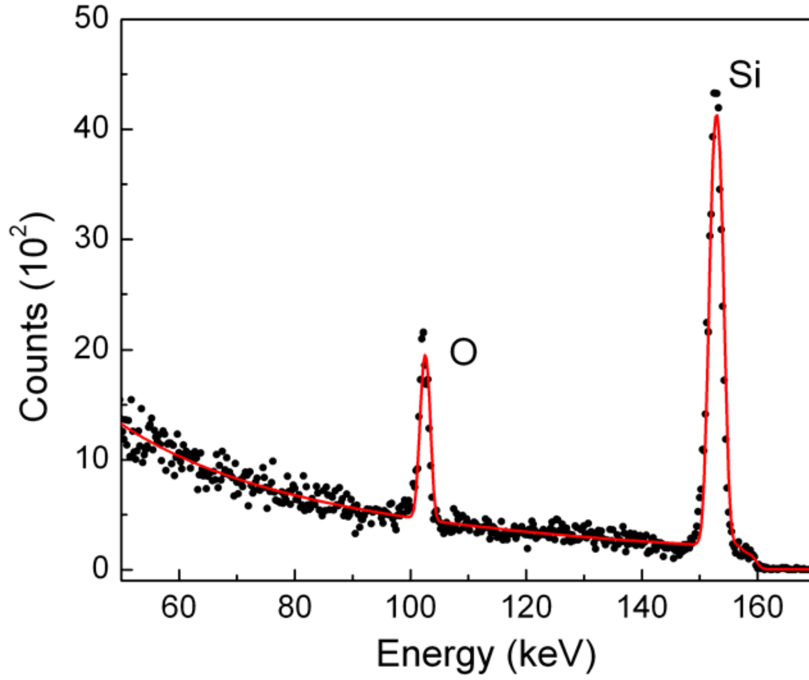

Figure 55. TOF-MEBS He^+ backscattering spectrum (····) and simulation (—) of SiO_x (x ~ 1.0) on Si.

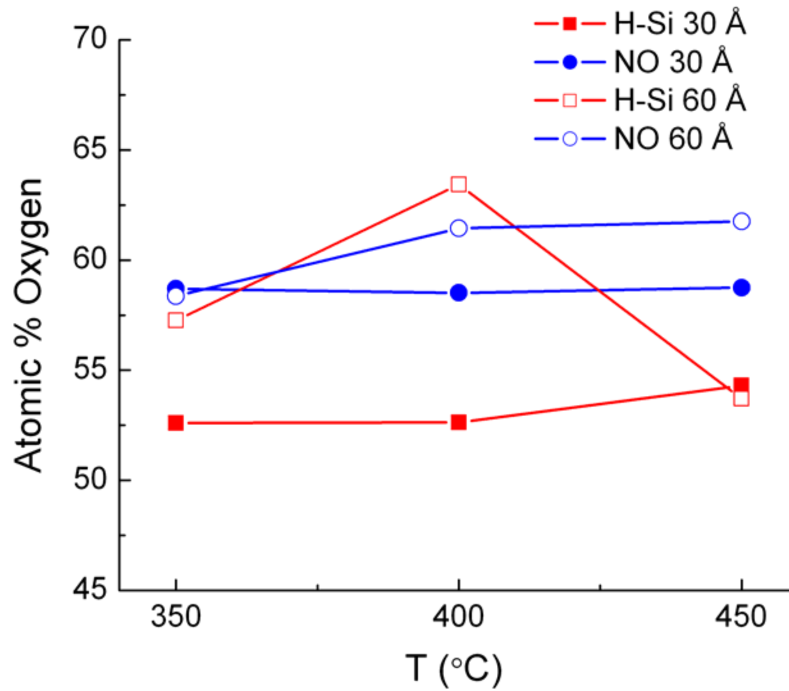

Figure 56. Atomic % of oxygen in interfacial region of 30 and 60 Å ZrO_2 films deposited on H-Si and N.O. at three different temperatures.

Since the total capacitance of a multilayered stack is dominated by the material with the lowest permittivity, it is desirable to minimize the thickness of any low-κ oxide layer between the high-k material and the Si substrate.[77] However, the presence of such a low-κ layer is not completely undesirable. An initially oxidized Si surface provides a high quality interface with high thermal stability and provides a reactive surface to deposit ZrO_2.[73] A smoother interface with Si could also improve carrier mobility in the channel of a MOSFET.[14]

Thin Film Density

Film densities where determined with Equation (VII-1) by assuming that in-situ SE measurements provided true thickness values.

$$\rho_{TOF} t_{TOF} = [atoms/cm^2] = \rho_{REAL} t_{REAL} \qquad \text{(VII-1)}$$

Figure 57 compared densities of the ZrO_2 films deposited on H-Si and N.O. surfaces at three different deposition temperatures. Both the 30 and 60 Å films deposited on N.O. surfaces were denser than those deposited on H-Si surfaces. All density values are lower than the bulk density of ZrO_2, 5.7 g/cm^3. Niinisto and coworkers obtained similar results where film densities were determined using a different analytical technique, x-ray reflectometry. In their study, ZrO_2 layers were deposited on H-Si and N.O. surfaces by atomic layer deposition.[129]

The void fraction of a film is directly related to film density and can be determined by spectroscopic ellipsometry. The void fraction of the samples used in this

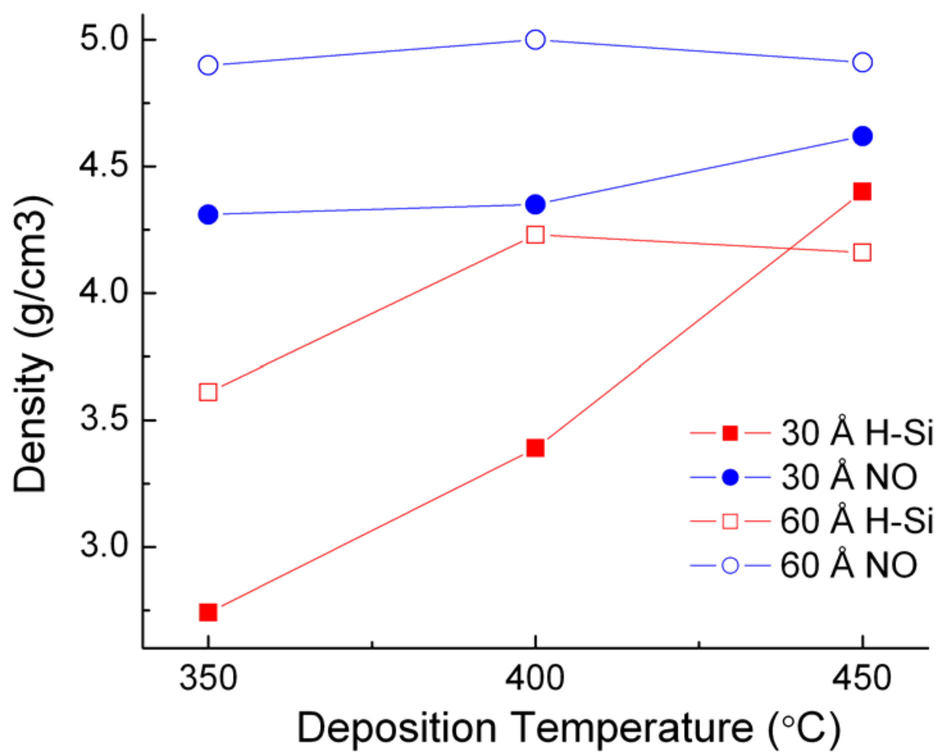

Figure 57. Density of 30 and 60 Å ZrO_2 films deposited on H-Si and N.O. at three different temperatures.

experiment was determined in a study by Song and Rogers.[126] Their results support TOF-MEBS results, which show that ZrO_2 films deposited on N.O. surfaces are denser than those deposited on H-Si surfaces. SE results indicated that the void fraction of films deposited on H-Si is about 10% higher than films deposited on N.O. surfaces for all thicknesses. The differences in film properties of ZrO_2 films deposited on the two surfaces have been explained by the mechanism of the decomposition mechanism of the ZrO_2 precursor, zirconium t-butoxide (ZTB). Unlike H-Si surfaces, native Si oxide surfaces are terminated with reactive hydroxyl groups, which act as reaction centers to initiate ZrO_2 depositions. The high surface density of these reactions sites results in the formation of a uniform low void fraction ZrO_2 layer. The morphology of this layer allows for an even flux of precursor molecules and, therefore, an even deposition of ZrO_2. At the initial stage of deposition on H-Si surfaces, ZrO_2 clusters form around the few available hydroxyl groups and become preferential deposition sites as soon as they are formed. These clusters result in rough film morphology. Therefore, non-uniform flux of precursor molecules occurs and results in the deposition of ZrO_2 in both the lateral and vertical direction. This deposition mechanism results in poor surface coverage and high void fractions.[126]

Song and Rogers[126] also found that the void fraction of H-Si films decreased with deposition temperature and film thickness. At high temperature, more ZrO_2 clusters are formed at the onset of deposition. This limits surface topology development and results in more uniform, low void fraction films. Similar results were obtained with TOF-MEBS. As shown in Figure 57, the density of the 30 Å H-Si films increases with deposition temperature and is comparable to the density of N.O. films for a deposition

temperature of 450° C. The density of the 60 Å H-Si films follow the same trend from 350 to 400 °C, but decreases slightly between 400 and 450 °C.

The presence of pores, associated with low density ZrO_2 films, could be a serious problem with regard to control of the interface. Oxygen is know to have a high diffusivity in ZrO_2.[77] The presence of pores in the film facilitates the diffusion of oxygen to the Si substrate, which can result in SiO_2 growth. Uncontrolled SiO_2 growth at the interface would severely compromise the highest achievable capacitance of the gate stack.

Conclusions

MOCVD ZrO_2 films deposited on hydrogen terminated Si and Si native oxides where analyzed with TOF-MEBS. The nature of the deposition surface was shown to significantly influence the material properties ZrO_2 films and their interface with the deposition surface. TOF-MEBS analysis indicated the presence of a Zr-silicate at the ZrO_2/Si interface for both deposition surfaces and thickness sets. Films deposited on H-Si had a higher Zr content in the interfacial layer than films deposited on a N.O., while those deposited on N.O. were found to have higher densities.

CHAPTER VIII

SUMMARY AND CONCLUSIONS

Time-of-flight medium backscattering (TOF-MEBS) is a powerful analytical technique for characterizing high-κ dielectric thin films and the interface they form with Si. The amount of information that can be obtained from backscattering experiments can be maximized by carefully choosing a detailed thin film model for simulations and by implementing an experimental configuration that optimizes depth resolution. For the analysis of dielectric films a sufficient film model was found to consist of three layers: 1) dielectric material 2) interfacial silicate and 3) substrate. For the analysis of thin films with thicknesses around 50 Å, the depth resolution of the TOF-MEBS system can be improved by operating at a beam energy around 170 keV and by using a glancing tilt angle (~52°). An additional study that would supplement the understanding of depth resolution in the TOF-MEBS system includes measurements as a function of beam energy for tilt angles beyond 45° and measurements at greater analysis depths.

If the target tilt angle in TOF-MEBS experiments is too glancing, multiple scattering and surface roughness can significantly degrade depth resolution and distort the shape of the backscattering spectrum. For the analysis of ZrO_2 films with 270 keV He^+ and a target tilt of 45°, these factors have a negligible influence on the spectrum shape. Additional MC simulations using more glancing angles and rougher surfaces would supplement the results obtained in this work. Surface roughness models used in

the simulations could be obtained from atomic force microscopy (AFM) height data to construct targets with more realistic morphologies.

The physical and chemical properties of MOCVD ZrO_2 films are significantly affected by the deposition surface. ZrO_2 films deposited on H-terminated Si are low in density and susceptible to the formation of an interfacial layer of a silicon oxide or a Zr-silicate. ZrO_2 films deposited on native Si oxide surfaces are dense and less susceptible to interfacial layer formation, although some silicate formation is likely. Compared to H-Si surfaces, deposition on native Si oxide results in higher quality ZrO_2 films; however, thermally grown SiO_2 may offer further improvement. Additional studies should be performed to evaluate differences in the chemical composition and density of MOCVD ZrO_2 films deposited on native Si oxide and thermally grown SiO_2 surfaces.

In Chapter III I showed that the conversion gain and the zero offset of the multichannel analyzer in the TOF-MEBS system changed over time. I recommend a routine check-up every few months to make sure these parameters have not significantly drifted. This check-up can be performed with a standard in which spectral features with known energies can be identified, as was done in this work with a thin film of $HfAl_xO_y$ on Si. Since this calibration is based on the assumption that the beam energy is known, I also recommend a calibration of the beam energy. This could be performed with an alpha-particle energy standard. This standard would allow a proper calibration of the analysis electronics, whereby true energy of the beam could then be obtained by inspecting spectral features of a TOF spectrum in the energy domain.

APPENDIX A

SIMULATING AND FITTING BACKSCATTERING SPECTRA

Backscattering spectra were simulated in this work using the computational tool set *RBSTools*, which is implemented in the platform-independent computational environment *Mathematica*. *RBSTools* set was originally developed for beam energies less than 300 keV, but is suitable for general, classical simulations. The following presents the procedure used in a Mathematica notebook for simulating and fitting backscattering spectra. Only the functions relevant to this work are presented here, but *RBSTools* contains many more functions for performing ion-solid calculations. The functions in *RBSTools* are contained in the files RBSTools.m, IonTools.m, NIonTools.m, and PhysicalChemicalData.m. These packages must be present in the *Applications* directory in the *AddOns* directory containing the *Mathematica* system. *Mathematica* version 3.0 or higher is required. The packages of executable functions are described in more detail by Weller.[67] Spectrum computations and fitting were performed on a PC with a 1.0 GHz processor and 512 MB of memory.

In this appendix, a backscattering spectrum of 270 keV He^+ incident on 50 Å ZrO_2 (density 5.7 g/cm^3)/15 Å SiO_2 (density 2.22 g/cm^3) /Si is simulated and fit to TOF-MEBS data. Actual *Mathematica* commands are shown in **bold** font.

Load all the basic backscattering functions into *Mathematica* by executing the following command:

```
Needs["RBSTools`"]
```

Backscattering spectra are computed using the function **SimulateRBS,** which has as arguments: projectile ion, target definition, incident beam energy, detector position, and target normal position.

A target is defined by its individual layers, with the outermost layer first. Each layer is defined by a three part list: a definition of the element or compound present in the layer, the density of the material, and the thickness of the layer in cm. Data on all elements in the periodic table are included in the package. Each element is identified with its full name and not its abbreviation. The form for a molecule is a list that includes each individual element in the compound and its stoichiometric coefficient.

Define the compounds present in the target:

zro2 = {{Zirconium, 1}, {Oxygen, 2}}

sio2 = {{Silicon, 1}, {Oxygen, 2}}

The density in molecules/cm^3 is computed from the chemical formula and a density in g/cm^3:

ρzro2 = MolecularDensity[zro2, 5.7]

ρsio2 = MolecularDensity[sio2, 2.22]

Atomic density is calculated by:

AtomicDensity[*element_name*]

Define the target:

target = {{zro2, ρzro2, 5.0 nm}, {sio2, ρsio2, 1.5 nm}, {Silicon, AtomicDensity[Silicon], 10^4 nm}}

Thickness is multiplied by the factor **nm** to convert length units from *nm* to *cm*. In order to compute a backscattering spectrum of the target defined above for 270 keV ^{4}He with

the detector at 150° and the target oriented 45° to the beam (75° between target normal and incident beam), execute the following:

s1 = SimulateRBS[Helium[4], target, 270000., {150., 0.}, {135., 180.}]

SimulateRBS returns the number of backscattered particles per unit steradian, per unit energy in eV, per incident ion as a function of energy in eV. In order to get numbers that you would see in a multichannel analyzer, **s1** needs to be multiplied by the number of incident ions, the detector solid angle, the detector efficiency, and the multichannel analyzer width in eV, typically around 10^{14}. This spectrum height adjustment will be referred to as the height scaling factor. The computed spectrum can be plotted as a function of energy:

Plot[10^{14} s1[c], {c, 50000., 240000.}],

which plots backscattering yield as a function of energy (Figure 58):

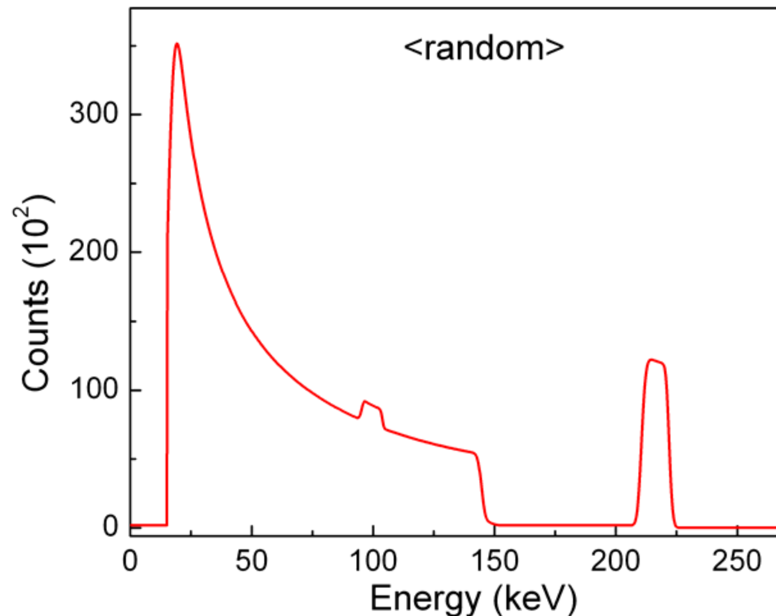

Figure 58. Simulated spectrum for 270 keV ^{4}He on 50 Å ZrO_2/ 15 Å SiO_2/Si.

A channeled spectrum can be computed by using the functional operator **ChannelSubstrate,** which has as arguments a computed spectrum and the channel-to-random ratios. **ChannelSubstrate[s, {chi1, chi2, chi3}]** approximates the effects of channeling by adjusting the height of the substrate signal at three points of the substrate layer: at the highest energy, *chi1*, at the lowest energy, *chi3* (usually the cutoff energy), and at the arithmetic average of these two, *chi2*. A spectrum with a channeled substrate is calculated by the following:

s2 = ChannelSpectrum[SimulateRBS[Helium[4], target, 270000., {150., 0.}, {135., 180.}], {0.05, 0.05, 0.05}]

The substrate yield has been reduced by 95%. Evaluating **s2** as a function of energy yields the following channeled spectrum (Figure 59):

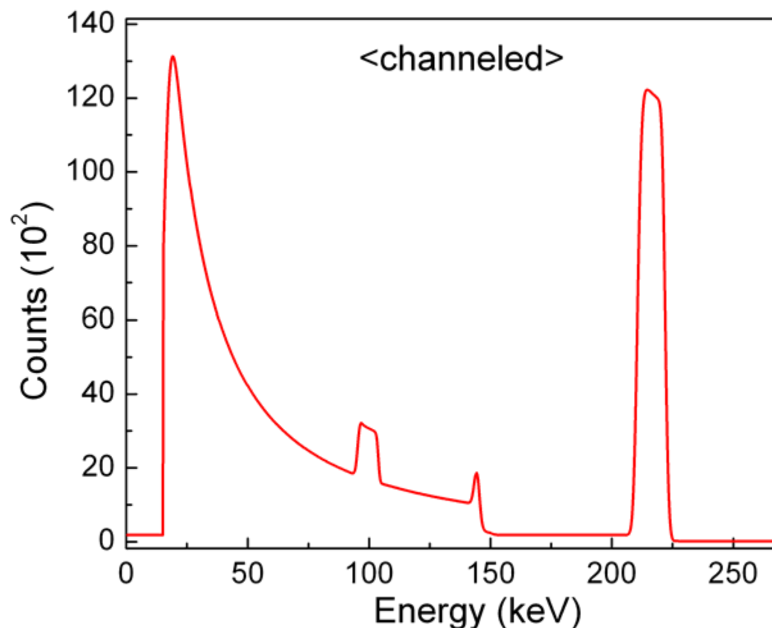

Figure 59. Simulated backscattering spectrum with a channeled substrate.

In a channeled spectrum there are some contributions from the first few monolayers of the crystalline substrate, which results in a peak at the front edge of the Si signal. This

feature is obtained in a simulated spectrum by including in the target definition a thin layer (~ 2 Å) with the same composition as the substrate.

Fits to backscattering spectra are performed with the function **SpectrumFit**. **SpectrumFit** performs a non-linear least squares fit to experimental spectra using Marquardt's method.[129] Best fit values can be determined for film thickness, composition, background, or for any other parameter that is adjustable in the simulation or evaluation of a spectrum. **SpectrumFit** has as arguments: {data, model, parameters}. The third argument is a list of initial guesses at the best fit parameters. In this example, a simulated spectrum similar to the one simulated above will be fit to an experimental TOF-MEBS spectrum using 11 fit parameters. The model that will be used in the fit is:

```
model1[a_Real, bkg_Real, chan0_Real, dzro_Real, dsio2_Real,
  nZr_Real, chi1_Real, chi2_Real, chi3_Real, KScale_Real, H_Real] :=
 Module[{target, s}, zro = {{Zirconium, nZr}, {Oxygen, 2}};
       target = {{zro, ρzro1, dzro*nm}, {sio2, ρsio2, dsio2*nm},
    {Silicon, AtomicDensity[Silicon], .2 nm},
    {Silicon, AtomicDensity[Silicon], 10^4 nm}};
       s =
   a*10^14*ChannelSubstrate[SimulateRBS[Helium[4], target,
     270*10^3, {150., 0.}, {135., 180.}], {chi1, chi2, chi3}];
    Function[Evaluate[bkg - H (Erf[(# - E2*10^3)/Sqrt[2 σ2*10^5]]) + s[(#*KScale + chan0)]]]]
```

Model parameters are followed by **_Real** to cast them as real numbers. The model parameters are as follows:

a: height scaling factor;

bkg: linear background;

chan0: energy equivalent zero-time channel;

dZrO2, **dSiO2**: thickness of ZrO_2 and SiO_2 layers, respectively;

nZr: stoichiometric coefficient for adjusting composition of ZrO_2 layer;

chi1, **chi2**, **chi3**: channeled-to-random ratio;

KScale: adjusts energy channel width. This parameter is equal to 1.0 if the parameters used in the conversion of spectra from the time to energy are correct;

H: height of the error function used for adjusting background near the Zr signal, as described in Chapter IV.

The user must define the experimental data to which the simulation will be fit:

Set directory of data file: **SetDirectory["*filepath*"]**

Import the desired file: **soraw = Import["S12_18_3.txt", "Table"];**

View the selected data by executing the following:

lp1 = ListPlot[soraw,PlotRange→All] (Figure 60)

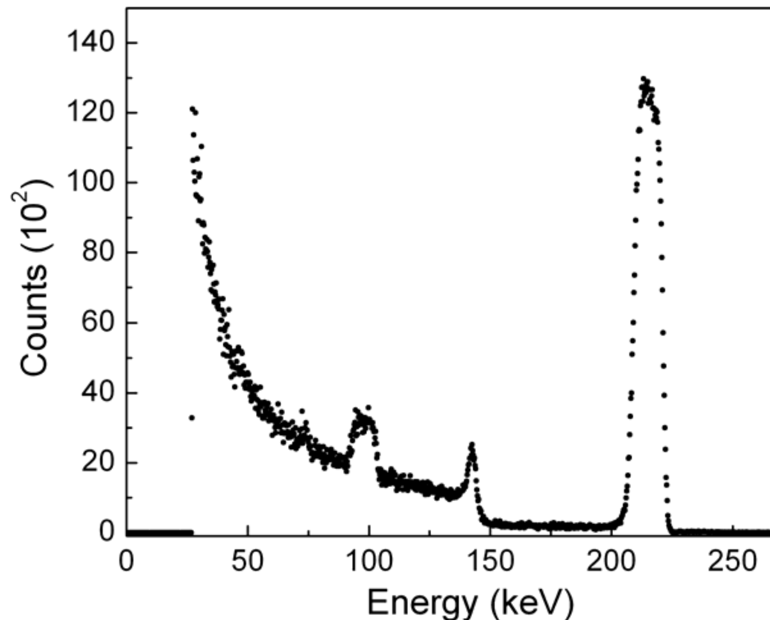

Figure 60. Experimental TOF-MEBS spectra for 270 keV He^+ on ZrO_2/Si.

The low energy region of the spectrum does not contain features of interest, so a range of points are selected: **so = Take[soraw,{180, 970}]** (Figure 61)

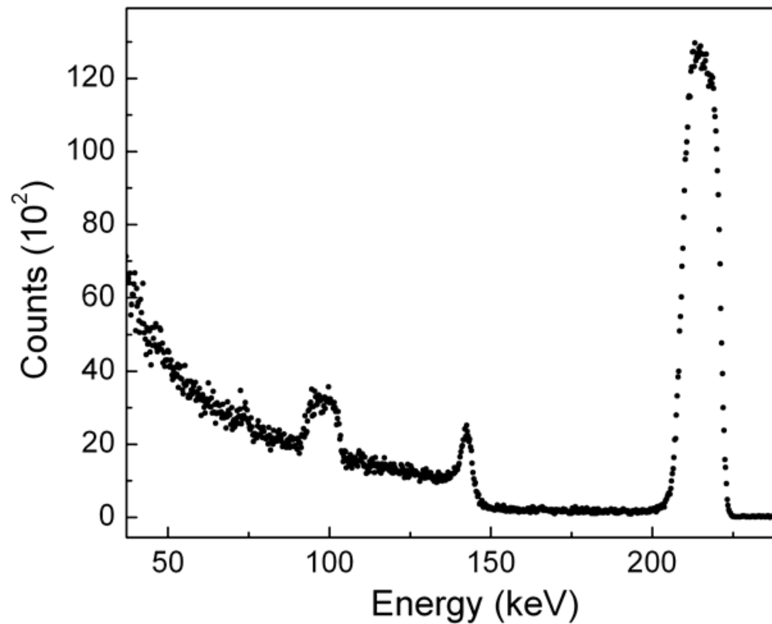

Figure 61. Selected region of experimental TOF-MEBS spectrum for 270 keV He^+ on ZrO_2/Si.

The data has been selected, and the model has been defined. Now perform the fit with an initial guess at the best-fit parameters:

> **fit1 = SpectrumFit[so, model1, {0.594, 103.3, -5900., 5., 1.0, 1.0, 0.16, 0.23, 0.37, 1.06, 85.0}]**

SpectrumFit returns a three member list: a list of the best-fit parameters, a list with the corresponding standard deviations, and a list with χ^2, the number of degrees of freedom, and the χ^2 cumulative probability. Simulate the backscattering spectrum with the best fit parameters and superimpose the spectrum on the experimental data: **Show[so, lp1]** (Figure 62)

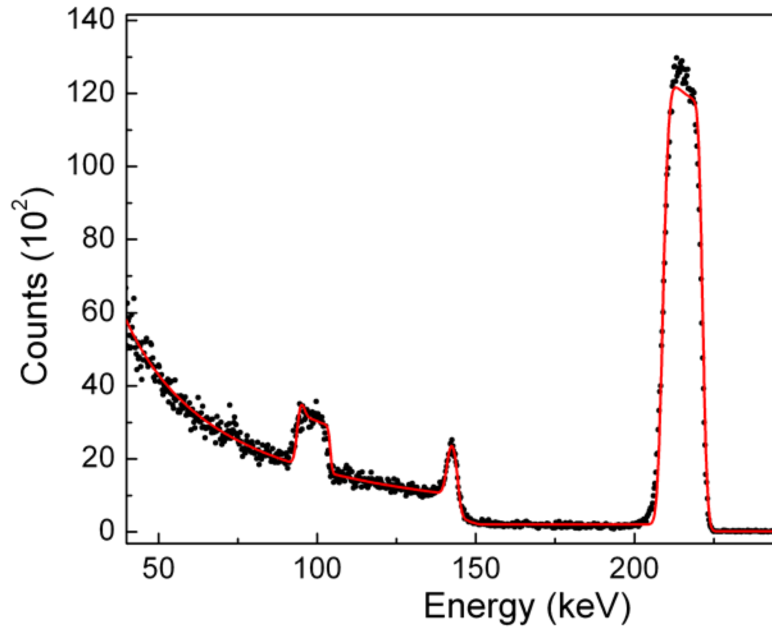

Figure 62. Backscattering spectrum and best fit simulation of 270 keV He^+ on 55 Å $Zr_{1.02}O_2$/ 26 Å SiO_2/Si.

The overall χ^2 of the best fit simulation is 18,660 for 780 degrees of freedom. The residual χ^2 distribution is calculated by:

```
χsquarelist = Function[{First[#], (s1[First[#]] - Last[#])^2 / s1[First[#]]}] /@ so
```

A plot of the residual χ^2 distribution is shown in Figure 63.

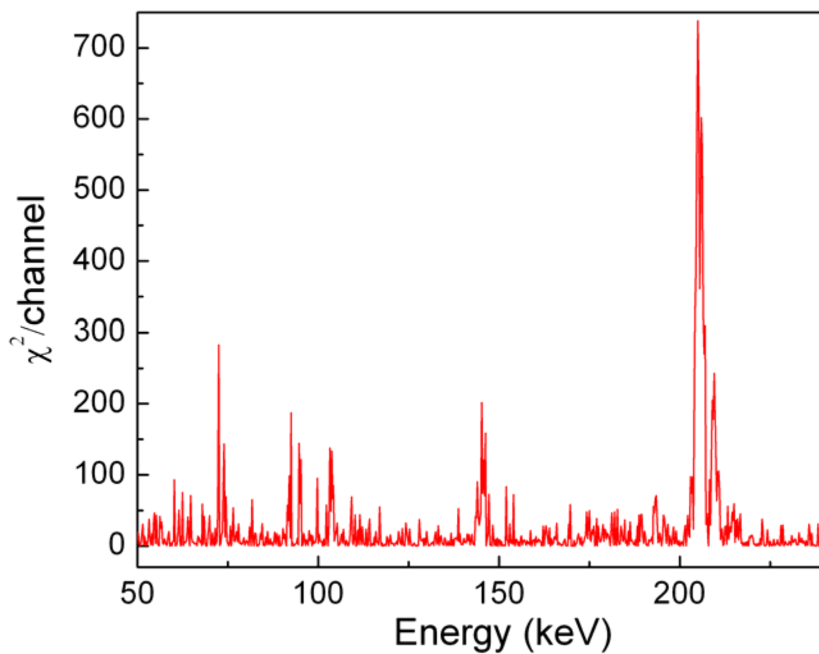

Figure 63. Residual χ^2 distribution.

REFERENCES

1. Moore, G.E., Proceedings of the IEEE **86** (1998) 82-85.

2. Wilk, G.D., Wallace, R.M., and Anthony, J.M., Appl. Phys. Rev. **89** (2001) 5243-5275.

3. Green, M.L., Sorsch, T.W., Timp, G.L., Muller, D.A., Weir, B.E., Silverman, P.J., Moccio, S.V., and Kim, Y.O., Microelectronic Engineering **48** (1999) 25-30.

4. Zant, P.V., *Microship Fabrication: A Practical Guide to Semiconductor Processing*. 4th ed. ed. 200, New York: McGraw-Hill.

5. Weldon, M.K., Queeny, J.E., Raghavachari, K., and Chabal, Y.J., Surf. Sci. **500** (2002) 859-878.

6. *The National Technology Roadmap for Semiconductors*. 2002, Semiconductor Industry Association.

7. Buchanan, D.A., IBM J. Res. and Dev. **43** (1999) 245-264.

8. Battiston, G.A., Carta, G., Cavinato, G., Gerbasi, R., Porchia, M., and Rossetto, G., Chem. Vap. Deposition **7** (2001) 69-74.

9. Chin, A., Liao, C.C., Lu, C.H., Chen, W.J., and Tsai, C., Digest of Technical Papers - Symposium on VLSI Technology (1999) 135-136.

10. George, S.M., Ott, A.W., Klaus, J.W., McCarley, K.C., and Way, J.D., Appl. Surf. Sci. **107** (1996) 128-136.

11. Groner, M.D., Elam, J.W., Fabreguette, F.H., and George, S.M., Thin Solid Films **413** (2002) 186-197.

12. Hubbard, K.J. and Schlom, D.G., J. Mater. Res. **11** (1996) 2757-2776.

13. Koh, W., Ku, S.-J., and Kim, Y., Thin Solid Films **304** (1997) 222-224.

14. Chen, H.-W., Huang, T.-Y., Landheer, D., Wu, X., Moisa, S., Sproule, G.I., and Chao, T.-S., J. Electrochem. Soc. **149** (2002) F49-F55.

15. Ferrari, S., Dekadjevi, D.T., Spiga, S., Tallarida, G., Wiemer, C., and Fanciulli, M., Journal of Non-Crystalline Solids **303** (2002) 29-34.

16. Kukli, K., Forsgren, K., Aarik, J., Uustare, T., Aidla, A., Niskanen, A., Ritala, M., Leskela, M., and Harsta, A., J. Crystal Growth **231** (2001) 262-272.

17. Lin, Y.S., Puthenkovilakam, R., Chang, J.P., Bouldin, C., Levin, I., Hguyen, N.V., Ehrstein, J., Sun, Y., Pianetta, P., Conard, T., and Vandervorst, W., J. Appl. Phys. **93** (2003) 5945-5952.

18. Wu, X., Landheer, D., Graham, M.J., Chen, H.W., Huang, T.Y., and Chao, T.S., J. Crystal Growth **250** (2003) 479-485.

19. Gusev, E.P., Cabral, J., C., Copel, M., D'Emic, C., and Gribelyuk, M., Microelectronic Engineering **69** (2003) 145-151.

20. Han, D., Kang, J., Lin, C., and Han, R., Microelectronic Engineering **66** (2003) 643-647.

21. Lee, P.F., Dai, J.Y., Chan, H.L.W., and Choy, C.L., Ceramics International **30** (2004) 1267-1270.

22. Nieveen, W., Schueler, B.W., Goodman, G., Schnabel, P., Moskito, J., Mowat, I., and Chao, G., Appl. Surf. Sci. **231-232** (2004) 556-560.

23. Renault, O., Samour, D., Rouchon, D., Holliger, P., Papon, A.-M., Blin, D., and Marthon, S., Thin Solid Films **428** (2003) 190-194.

24. Boughaba, S., Islam, M., McCaffrey, J.P., Sproule, G.I., and Graham, M.J., Thin Solid Films **371** (2000) 119-125.

25. Boughaba, S., Sproule, G.I., McCaffrey, J.P., Islam, M., and Graham, M.J., Thin Solid Films **358** (2000) 104-113.

26. Mao, A.Y., Son, K.A., Hess, D.A., Brown, L.A., White, J.M., Kwong, D.L., Roberts, D.A., and Vrtis, R.N., Thin Solid Films **349** (1999) 230-237.

27. van Dover, R.B., Lang, D.V., Green, M.L., and Manchanda, L., J. Vac. Sci. Technol. A **19** (2001) 2779-2784.

28. Zhao, C., Richard, O., Young, E., Bender, H., Roebben, G., Haukka, S., De Gendt, S., Houssa, M., Carter, R., and Tsai, W., J. Non-Cryst. Solids **303** (2002) 144-149.

29. Qi, W.J., Nieh, R., Lee, B.H., Kang, L.G., Jeon, Y., and Lee, J.C., Appl. Phys. Lett. **77** (2000) 3269-3271.

30. Wilk, G.D. and Wallace, R.M., Appl. Phys. Lett. **76** (2000) 112-114.

31. Wilk, G.D., Wallace, R.M., and Anthony, J.M., J. Appl. Phys. **87** (2000) 484-492.

32. Yamada-Takamura, Y., Koch, F., Maier, H., and Bolt, H., Surface and Coatings Technology **142-144** (2001) 260-264.

33. Sun, Y.-M., Lozano, J., Ho, H., Park, H.J., Veldman, S., and White, J.M., Appl. Surf. Sci. **161** (2000) 115-122.

34. Hu, Y.-Z. and Tay, S.-P., J. Vac. Sci. Technol. B **19** (2001) 1706-1714.

35. Dey, S.K., Wang, C.G., Tang, D., Kim, M.J., Carpenter, R.W., Werkhoven, C., and Shero, E., J. Appl. Phys. **93** (2003) 4154-4157.

36. Chang, J.P., Lin, Y.S., and Chu, K., J. Vac. Sci. Technol. B **19** (2001) 1782-1787.

37. Klein, T.M., Niu, D., Epling, W.S., Li, W., Maher, D.M., Hobbs, C.C., Hegde, R.I., Baumvol, I.J.R., and Parsons, G.N., Appl. Phys. Lett. **75** (1999) 4001-4003.

38. Haanappel, V.A.C., v.d. Vendel, D., van Corbach, H.D., Fransen, T., and Gellings, P.J., Thin Solid Films **256** (1995) 8-12.

39. Kuo, D.-H., Cheung, B.-Y., and Wu, R.-J., Thin Solid Films **398-399** (2001) 35-40.

40. Maruyama, T. and Arai, S., Appl. Phys. Lett. **60** (1992) 322-323.

41. Busch, B.W., Pluchery, O., Yves, J.C., Mueller, D.A., Opila, R.L., Kwo, J.R., and Garfunkel, E., MRS Bulliten (2002) 206-211.

42. Misra, V., Lucovsky, G., and Parsons, G.N., MRS Bulliten (2002) 212-216.

43. Jach, T. and Landree, E., National Institute of Standards and Technology (2000)

44. Feldman, L.C. and Mayer, J.W., *Ch. 4*, in *Fundamentals of surface and thin film analysis*. 1986, Elsevier Science Publishing Co., Inc: New York. p. 352.

45. Besling, W.F.A., Young, E., Conard, T., Zhao, C., Carter, R., Vandervorst, W., Caymax, M., De Gendt, S., Heyns, M., and Maes, J., J. Non-Cryst. Solids **303** (2002) 123-133.

46. Feldman, L.C. and Mayer, J.W., *Ch. 2*, in *Fundamentals of surface and thin film analysis*. 1986, Elsevier Science Publishing Co., Inc: New York. p. 352.

47. Weller, R.A., *Ch. 12*, in *Methods in Materials Research*. 2000, Wiley: New York. p. 12b.1-15.

48. Mendenhall, M.H. and Weller, R.A., Nucl. Instr. and Meth. B **58** (1991) 11-17.

49. Mendenhall, M.H. and Weller, R.A., Nucl. Instr. and Meth. B **227** (2005) 420-430.

50. Leavitt, J.A., McIntyre, L.C., and Weller, M.R., *Ch. 4*, in *Handbook of modern ion beam materials analysis*, J.R. Tesmer and M.A. Nastasi, Editors. 1995, Mater. Res. Soc.: Pittsburg. p. 5-19.

51. Chu, W.K., Mayer, J.M., and Nicolet, M.A., *Backscattering Spectrometry*. 1978, New York: Academic Press.

52. Ziegler, J.F., J. Appl. Phys. **85** (1999) 1249-1272.

53. Feldman, L.C. and Mayer, J.W., *Ch. 3*, in *Fundamentals of surface and thin film analysis*. 1986, Elsevier Science Publishing Co., Inc: New York. p. 352.

54. Rauhala, E., *Ch. 2*, in *Handbook of modern ion beam materials analysis*, J.R. Tesmer and M.A. Nastasi, Editors. 1995, Mater. Res. Soc.: Pittsburg. p. 5-19.

55. Chan, E.K.L., Powers, D., Lodhi, A.S., and Brown, R.B., Appl. Phys. **49** (1978) 2346.

56. Kreutz, R., Neuwirth, W., and Pietsch, W., Physics Review **A22** (1988) 2598.

57. Ziegler, J.F. and Manoyan, J.M., Nucl. Instr. and Meth. B **35** (1988) 215-228.

58. Lennard, W.N., Xia, H., and Kim, J.K., Nucl. Instr. and Meth. B **215** (2004) 297-307.

59. Pascual-Izarra, C., Bianconi, M., Lulli, G., and Summonte, C., Nucl. Instr. and Meth. B **196** (2002) 209-214.

60. Yang, Q., O'Connor, D.J., and Wang, Z., Nucl. Instr. and Meth. B **61** (1991) 149-155.

61. Feldman, L.C. and Mayer, J.W., *Ch. 5*, in *Fundamentals of surface and thin film analysis*. 1986, Elsevier Science Publishing Co., Inc: New York. p. 352.

62. Mendenhall, M.H. and Weller, A.R., Nucl. Instr. and Meth. B **40/41** (1989) 1239-1243.

63. Weller, R.A., *Ch. 11*, in *Handbook of modern ion beam materials analysis*, J.R. Tesmer and M.A. Nastasi, Editors. 1995, Mater. Res. Soc.: Pittsburg. p. 5-19.

64. Weller, R.A., *Time-of-flight medium energy spectrometer*, Vanderbilt University: Nashville.

65. Weller, R.A., Arps, J.H., Pedersen, D., and Mendenhall, M.H., Nucl. Instr. and Meth. A **353** (1994) 579-582.

66. Arps, J.H. and Weller, R.A., Nucl. Instr. and Meth. B **90** (1994) 547-551.

67. Weller, A.R., *General purpose computational tools for simulation and analysis of medium-energy backscattering analysis*, in *Applications of Accelerators in Research and Industry*, J.L. Duggan and I.L. Morgan, Editors. 1999, The American Institute of Physics: New York. p. 596.

68. Barradas, N.P. and Jeynes, C., Appl. Phys. Lett. **71** (1997) 171-175.

69. Doolittle, L.R., Nucl. Instr. and Meth. B **9** (1985) 344-351.

70. Kotai, E., Nucl. Instr. and Meth. B **85** (1994) 588-596.

71. Battistig, G., Amsel, G., d'Artemare, E., and L'Hoir, A., Nucl. Instr. and Meth. B **85** (1994) 572-578.

72. Mayer, M., *SIMNRA user's guide*. 1997, Tech. Rep. IPP 9/113: Max-Plank-Institut fur Plasmaphysik, Garching.

73. Copel, M., Gribelyuk, M., and Gusev, E., **76** (2000) 436-438.

74. Gustafsson, T., Lu, H.C., Busch, B.W., Schulte, W.H., and Garfunkel, E., Nucl. Instr. and Meth. B **183** (2001) 146-153.

75. Copel, M., IBM J. Res. and Dev. **44** (2000) 571-582.

76. Copel, M., Cartier, E., Gusev, E.P., Guha, S., Bojarczuk, N., and Poppeller, M., Appl. Phys. Lett. **78** (2001) 2670-2672.

77. Busch, B.W., Schulte, W.H., Garfunkel, E., and Gustafsson, T., Phys. Rev. B **62** (2000) 290-293.

78. Mendenhall, M.H. and Weller, A.R., Nucl. Instr. and Meth. B **47** (1990) 193-201.

79. Woollam, J.A., Johs, B., Herzinger, C.M., Hilfiker, J., Synowicki, R., and Bungay, C.L., Critical Reviews of Optical Science and Technology **CR72** (1999) 3-28.

80. Tonova, D., Depas, M., and Vanhellemont, J., Thin Solid Films **288** (1996) 64-68.

81. Williams, D.B. and Carter, C.B., *Transmission Electron Microscopy: Basics*. Vol. I. 1996, New York: Plenum Press.

82. Bonnell, D.A., *Scanning Probe Microscopy and Spectroscopy: Theory, Techniques, and Applications*. 2 ed. 2001, New York: Wiley. 493.

83. McDonald, K., Weller, R.A., and Liechtenstein, V.K., Nucl. Instr. and Meth. B **152** (1999) 171-181.

84. Weller, R.A., *private communication*. Vanderbilt University, Nashville, TN (2005).

85. Kimura, K. and Nakajima, K., Appl. Surf. Sci. **216** (2003) 283-286.

86. Williams, J.S., Nucl. Instr. and Meth. **126** (1975) 205-215.

87. Williams, J.S. and Moller, W., Nucl. Instr. and Meth. **157** (1978) 213-221.

88. Mendenhall, M.H. and Weller, A.R., Nucl. Instr. and Meth. B **59/60** (1991) 120-123.

89. Weller, R.A., McDonald, K., Pedersen, D., and Keenan, J.A., Nucl. Instr. and Meth. B **118** (1996) 556-559.

90. Arps, J.H., Weller, R.A., Tung, Y.S., and Henderson, D.O., Nucl. Instr. and Meth. B **99** (1995) 623-626.

91. Huang, M.B., McDonald, K., Keay, J.C., Wang, Y.Q., Rosenthal, S.J., Weller, R.A., and Feldman, L.C., Appl. Phys. Lett. **73** (1998) 2914-2916.

92. Rauhala, E., *Handbook of modern ion beam materials analysis*, ed. J.R. Tesmer and M.A. Nastasi. 1995, Pittsburg: Mater. Res. Soc. 385-410.

93. Press, W.H., Teukolsky, S.A., Vetterling, W.T., and Flannery, B.P., *Ch. 15*, in *Numerical Recipes in C*. 1992, Cambridge University Press: Cambridge. p. 681-688.

94. Tsai, W., Carter, R.J., Nohira, H., Caymax, M., Conard, T., Cosnier, V., DeGendt, S., Heyns, M., Petry, J., and Richard, O., Microelectron. Eng. **65** (2003) 259-272.

95. Gutierrez, G. and Johansson, B., Phys. Rev. B **65** (2002) 104202.

96. Chang, J.P. and Lin, Y.-S., J. Vac. Sci. Technol. B **19** (2001) 2137-2142.

97. Kukli, K., Ritala, M., Uustare, T., Aarik, J., Forsgren, K., Sajavaara, T., Leskela, M., and Harsta, A., Thin Solid Films **410** (2002) 53-60.

98. Eckstein, W. and Mayer, M., Nucl. Instr. and Meth. B **153** (1999) 337-344.

99. Bauer, P., Steinbauer, E., and Biersack, J.P., Nucl. Instr. and Meth. B **79** (1993) 443-445.

100. Weber, A., Mommsen, H., Sarter, W., and Weller, A., Nucl. Instr. and Meth. **198** (1982) 527-533.

101. Steinbauer, E., Bauer, P., and Biersack, J.P., Nucl. Instr. and Meth. B **45** (1990) 171-175.

102. Bauer, P., Steinbauer, E., and Biersack, J.P., Nucl. Instr. and Meth. B **64** (1992) 711-715.

103. Edge, R.D. and Bill, U., Nucl. Instr. and Meth. **168** (1980) 157-162.

104. Knudson, A.R., Nucl. Instr. and Meth. **168** (1980) 163-167.

105. Hobbs, C.P., McMillan, J.W., and Palmer, D.W., Nucl. Instr. and Meth. **30** (1988) 342-348.

106. Metzner, H., Hahn, T., Gossla, M., Conrad, J., and Bremer, J.H., Nucl. Instr. and Meth. B **134** (1998) 249-261.

107. Shorin, V.S. and Sosnin, A.N., Nucl. Instr. and Meth. B **72** (1992) 452-456.

108. Wuest, M. and Bochsler, P., Nucl. Instr. and Meth. B **71** (1992) 314-323.

109. Yesil, I.M., Assmann, W., Huber, H., and Lobner, K.E.G., Nucl. Instr. and Meth. B **136-138** (1998) 623-627.

110. Mayer, M., Nucl. Instr. and Meth. B **194** (2002) 177-186.

111. Agostinelli, S., Allison, J., Amako, K., Apostolakis, J., Araujo, H., Arce, P., Asai, M., Axen, D., Banerjee, S., and Barrand, G., Nucl. Instr. and Meth. A **506** (2003) 250-303.

112. Mendenhall, M.H., *private communication*. Vanderbilt University, TN (2005).

113. Ziegler, J.F., Biersack, J.P., and Littmark, U., *The Stopping and Range of Ions in Solids*. 1985, New York: Pergamon Press. 321.

114. Geil, R.D., Rogers, B.R., Weller, R.A., and Song, Z., J. Vac. Sci. Technol. A **22** (2004) 1129-1133.

115. Tesmer, J.R. and Nastasi, M.A., *Ch. 2*, in *Handbook of modern ion beam materials analysis*, J.R. Tesmer, Editor. 1995, Mater. Res. Soc.: Pittsburg. p. 385-410.

116. Kim, M.S., Bue, Y.D., and Bak, H.I., Nucl. Instr. and Meth. B **108** (1996) 139-146.

117. O'Connor, D.J. and Chunyu, T., Nucl. Instr. and Meth. B **36** (1989) 178-188.

118. Szilagyi, E. and Paszti, F., Nucl. Instr. and Meth. B **85** (1994) 616-620.

119. Cox, R.P., Leavitt, J.A., and McIntyre, L.C., *Appendix 7*, in *Handbook of modern ion beam materials analysis*, J.R. Tesmer and M.A. Nastasi, Editors. 1995, Mater. Res. Soc.: Pittsburg. p. 481-508.

120. Harris, J.M., Chu, W.K., and Nicolet, M.A., Thin Solid Films **19** (1973) 259-265.

121. Szilagyi, E., Nucl. Instr. and Meth. B **161-163** (2000) 37-47.

122. Szilagyi, E., *DEPTH*. 2004, http://www.kfki.hu/%7Eionhp/doc/prog/mdepth.htm.

123. Jeon, T.S., White, J.M., and Kwong, D.L., Appl. Phys. Lett. **78** (2001) 368-370.

124. Yamaguchi, T., Satake, H., Fukushima, N., and Toriumi, A., **80** (2002) 1987-1989.

125. Caballero, A.C., Fernandez, J.F., Moure, C., Duran, P., and Chiang, Y.M., Journal of the American Ceramic Society **81** (1998) 939-944.

126. Song, Z., Sullivan, L.M., and Rogers, B., J. Vac. Sci. Technol. A **23** (2005) 165-176.

127. Blumenthal, W.B., *The Chemical Behavior of Zirconium*. 1958, Princeton: Van Nostrand.

128. Philipp, H.R. and Taft, E.A., **53** (1982) 5224-5229.

129. Niinisto, J., Putkonen, M., Niinisto, L., Kukli, K., Ritala, M., and Leskela, M., J. Appl. Phys. **95** (2004) 84-91.